ISTANBUL TECHNICAL UNIVERSITY ★ GRADUATE SCHOOL

INVESTIGATION OF THERMAL CONDUCTION IN MICROCONTACTS CREATED BY INDENTATION

M.Sc. THESIS

Ahmed ULUCA

Department of Physics Engineering

Physics Engineering Programme

APRIL 2022

ISTANBUL TECHNICAL UNIVERSITY ★ GRADUATE SCHOOL

INVESTIGATION OF THERMAL CONDUCTION IN MICROCONTACTS CREATED BY INDENTATION

M.Sc. THESIS

Ahmed ULUCA
(509191101)

Department of Physics Engineering

Physics Engineering Programme

Thesis Advisor: Prof. Dr. Hakan Özgür ÖZER

APRIL 2022

İSTANBUL TEKNİK ÜNİVERSİTESİ ★ LİSANSÜSTÜ EĞİTİM ENSTİTÜSÜ

GİRİNTİ İLE OLUŞTURULMUŞ MİKRO ÖLÇEKLİ TEMASLARDA ISIL İLETİMİN İNCELENMESİ

YÜKSEK LİSANS TEZİ

Ahmed ULUCA
(509191101)

Fizik Mühendisliği Anabilim Dalı

Fizik Mühendisliği Programı

Tez Danışmanı: Prof. Dr. Hakan Özgür ÖZER

NİSAN 2022

Ahmed ULUCA, a M.Sc. student of ITU Graduate School student ID 509191101 successfully defended the thesis entitled "INVESTIGATION OF THERMAL CONDUCTION IN MICROCONTACTS CREATED BY INDENTATION", which he/she prepared after fulfilling the requirements specified in the associated legislations, before the jury whose signatures are below.

Thesis Advisor :	**Prof. Dr. Hakan Özgür ÖZER** Istanbul Technical University	.....
Jury Members :	**Prof. Dr. Hakan Özgür ÖZER** Istanbul Technical University	.....
	Prof. Dr. Mehmet Nazmi POSTACIOĞLU Istanbul Technical University	.....
	Prof. Dr. Özhan ÖZATAY Boğaziçi University	.....

Date of Submission : **8 April 2022**
Date of Defense : **28 April 2022**

FOREWORD

I would like to express my most sincere thanks for his guidance to Prof. H. Özgür ÖZER who have given me the opportunities to develop myself in many researches such as this study transformed to my thesis work in Nanomechanics Laboratory of Physics Department since I was a juvenile physics student.
I am also grateful to Prof. Graham CROSS for his intellectual and technical supports from start to finish of this study, without his assistance and lendings there would not be any of this work.
I would like to thank to Prof. Ahmet ORAL for his generous instrumental helps such as Nanomagnetics Instruments HP AFM system and Fiber Interferometry Card that had provided me fast and accurate calibrations of the Indenter.
Many of my friends, for whom I am grateful, have helped me in various ways and times. Dr. Majid Fazeli JADIDI and (to be) Dr. İpen DEMİREL had helped out for many technical aspects at the very beginning of the work, and also I am glad to had worked with them in Nanomechanics Lab. for many years. I would like to thank Dr. James ANNETT for his helps at TCD where these studies started, without his prior works this project would not have developed that much.
I am glad to had many friends in the Lab who have assisted this research in different ways. I would like to express my deepest appreciation for his helps and friendship to Emre ASLAN who contributed to the last version of the mechanical construction. I would like to thank to Seda Nur SÖNMEZ who helped with the calibrations of the setup. I would like to thank to Deniz GÜNSEREN for his helps on the calibration and useful discussions. I would like to thank to Cem SANGA who helped for carrying out first trials with the first versions of experimental setup and progressed the data analysis methods. I am also grateful to E. Asena ÖZER and Egemen ÇATAL for helps on some of the construction trials of the experimental setup.
I am indebted to many engineer friends who had given me many insights for the electronic and mechanical design issues. I would like to thank to M. Emin ATEŞ and Adem Ü. ATEŞ who encouraged me for the programming and helped out on electronic card design. Without their helps I could never progress on the setup except of running just ready to use devices. I am also feeling lucky to have such a friend as H. Anıl ŞAHİN who has provided insights to me on mechanical design concepts and heat transfer.
Last but the most, my family has funded me during all my long stubborn research and simply all of my life. I owe them a debt of gratitude by their names also, to my dearest mother Leyla, my father Ferruh, my sisters Nurcan and Betül and, my brother M. Musa ULUCAs for their material and moral contributions on me.

April 2022 Ahmed ULUCA

TABLE OF CONTENTS

ABBREVIATIONS

2D	**:** Two Dimensional
3D	**:** Three Dimensional
ADC	**:** Analog to Digital Converter
AFM	**:** Atomic Force Microscopy
APA	**:** Amplified Piezoelectric Actuator
ASTM	**:** American Society for Testing and Materials
DAC	**:** Digital to Analog Converter
DAQ	**:** Data Acquisition
FEA	**:** Finite Element Analysis
I2C	**:** Inter-Integrated Circuit-A Serial Synchronous Communication Bus Type
IC	**:** Integrated Circuit
INL	**:** Integral Non-Linearity, a measure of performance of ADCs and DACs
IR	**:** Infrared Autoregressive Conditional Heteroskedasticity
ISO	**:** International Organization for Standardization
MCU	**:** Micro-controller Unit
NI	**:** National Instruments
NV	**:** Nitrogen Vacancy
ODMR	**:** Optically Detected Magnetic Resonance
PCI-e	**:** Peripheral Component Interconnect Express, serial expansion bus for communication between computer and peripheral device
PCR	**:** Periodic Contact Resistance
PID	**:** Proportional Integral Derivative, a feedback control mechanism
PPM	**:** parts-per-million
PWM	**:** Pulse Width Modulation, a power control type by adjusting pulse duration
RC	**:** Indicates Exponential Saturation or Decay Behavior with a Time Constant Exists in a System Similar to a Circuit was Set by Resistor and Capacitor
RMS	**:** Root-Mean-Square
SEM	**:** Scanning Electron Microscopy
SNR	**:** Signal to Noise Ratio
TCC	**:** Thermal Contact Conductance
TCR	**:** Thermal Contact Resistance
TTC	**:** Thermal Time Constant
USART	**:** Universal Synchronous Asynchronous Receiver/Transmitter
USB	**:** Universal Serial Bus
UI	**:** User Interface

SYMBOLS

$\boldsymbol{\alpha}$	**:** Thermal Diffusivity
$\boldsymbol{\beta}$	**:** Dimensionless depth square to area
$\boldsymbol{\Delta T}$	**:** Temperature Difference
$\boldsymbol{\eta}$	**:** Dimensionless Efficiency
$\boldsymbol{\varepsilon}$	**:** Dimensionless Indenter Shape Factor
$\boldsymbol{\sigma}$	**:** Standard Deviation
$\boldsymbol{\Sigma_i}$	**:** Summation over i
$\boldsymbol{\nu}$	**:** Poisson Ratio
$\boldsymbol{\mu}$	**:** Micro
$\boldsymbol{\tau}$	**:** Time Constant (seconds)
$\boldsymbol{\theta}$	**:** Half Angle of Cone
$\boldsymbol{\zeta}$	**:** Displacement to Load Multiplication Factor of Oliver-Pharr Method
a	**:** Radius of a Contact Spot
$\boldsymbol{a_{mean}}$	**:** Mean Radius of Contact Spots
b	**:** Radius of Cylinder Feeding Heat to/from Contact Spot
d	**:** Depth
dt	**:** Time Derivative
dh	**:** Derivative with respect to depth
dX	**:** Differential of quantity X
dB	**:** decibel, gain unit
erf	**:** Error Function
erfc	**:** Complementary Error Function
h	**:** Thermal Surface Conductance (used as depth in Mechanical Model)
$\boldsymbol{h_c}$	**:** Thermal Contact Conductance
k	**:** Thermal Conductivity
$\boldsymbol{k'}$	**:** Harmonic Mean Conductivity
m	**:** Oliver-Pharr Method Depth Exponent of Load
s	**:** seconds
t	**:** time
$\boldsymbol{tan(\theta)}$	**:** Slope of the surface asperities
$\boldsymbol{A_i}$	**:** Area of *i* or area calculated for the case *i*
Al	**:** Aluminium
Au	**:** Gold
Bi	**:** Biot number, ratio of thermal surface to body conductance
C	**:** Capacitance
Cu	**:** Copper
E	**:** Elastic Modulus
$\boldsymbol{E'}$	**:** Effective Modulus
$\boldsymbol{E_r}$	**:** Reduced Modulus
F	**:** Force

$\boldsymbol{F^a}$: Constriction Alleviation Factor
G : Gravity
H : Hardness, Maximum Force per Impression Area
Hz : Hertz, counts in one second
P : Pressure
Q : Heat Rate
R : Resistance
S : Shape Factor
$\boldsymbol{S_c}$: Compressive Strength
$\boldsymbol{S_{con}}$: Contact Stiffness
$\boldsymbol{I_n}$: Modified Bessel Function of First Kind at n-th order
V : Voltage
W : Energy
X : Function of Real to Apparent Area
XY : Directions Perpendicular to Indentation
Z : Indent Direction

LIST OF TABLES

LIST OF FIGURES

INVESTIGATION OF THERMAL CONDUCTION IN MICROCONTACTS CREATED BY INDENTATION

SUMMARY

Thermal contact conduction has been investigated on different scales for many practical and scientific motivations in the literature. Demands for engineering the interfaces are increasing for accurately managing the contact mechanics and heat transfer with miniaturization of the electronics devices. In this study, microcontacts, that are created by indentation, have been investigated with experimental, simulation, and analytical works. The spreading resistance perspective of the disc constriction case has been extended for the studied highly plastic microcontacts of indentation.

Creating the microcontacts and investigating the conductance through them had been realized by indentation of metallic surfaces by specially prepared diamond micro-particles/indenters. Thermal measurements had been realized by mounting thin thermocouples on diamond tips. The experimental setup is home-built with commercial piezo, motor, DAQ utilities, and other miscellaneous devices. PC User Interface and Intercessor Microcontroller Unit had been programmed to properly manage to conduct experiments.

Furthermore, to measure the resistance, we employed an oscillatory experimental procedure and lumped analysis of transient heat transfer. The application of oscillations at different indentation depths has enabled us to extract the RC behavior of the microcontacts created by high plastic deformation. Therefore, the time constant of the contacts can be obtained. Additionally, we could find an effective measure of the thermal diffusivity of the contact through the diamond tip by fitting the change of time constant to depth with the proposed modified constriction models.

Moreover, to analyze and predict the change of the time constant with respect to depth and load, several simulations and calculation work had been pursued. The increase in the contact area by indenter penetration into the sample has been concerned to be suppressed by gradient occurrence along the tip-sample contact. Moreover, with help of the simulations, we deduced the effect of plasticity such as pile-up on the improvement of the indentation contact for the heat transfer can be effective.

Consequently, for the first time, we conducted the periodic contact procedure for the thermal contact of single micro asperity of indentation. The periodic experimental procedure and fin efficiency application to spreading cases for single microcontact are unique parts of this work.

Results with the diamond tip on three different metallic samples showed that the gradient occurrence along the indentation contact can be analyzed with the fin solutions of the literature. Experimental results were fitted properly to a unified function of conic fin and spreading resistance functions. In addition, parameters of the fits can be

deduced for the conductivity and interface conductance. However, state of the results are not sufficient to exactly determine the contact and material parameters due to need for exact parameters for transient analysis and, uncertainties in the properties of the tip and samples.

With help of more precise thermal measurements and indenter systems, this experimental procedure may provide further advances and ease in the investigation of the thermal contacts of many different materials and scales. In addition, for the solid-state thermal interface materials solutions, we deduce that investigation of the geometry optimization for pressure and heat transfer as indicated in this thesis would provide insights into the bottlenecks of the contact heat transfer. Specifically, the gradient occurrence and its effectivity on the overall contact heat transfer should be taken into account for the indentation contacts while improving the contact by plasticity.

GİRİNTİ İLE OLUŞTURULMUŞ MİKRO ÖLÇEKLİ TEMASLARDA ISIL İLETİMİN İNCELENMESİ

ÖZET

Isıl temas direnci, farklı sıcaklıkta tutulan iki cisimin birbirine dokundurulmasıyla ara-yüzeyde meydana gelen ani sıcaklık düşüşünün geçen ısı miktarına oranı olarak tanımlanır. Büyük ölçekli temastaki ısıl direnç, mikro ölçekte katıların birbirine gerçekten temas edememesinden kaynaklanır. Çünkü yüzeyler mikro ölçekte pürüzlüdür, ve genellikle temas eden yüzeylerdeki çıkıntılar bütün yüzeye oranla sadece %1'lik bir gerçek temas yüzeyi oluştururlar. Yani, büyük ölçekte temas eden cisimlerin görünür temas yüzeyi genellikle boşluklardan oluşurken gerçek temas noktaları ise ısıl daraltma/yayılma direncine maruz kalır. Bunun yanında, ısıl sınır direnci olarak isimlendirilen gerçek ara-yüzey (atomik ölçekli) temas direnci ise temas eden katılardaki enerji taşıyıcıların farklılığından meydana gelir ve daralma direncine göre genellikle 3-5 mertebe daha küçüktür.

Dolayısıyla, büyük ölçekte genellikle daralma direncini oluşturan yüzey girintileri ve bu girintilerin mekanik bozunum ile değişimleri incelenir. Isıl daralma ya da yayılım direnci, farklı sıcaklıkta tutulan katılar üzerinde bir boyutlu gerçekleşen ısıl iletimin, temas yüzeyindeki girintiler üzerinden aktarımı sırasında, girintiden, girintiye nispetle sonsuz yarı ortam gibi görülebilecek katı malzemeye geçişi sırasında aniden iki boyutlu ısı iletimine dönüşmesi sonucu ortaya çıkar. Çeşitli geometri ve sınır koşulları için çözümleri olmakla birlikte temas direnci açısından, geometrik benzerliği nedeniyle, genellikle yarı-sonsuz yüzey üzerinde sonlu bir dairesel alanda sabit sıcaklık ya da ısıl akım tutulan çözüm kullanılmaktadır.

Literatürde büyük ölçekteki ısıl temasların yukarıda belirtilen bakış açısı ile yapılagelmiş birçok araştırması mevcuttur. Fakat, bilhassa mikro elektronik cihazlarda birim alana düşen işlemci sayısındaki artış ile günümüzde mikro ve nano ölçekte ısıl iletimin incelenmesi elzem olmuştur. Zira birim alanda işlemci sayısının artışı uygun soğutma düzeneği olmaksızın atıl kalacaktır. İşlemci soğutmada geleneksel yöntem, yonga ile soğutucu metal ara-yüzeyinde termal macun kullanımı ile temasın geliştirilmesi ve yüzey kusurları dolayısıyla oluşan boşlukların doldurulmasıdır. Ancak, termal macunlar hem artan ısıl iletim ihtiyacında hem de bazı sıra dışı kullanım alanlarında (uzay teknolojileri gibi) yetersiz kalmaya başlamıştır. Nitekim macun teknolojisi yerine yeni nesil katı hal arayüzey malzemeleri araştırmaları günümüzde hız kazanmıştır. Katı cisimlerin arasında iyi iletken mikro parçacıkların (elmas vb.) yerleştirilmesi ya da yüzeylerin bilinçli olarak istenilen girintiler ile düzenlenmesi gibi yöntemler 'kuru temas' veya 'tak-çıkar' temaslar için geliştirilmektedir. Dolayısıyla bu çalışmamızla, bahsedilen bilimsel ve teknik motivasyonlarla tek bir mikro ölçekli girintinin üzerinde olduğu yüzeyi bozarak içine girmesi durumunun ısıl temas iletimine katkısı araştırılmıştır.

Literatürde metal-metal temaslarının incelenmesi genellikle yüzey çıkıntılarının ezilerek yayılması durumuna odaklanmıştır. Fakat, biz bu çalışmamızla, tek bir elmas çıkıntının metal yüzeyde girinti oluşturmasının sonuçlarını incelemeye odaklandık. Aslında her iki yaklaşım da görünür temas alanındaki boşlukları kapatmak için, yüzey girintilerinin kuvvet uygulanarak daha çok alana temas etmesini inceler. Ancak, girinti derinliği artırılarak temas alanını arttırmak temas derinliği boyunca bir ısıl meyile sebep olabilir. Bu ısıl meyil, ısı geçişi çalışmalarında daha çok kanat etkenliği bağlamında çalışılmıştır, ve biz de uç geometrimiz için uygun olan etkenlik fonksiyonunu bu çalışmalardan ödünç aldık. Öte yandan, yüksek derecede kalıcı mekanik bozulmaya neden olan, girinti oluşturarak alan artırmanın ısıl temas iletimi açısından yararlı olacağı durumlar da vardır. Mesela, girinti boyunca oluşan taze yüzey boyunca sıkı-uyumlu mekanik temas elde edilir. Ayrıca, kalıcı bozunum dolayısıyla, girinti yapılan malzemedeki sıkışmalar, yüzeyden içeri göçmeye ya da yüzey dışına yığılmaya sebep olabilir. Yüzey dışına yığılma durumunda, girinti derinliğine ek bir temas alanı elde edilmiş olur. Yığılmanın yüzey dışında oluşmasının ısıl meyilden dolayı oluşabilecek iletim etkenliğinin düşüşünü de azaltabileceğini öngörüyoruz.

Velhasıl, bu araştırma ile tek bir mikro uzantının temas ettiği cisimde oluşturduğu esnek ve kalıcı hasarın ısıl iletimi nasıl değiştirdiği incelenmiştir. Bahsedilen incelemenin deneysel olarak gerçekleştirilebilmesi için bir Girinti Cihazı (Indenter) inşa edilmiştir. Cihazımızın kullandığı hazır alınmış piezo, motorlar ve veri toplama birimini diğer birtakım sensör ve araçla beraber uyum içinde kullanabilmek için, mekanik tasarım ve yapıma ek olarak, gerek kullanıcı arayüz programlaması gerek aracı mikroişlemci programlaması uygun elektronik kart tasarımı ile beraber Laboratuvarımızda yapılmıştır. Dolayısıyla, çeşitli deney usul ve yöntemleri temas iletimini farklı derinliklerde girinti oluştururken inceleyebilmek için düzenlenebilmiştir.

Başlıca uygulanan deney usulü geçici rejimde temas zaman sabitini ve dolayısıyla temas direncini çıkarabilmek için girinti oluştuktan sonra girinti yönünde kare dalga şeklinde salınımlar uygulamaktan ibarettir. Bahsedilen kare salınımlar marifetiyle, devinim halinde ani temas kurulumu ve temasın bozulması (uç ile örneğin ayrılması) süreçleri eş süreli olarak gerçekleşir. Dolayısıyla, belirli bir süre boyunca değişmeyen temas alanı ve onu takip eden belirli mesafede temassızlık süreçleri elmas uca yapıştırdığımız termokupl tarafından sıcaklık değişimi olarak ölçülür. Deneylerimizde genel olarak sıcak bir örnek ve görece soğuk bir uç kullandığımız göz önünde bulundurulursa; temas sürecinde ısınma ve ayrılık sürecinde soğuma zaman sabitlerini sıcaklık ölçümünü üstel doyum fonksiyonuna uydurarak buluruz. Üstel doyum fonksiyonunu kullanabilmek için, geçici rejimde toplam kütle yaklaşımı uç-örnek ısıl temas iletiminin yüzeyden taşınıma benzetilmesi suretiyle uyarlanmıştır. Toplam kütle yaklaşımının geçerliliği ise yüzeyden olan ısı iletiminin ucun içinde gerçekleşenden en az bir mertebe daha küçük olduğu denetlenerek belirlenmiştir (Biot yasası). Yani, ucun içinde sıcaklık değişiminin aniden topluca olduğu ve uç içerisinde bir ısıl meyil gerçekleşmediğini varsayıyoruz.

Deney sonuçları, uyguladığımız deney usullerinin temas iletiminin temas derinliği ile değişimini ortaya çıkarmaya yetkin olduğunu göstermiştir. Deneylerimizi çeşitli derinliklerde çok sayıda salınımlar uygulayarak yapmamızın asıl nedeni, termokupl ölçümünün temas eden mikro parçacığın sıcaklık farkını ölçmede yeterli çözünürlük

verememesidir. Literatürde daha önce de büyük ölçekte uygulanmış olan periyodik temas deney analizlerine dayanarak, ucun sıcaklığının yarı-kararlı rejimde olduğunu varsayarız. Dolayısıyla, her bir temas derinliğinde uyguladığımız birçok kare dalga salınımı periyodik ortalama alarak tek bir düşük belirsizlikli üstel doyum ve yokolum verisine dönüştürmüş oluruz. Ortalama almanın yararlı etkisi yanında, temasımızın ilk süreçlerinin henüz yarı-sabit rejime gelememesi beklenebilir, fakat başlangıçtaki geçici rejim toplam salınım süresine nispetle önemsiz kalır. Yine de, daha yüksek çözünürlüklü sıcaklık ölçüm aygıtlarıyla her bir temas ve ayrılık devinimi ayrı ayrı incelenebilseydi araştırmamızı periyodik temas direnci ve kuvvet deviniminin temasa etkisi gibi alanlara genişletebilirdik.

Sonuç olarak, anlatılan deney usulleri ve veri analiz yöntemleri ile kesik koni şeklinde bir elmas uç ile Aluminyum (Al), Altın (Au) ve Bakır (Cu) örnekler üzerinde derinliğe bağlı zaman sabitleri elde ettik. Elde ettiğimiz zaman sabitlerinin yukarıda açıkladığımız temas direnci modellerine uyumluluğunu da test ettik. İlk olarak, kullandığımız toplam kütle yaklaşımının genel kullanımı sabit bir iletim katsayısı ve alana bağlı olduğundan, alan ile lineer bağlı bir ısıl temas iletimi denenmiştir. Veriyi temas alanına uydurduğumuzda, uyum katsayısı olarak ısıl kütle ve temas direncinin çarpım sonucunu elde ederiz. Fakat beklediğimiz gibi, alana bağlı uydurma ölçülen temas zaman sabitlerinin derinlik davranışını doğru vermede yetersiz kalmıştır. Çünkü bahsettiğimiz daralma direnci ve ısıl meyil baskısı, termal iletim katsayısının derinlikle değiştiğini göstermektedir. Ayrıca, alanla uydurulan sabit yüzey iletkenliği sonuçları, elmas uç için genel temas alanının toplam alan oranına %1 iken E+4 mertebesinde ortalama iletim katsayısı değerlerini ortaya çıkardı. Bu sonuçların literatür değerleri ile uyumlu olduğu görülmektedir.

Ardından, yüzey üstündeki daralma direnci tip boyunca uygulanarak daha uygun fonksiyonlar türetilmiştir. Öcelikle ısıl meyil baskısının olmadığı durum verilere uydurulmaya çalışılarak etkin ısıl temas yayılım katsayısı ortaya çıkarılmıştır. Isıl yayılım katsayısı bulabilmemiz, zamana bağlı deney sonuçlarını yorumlamak için de uygun olmuştur. Ucun kesik koni olması nedeniyle, zaman sabiti verileri konik ve silindirik etkenlik fonksiyonları ile değişime uğratılmış daralma direnci modeline de uydurulmaya çalışılmıştır. Özellikle, konik etkenlik fonksiyonunun uyum sabitlerinden geri türettiğimiz ısıl iletim sabitleri elmas ve metallerin harmonik ortalama değerlerine yakınlığı ile dikkat çekmiştir. Bunun yanında, etkenlik fonksiyonunun uyum katsayıları ise dolaylı olarak arayüzeydeki gerçek -atomik ölçekli- iletime dair fikir vermiştir. Arayüzey için bulunan katsayılar mertebe olarak literatür verileriyle uyumlu çıkmıştır. Sonuçlar, silindirik ve konik verimlilik fonksiyonları için sırasıyla E+8'den E+13'e kadar kullanılan uyum fonksiyonuna göre değişen çok yüksek iletkenlik değerleri göstermektedir. Bu sonuçlar da en azından mertebe olarak hem hesaplama hem de literatürdeki deneysel çalışmalarla örtüşmektedir.

Zaman sabiti sonuçları ve yukarıda bahsedilen fonksiyonlara uydurulması, Al, Cu ve Au olarak en düşükten en yükseğe doğru temas iletkenlik sıralaması vermiştir. Bununla birlikte, yüksek plastik girintili kontaklarda, sadece daralmanın harmonik iletkenlik resmini dikkate almak yeterli değildir. Özellikle bakırın altından yaklaşık iki kat daha yüksek sertliği olması dolayısıyla altın-elmas temasının daha uyumlu olduğunu, ve bu

nedenle altınla yapılan deneyler için daha düşük zaman sabiti değerleri elde edildiğini öneriyoruz.

Deneysel incelemelerimize ek olarak, bir ucun ezilerek yüzeye genişlemesiyle katının içinde oyuk oluşturmasının ısıl iletkenlik açısından farklarını kavrayabilmek için birtakım analitik hesaplar ve sonlu elemanlar analizleri (ABAQUS programı ile) de yapılmıştır.

Hesaplama ve simülasyon sonuçları, gradyanın meydana geldiğini ve yüksek arayüz iletkenliğine sahip girintili mikro ölçekli bağlantılar için etkili olduğunu göstermiştir. Buna bağlı olarak, girintinin termal kontaklarına verimlilik fonksiyonunun dahil edilmesinin doğru bir yaklaşım olduğunu ve zaman sabitlerinin deneysel sonuçlarının uyumlandırıldığı model fonksiyonların simülasyon ve analitik hesaplama desteklerine sahip olduğunu vurguladık.

Kontaklar için bahsedilen etkinlik resminin oluşturulmasına destek sağlamanın ötesinde, simülasyon ve hesaplama sonuçları ile en etkili girinti temas derinliği ve şekli bulunmaya çalışılmıştır. Elastik rejim hesaplamaları, daha geniş koni açısının hem basınç minimizasyonu hem de termal gradyan azalması için genellikle daha etkili olduğunu göstermektedir. Ancak simülasyonlara plastisite dahil edildiğinde, yığılma oluşumu nedeniyle daha keskin koninin basınç durumu için daha etkili olduğu bulundu. Daha önemlisi yığın oluşumu, temas yüzeyinin tabanının üzerinde fazladan temas alanı oluşturduğu için ısıl meyil için de yararlı olabilir, bu nedenle termal temasların mikro ölçekli mühendisliği bu yüksek plastisite etkileri ile değerlendirilmelidir.

Ek olarak, daralma/yayılma direnci temas çiftlerinin iletkenliğini bastırmaya başlamadan önce, mükemmel uyumlu silindirik girintinin değişen iletkenlik simülasyonları ile, öncelikle gradyan oluşumunun üstesinden gelinmesi gerektiğini bulduk. Bu nedenle, termal temas iletkenliğini artırmak için yüzey uzantılarının oluşturulması sırasında, elmas ve metalde olduğu gibi özellikle yüksek kaliteli arayüzler için uçta gradyan oluşumunun etkisi hafife alınmamalıdır.

Nihayet, kanat benzerliğinin girintinin termal temaslarının yorumlanmasında kullanılabileceğini ve de kullanılması gerektiğini gördük. Mikro ölçekteki tek pürüz, bu benzersiz yaklaşım ve yeni salınımlı deney tasarımı ile araştırılmıştır. Bu çalışma elmas-metal kontaklardan oluşsa da önerilen deneysel prosedür herhangi bir kontak çifti için uygulanabilir ve literatürle karşılaştırılabilir. Takip edilen veri analizi, kontağın teması veya ayrılma sırası için güvenilir tek termal zaman sabiti sağlamaya odaklanmıştır. Bununla birlikte, sıcaklık ölçüm çözünürlüğündeki iyileştirmelerin yardımıyla, farklı girinti derinliklerinde birçok yarı-sabit durum temas çevriminin ortalaması yerine her bir temas çevrimini çıkarabiliriz. Ayrıca, bahsedilen iyileştirmelerle, ısıl temas iletkenlik tahminleri için deneylerin (yavaş) girinti kısımları ve (kare dalga) darbe etkileri de çıkarılabilecektir.

Neticede, devam eden araştırma çalışmalarına bırakılan birkaç konu vardır. İlk olarak, mekanik özellikleri doğru bir şekilde ölçmek için girinti daha doğru olmalı ve Girinti Cihazı esnekliği azaltılmalıdır. Daha da önemlisi, çoğunlukla cihaz esnekliği sorunlarına bağlı olan girinti derinliği belirsizliği azaltılmalıdır. İkinci olarak, deneylerin termal ölçüm kısmı daha hassas cihazlarla veya tezde belirtildiği gibi elmas üzerinden doğrudan ölçüm ile gerçekleştirilebilir. Deney düzeneğimizin uç sıcaklığı

üzerinde henüz bir kontrolü yoktur, ve uç sıcaklığı sadece ortam ve numune ile temas arasındaki termal denge ile belirlenir, belirli bir girinti seviyesinden sonra, deney sonuçlarında da görüldüğü gibi çözülebilir veri elde etmek imkansız hale gelir. Bu sorun, uca mümkün olduğunca yakın bir soğutucu takılarak kısmen çözülebilir, ancak bu prosedür ve düzenek yoluyla nihayetinde ölçüm yapmak için bir sınır olacaktır. Ancak, sadece bir düşünce deneyi olarak, tüm ucu üzerine bir soğutucu koyarak ve numuneye gömerek, ardından sıcaklığı doğrudan uçtan ölçmek (mesela elmas uçta NV merkezleri aracılığıyla), temas direnci ölçümleri adına bazı sonuçlar verebilir. Gerçekten de benzer durumlar ABAQUS simülasyonları aracılığıyla gösterilmiştir.

1. INTRODUCTION

This study includes investigations of contacts at microscale with an emphasis on heat transfer occurring through them, in order to gain insight into thermal contact conductance (TCC) for high plastic deformation.

Thermal contact resistance (TCR) -the inverse of TCC- is responsible for the sudden change in temperature at the contact surface of two bodies. Contacts have many aspects for investigation ranging from pure geometrical to pure mechanical considerations. Towards nanoscale, the variation of the energy carriers is also an intriguing study area to explain and model the contacts accurately. At that scale, TCR is named as thermal boundary resistance and should be investigated with the help of electronic and phononic energy transfer mechanisms in solids. On the other hand, conductive heat transfer also can be modelled as many adjoining tiny contacting bodies with a thorough atomic-scale investigation of contacts [4]–[8] which is beyond the scope of this thesis.

From a macroscopic perspective, the TCC is modelled as a sum of many heat transfer channels that exhibit spreading (constriction) resistance. It is the prominent model used in the heat transfer engineering community because contact resistance -at least for macro scale- is perceived to be arising from contact flaws. Hence, one can argue that flawless contact should not show any resistance, so it is due to poor contact. In this respect, the model of surfaces should be studied with various surface deviation parameters and deformation of asperities due to load application [9]. For a demonstration of contacts at different sizes, see the Figure 1.1.

Even though thermal contact conduction is a widely studied subject in different scales with the general help of contact mechanics in the analysis [6,10]–[13]; the high plasticity effects are not clearly understood. Furthermore, there is a lack of comprehensive investigation at a single micro-contact level beyond the statistical approach to contacting surfaces with many contact points.

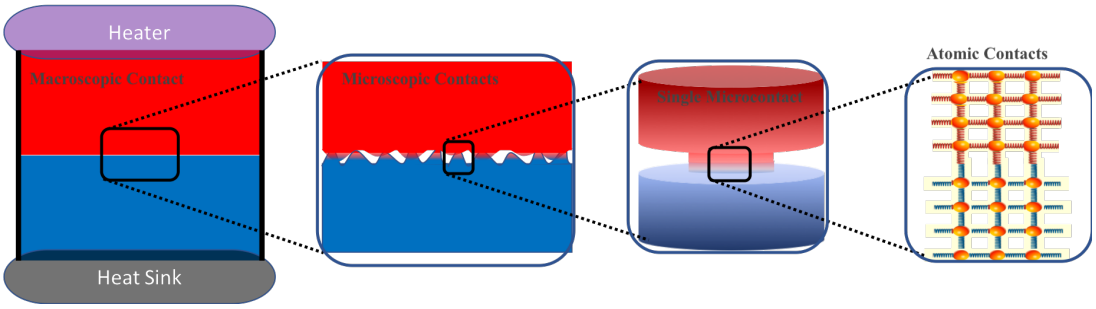

Figure 1.1 : Models of intimate contacts from macro to atomic scales are illustrated.

In addition to scientific motivation, determining thermal contact conduction parameters has become vital for the engineering of small-scale interfaces. Thermal management is a $44.75B per annum business and expected to reach $62.45B in 2026 [14], involving equipment and manufacturing processes designed primarily to cool devices as they operate. Perhaps most famous in the computer CPU industry, the ability to efficiently remove heat is a leading factor governing advances in the processing, storage, and transmission of information by electronic means [15,16]. Even though the increase of processor density in microchips tends to comply with Moore's Law, these high densities of processors become unserviceable without sufficient thermal management due to overheating [1,17]. Hence, investigating new designs for Thermal Interface Materials (TIMs), which are systems intended to overcome thermal conduction bottlenecks at the rough interfaces and joints between thermal management components, is one of the motivations of this thesis. The increase of heat generation and the increasing number of processors by years are demonstrated in Figure 1.2 [1].

The mentioned need for the rapid and efficient cooling need of electronics has led to many designs and material developments in the industry. The well-known solution is thermal pastes to fill the gaps in the contacts. However, sandwiching materials with fillers that provide higher conductivity than air lacks the needs of the industry, for specific cases such as for high-temperature applications and pluggable devices [18]. Especially for the plugs, many contact-separation cycles are required with high heat conduction in optoelectronics and fiber-optics industries [18]–[20]. To meet the dry contact needs, several elastic [19]–[21] and elastoplastic [18] contacts have been tried in recent years.

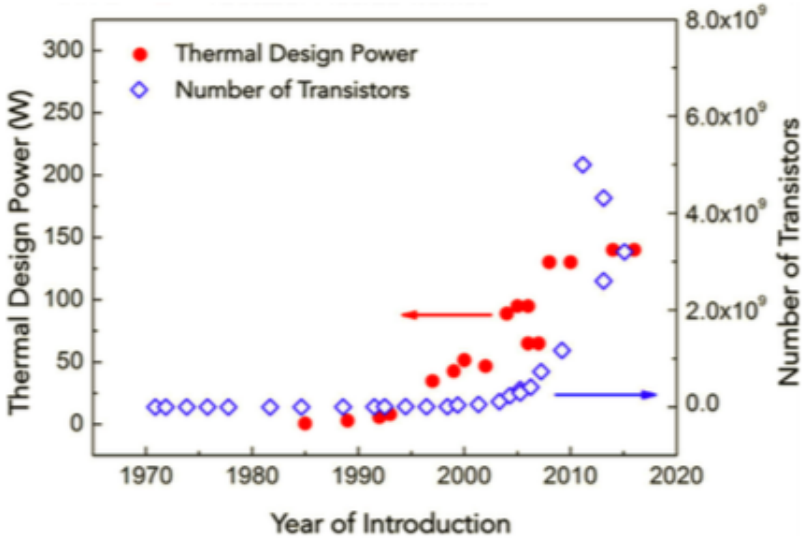

Figure 1.2 : Demonstration of increase by years of Intel MCUs' transistor number (blue) and maximum generated heat by processor (red) (Thermal Design Power) (Graph is taken from [1] that is obtained data from Intel).

Furthermore, transient and oscillatory investigations of contact conductance have unique importance in some applications such as machining processes of materials [22,23]. Local rapid heat production has become a bottleneck in many practical issues. Hence, analyzing the forming stage of contacts at different materials may reveal exact parameters for the machining process itself and developing tools for it.

Therefore, we investigated the thermal transport in a novel way through a single microscopic contact under increasing load. Investigations have led to a new apparatus designed to measure thermal flux under conditions of elastic-plastic contact to high strain. An oscillatory (or "AC") method to determine the thermal contact resistance as a function of tip penetration has been developed, which is particularly novel under conditions of plastic flow in the metal substrate. Although conduction has the dictionary definition of the transfer of energy through bodies without moving them, we are always in quasi-static condition while doing indentation and even in square wave oscillatory measurements. More importantly, the TCC of the contact had been extracted for a constant contact depth with abrupt contact formation by square waves. Hence, we have distinctly observed the conduction heat transfer through the contact.

Mainly, for the purpose of this thesis, thermal contact resistance of micro contacts was aimed to be extracted via temperature rise of a cold tip due to indentation of hot material with the aforementioned oscillatory method. Therefore, a tabletop nano/micro-indenter has been constructed, and transient measurement procedures have been developed to study the emergence of the thermal contact conductance at the incident of forming the micro-contacts. Moreover, computational methods have been employed to optimize the mechanics and geometry of the heat transfer channels and, analytical optimization of channel length and geometry have been investigated by using similarity of the channels to fin problem.

Estimation of the resistance through the oscillatory indentation process needs a transient analysis of temperature change. The utilized time-dependent thermal model can be easily depicted as an analog of charging a capacitor by a battery with a resistor. It is known as the lumped model in heat transfer studies which mainly considers convection parameter through a surface as resistance [2]. However, we have considered contact resistance as the relevant resistance of the lumped system.

1.1 Lumped Analysis of Transient Heat Transfer

The lumped model has been used for transient experimental data fitting. This model counts on only surface heat transfer through a body abiding by Newton's cooling law and assumes an infinite conductance in the body. However, firstly, the internal temperature gradient should be examined whether it is effective or not. This relative internal heat transfer speed is known as Biot number, which is the ratio of surface conductance (hA) to body conductance (kA/L):

$$Bi = \frac{hL}{k} \tag{1.1}$$

To use lumped analysis, generally, Biot number should be smaller than 0.1 [2]. Yet, for the sake of our experiments that have variable contact areas for surface conductance:

$$Bi = \frac{h_c A_c}{kA/L} = \frac{h_c \pi d^2 tan(\theta)/cos(\theta)}{kL\pi tan^2(\theta)} = \frac{h_c d^2}{kLsin(\theta)} \tag{1.2}$$

for a conic indenter with half angle θ, tip height of L, tip conductivity of k, contact conductance (to be found) h_c and indentation depth of d. Therefore, the last derivation

would provide a quick test for accuracy of using Lumped Analysis for a certain conductance calculated at a certain indentation depth.

Then, after showing the validity of the conducting lumped model with the Biot number, we may continue to write the energy balance equation at the surface with the help of Newton's cooling law for surface conductance,

$$Q = hA\Delta T \tag{1.3}$$

so, a simplified form of continuity equation can be written as:

$$C\frac{d\Delta T}{dt} = hA\Delta T \tag{1.4}$$

Finally, a function can be found by inserting initial and boundary conditions as;

$$T(body,t) = T_0 + \Delta T(1 - \exp\frac{-t}{RC}) \tag{1.5}$$

Here 'C' is defined as the heat capacity of the tip and 'R' is the surface heat transfer resistance, so the time constant can be defined as

$$\tau = RC \tag{1.6}$$

The result of the one of the experiments is given in Figure 1.3 as a generic temperature rise and decay curve of indenter tip for a 500 mHz oscillation of tip indented into the sample.

Because the lumped analysis has been used, the time constant is the product of a constant capacitance and resistance as mentioned. There should not be any significant gradient in the body of the probe, so the heat transfer just occurs through surfaces. Newton's cooling law can be used to write the contact resistance with the following:

$$R = \frac{\Delta T}{Q} \tag{1.7}$$

so,

$$R = \frac{1}{h_c A_c} \tag{1.8}$$

As evident in the equation, there are slight differences from the well-known cooling/heating body by immersing it in a fluid. First, it is not the whole area but

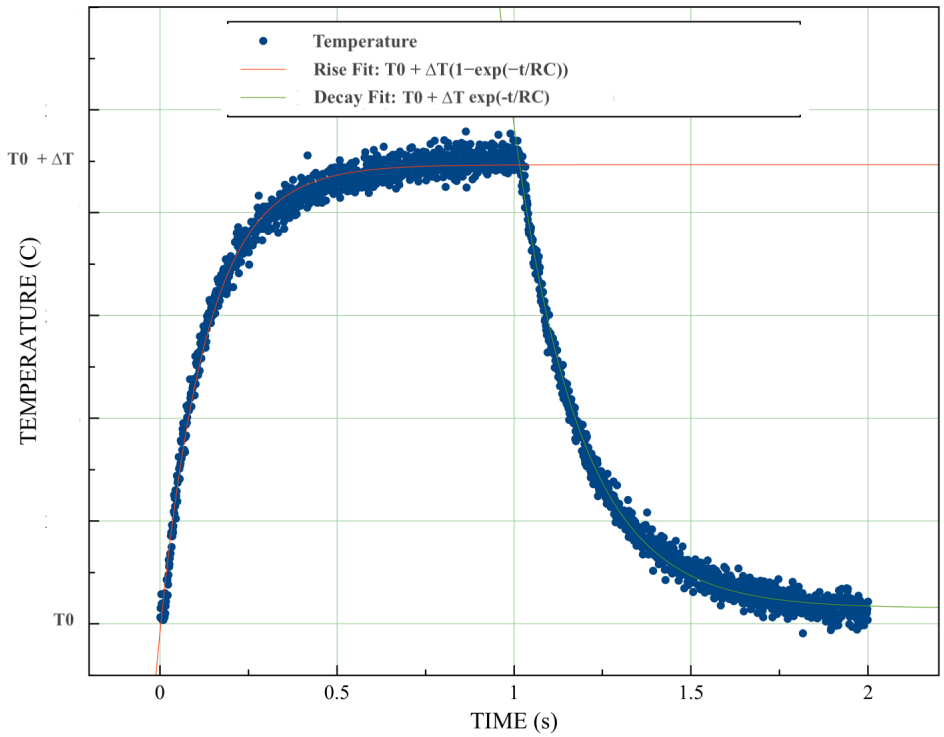

Figure 1.3 : Averaged cycles of tip temperature rise and decay with respect to a 500 mHz square oscillation contact is shown.

the contact area. The contact area stays nearly constant for cyclic contact at one indent level but, going deeper into the surface will increase it with such function:

$$A_c = \beta d^2 \tag{1.9}$$

because, for the conic type indenters contact area increases quadratic with depth with respect to a multiplication factor β depending on half angle. However, this equation should be adjusted for the different shapes of the indenters. If we assume a constant contact conductance (h_c, then time constants τ in eq.(1.6)) that are obtained by fitting to experimental results become:

$$\tau = \frac{C}{h_c A_c} \tag{1.10}$$

After that, we should try to understand how the contact conductance behaves while contact depth is varied.

1.2 Thermal Contact Conductance

For steady-state, there is an abrupt change in temperature at the interface due to contact resistance, similar to Figure 1.4.

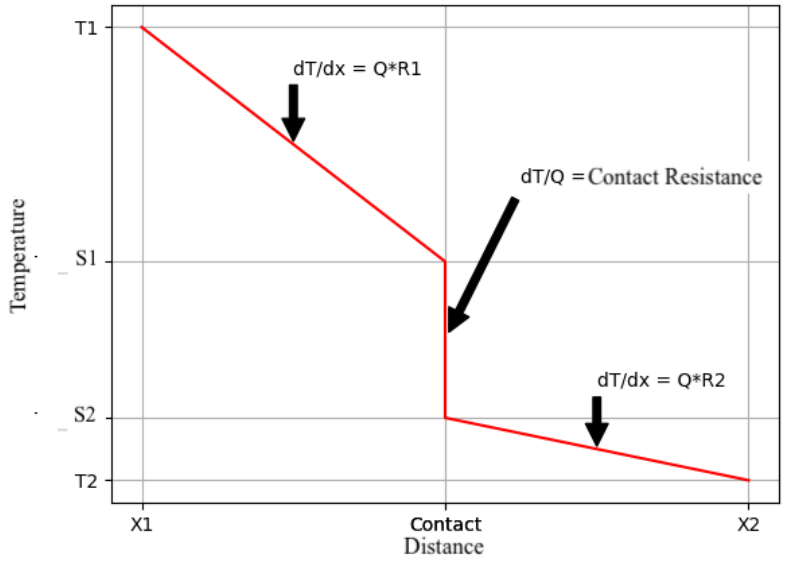

Figure 1.4 : 1D temperature distribution of contacting bodies is plotted for steady state conditions: T1 is the boundary temperature of the first body and S1 is the contact temperature of it while contacting the second body with boundary and surface temperatures of T2 and S2 respectively. Corresponding resistance calculations are shown on the figure for the first body, contact, and the second body as R1, Contact Resistance and R2.

Although it is well-known that energy carrier alternation is the source of the resistance of contacts, for practical reasons it is assumed that there is not any resistance intrinsic to the contact in a large number of studies [10,24,25]. Instead, when contact is accepted to be perfect, the contact resistance has been related to the flaws of the surfaces that prohibit getting them into contact. Therefore, there are many investigations of surface roughness and waviness for analyzing the contact surfaces and heat transfer.

However, if there were not any resistance belonging to contact, the difference between the real contact area to the apparent area would not be enough to define any contact resistance. If the heat could pass through many channels without encountering any resistance, there would not be any apparent resistance yet. Indeed, those many "perfect" contact channels are subjected to resistance due to the abrupt increase of dimensionality of heat transfer. This phenomena is widely studied for non-dimensionalizing the 2D heat transfer from a finite source to infinite body with shape factors for various geometries [25]–[27]. The shape factor 'S' is defined through deriving non-dimensional steady heat rate as [2];

$$Q = SK\Delta T \tag{1.11}$$

so, a 2D resistance is obtained in terms of shape factor with resistance definition in eq. (1.7);

$$R_{2d} = \frac{1}{Sk} \tag{1.12}$$

here the 'k' is the infinite body's conductivity. Moreover, generally the simplest case of an isothermal disc boundary on the surface of a semi-infinite space has been used in TCC studies with a shape factor [9,11]:

$$S = 4a \tag{1.13}$$

where 'a' is the radius of the disc which is depicted in Figure 1.5.

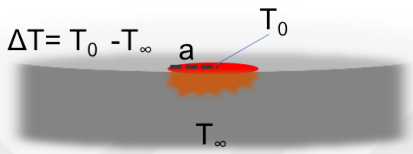

Figure 1.5 : Disc shaped temperature boundary condition (T_0) with radius a on half infinite space of temperature T_∞ is illustrated.

Using resistance definition in eq. (1.7) below formula has been derived (see full derivation specially for contact case in [11]) for a uniform temperature distribution of a disc of radius 'a' on a semi-infinite medium with conductivity k:

$$R = \frac{1}{4ka} \tag{1.14}$$

Then, just making two constriction resistances in series to model contacting asperities with contact radius "a" gives:

$$R = \frac{1}{4k_1 a} + \frac{1}{4k_2 a} = \frac{1}{2a}\frac{k_1 + k_2}{2k_1 k_2} = \frac{1}{2ak'} \tag{1.15}$$

where k_1 and k_2 are the thermal conductivity of two bodies and k' is defined as harmonic mean of conductivity of bodies:

$$k' = \frac{2k_1 k_2}{k_1 + k_2} \tag{1.16}$$

This 2D heat transfer to semi-infinite space is called the spreading resistance and, a reverse perspective can be perceived as the constriction. Although this model of

contact resistance may be limited by 2D contacts, it is widely used with some factors (constriction alleviation factors) [10,11,26,27] to obtain a conductance value of overall surface by summation of many parallel constrictions;

$$R = \left[\Sigma_i \frac{2k' a_i}{F_i^a(a_i/b_i)} \right]^{-1} \tag{1.17}$$

where the $F_i^a\left(\frac{a_i}{b_i}\right)$ is the constriction alleviation factor and a_i is the radius of of ith contact channel between surfaces that can be depicted as below Figure 1.6.

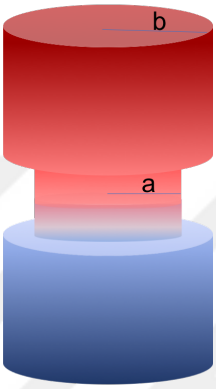

Figure 1.6 : The model of contact with two disc constrictions are put into series contact with feeding cylinders.

The constriction alleviation factor has been used for taking into account that actual heat transfer channels are mainly fed through finite ($r = b$ in Figure 1.6) diameter channels rather than infinite half-space. Hence, the constriction resistance would become smaller than presumed by the resistance of the disc shape factor (eq. (1.14)) on the infinite body, and this profit from loss is generally expressed as a function of the ratio of the radius of contact disc to the radius of the feeding cylinder of contact. In the literature, there are many empirical estimations for the alleviation factors [9,11,26].

After establishing this perspective of the contact heat transfer, remaining is just a careful summation of many constrictions due to surface asperities (as illustrated in Figure 1.7). In this manner, contact resistance can be estimated by the surface parameters and variation of them under contact pressure. Several widely used contact conductance formulations with the surface parameters have been explained below. The main conductance formula is derived by using the ratio of real area to the apparent area of contacts with the help of evaluating surface profiles in a probabilistic manner

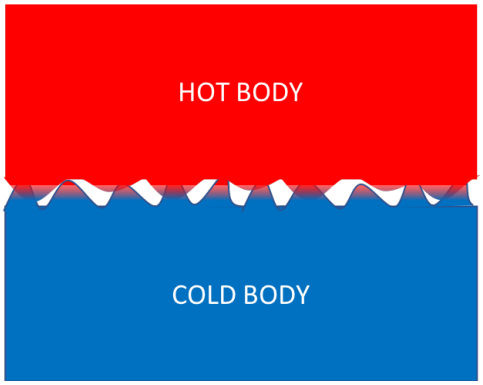

Figure 1.7 : Contact heat transfer through asperities of surfaces is illustrated.

to estimate coinciding asperities as [11];

$$h = \frac{1}{2\pi}\frac{k'\psi}{\sigma F^a} exp[-X] \tag{1.18}$$

where k' is the harmonic mean conductivity (see (1.16)), ψ is the root-mean-square (RMS) of absolute slopes of the surface asperities, σ is the RMS of the standard deviation of the asperity heights of the surfaces, F is the alleviation factor and X is a function of the ratio of real area A_r to apparent area A:

$$X = \left[erfc^{-1}\left(\frac{2A_r}{A}\right)\right]^2 \tag{1.19}$$

where $erfc$ is the complementary error function $(1 - erf)$. Then, several deformation analysis for the plastic and elastic contacts had been derived to demonstrate the development of the actual area with the applied load, so the contact conductance can be given in terms of the contact pressure and the other mentioned surface parameters such as [28]:

$$Plastic : h = 1.13\frac{k\psi}{\sigma}\left[\frac{P}{H}\right]^{0.94} \tag{1.20}$$

$$Elastic : h = 1.55\frac{\psi}{\sigma}\left[\frac{P\sqrt{2}}{E\psi}\right]^{0.94} \tag{1.21}$$

where H is the hardness of the softer material, P is the contact pressure and, E is the effective modulus of the elasticity of the surfaces that can be denoted as:

$$E = 2\left[\left[\frac{1-\nu_1}{E_1}\right] + \left[\frac{1-\nu_2}{E_2}\right]\right]^{-1} \tag{1.22}$$

where E_1 and E_2 are the Young Moduli and, ν_1 and ν_2 are the Poisson's ratio of the two contacting materials. Furthermore, some experimental correlations had been made

by researchers such as [29];

$$h = \frac{2}{1-F^a}\frac{k}{\pi\lambda_1\lambda_2}\left[\frac{P}{H}\right]^{0.5} \tag{1.23}$$

where F is the Roess Constriction Alleviation Factor [11], λ_1 and λ_2 are wavelengths of the crossed ridges and, this correlation was derived for contact of surfaces consist of the crossed ridges [11]. In 1970 Mal'kov [30] developed a TCC relation for mean radius of contact spots:

$$h = 0.118\frac{k\psi}{a_{mean}}\left[\frac{PC_1}{3S_c}\right]^{0.66} \tag{1.24}$$

where a_{mean} is average radius of contact spots, S_c is the compressive strength and C_1 is "micro projection" factor. This correlation works well with the low loads but, increase in the load exponent has been seen by the increasing loads [11]. In addition, Tien (1968) [31] introduced a useful TCC-pressure relation by using the surface and material parameters for nominally flat surfaces:

$$h = 0.55\frac{k\psi}{\sigma}\left[\frac{P}{H}\right]^{0.85} \tag{1.25}$$

There are many other comprehensive works on correlation factors which can be summarized in the two main groups such that; either the load exponent is about 0.7 (0.66-0.75) or about 0.95 [11]. Lastly, in the Ph.D. thesis of Bahrami [13], it is suggested that namely "micro" and "macro" resistances (for sphere to flat surface contact) should be evaluated to get a total TCR by defining a joint resistance R_j [11];

$$R_j = \frac{0.18H^*}{k'LP} + \frac{(1-a_L/b_L)^{1.5}}{2k'a_L} \tag{1.26}$$

where H^* is microhardness, the a_L/b_L ratio is similar to alleviation factor ratio of radii of contact to feeding tube with a_L here is being "macro" contact radius, and L is;

$$L = \frac{b_L^2}{\sigma/\psi} \tag{1.27}$$

On the other hand, we are investigating the deformation of the surface elastically and plastically at the micro-level by a single asperity (indenter tip). Therefore, the probabilistic approach and the 2D disc contact approach may be insufficient in terms of contact conductance of the indenter that provides a volumetric 3D contact shape. Therefore, fin effectiveness similarity has been conducted to assess the

dimensionality difference. There would be a non-negligible thermal gradient along with the contact, which might slightly suppress the positive contribution to the conductance of increasing contact area as increasing indentation depth. Therefore, it would be practical to define a dimensionless efficiency function η to properly take into account the yield of the area increase on heat transfer rate:

$$A_{effective} = A_c \eta(d) = \beta d^2 \eta(d) \tag{1.28}$$

Subsequently, the constriction resistance (eq. (1.15)) can be converted to the conductance to write the thermal time constant (eq. (1.10)) with respect to indentation depth by writing constriction disc radius as a linear function of depth (such as "αd" for a conic indenter shape):

$$h_c = \frac{2k'\alpha}{\beta d} \tag{1.29}$$

so, putting together the equations for τ (eq. (1.6) and resistance (eq. (1.8)) with inserting above derivations of effective area and contact conductance results in below function for time constant;

$$\tau(d) = \frac{C}{h_c A_{effective}} = C\frac{1}{2k'd\alpha\eta(d)} \tag{1.30}$$

Finally, the efficiency factor in equation (1.30) will be examined.

1.2.1 Efficiency function and fin similarity

The idea of decreasing resistance by increasing the surface area in surface conductance studies is well known as the fin problem [2]. Here our study is similar; surface area of contact is increased by increasing the indent depth that extends the surface while decreasing the temperature difference along with the contact. However, establishing a similarity between the two approaches has a drawback as the contact conductance itself increases with the contact area (constriction decreases). Even so, the below fin solution for the cylindrical and conical fin cases will be tried to be placed in the τ (eq. (1.30)).

Efficiency function for finned surfaces is derived from continuity equation with a 1D approximation for body conduction with alternating surface conduction at the boundaries. If a body's surface is held at a temperature different from the surrounding

medium, heat transfer through the surface occurs. As depicted in the eq. (1.3), the heat rate depends on the area, temperature difference, and conductance parameter. Therefore, protrusions (fins) need to be produced on the surface, if one needs to increase the heat rate with a restricted base surface area and constant system parameters (temperature difference ΔT,and surface conductance coefficient h). However, the heat transfer through the surface decreases itself by decreasing the temperature difference between the surrounding interface and fin along with the fin extension due to uncontrolled temperature along the length of the fin. From the equation (1.3), one can discern the trade-off between decreasing ΔT along the fin while increasing the area by the fin extension. An illustration of the heat transfer along the surface extension by simultaneous conduction and convection can be seen in Figure 1.8.

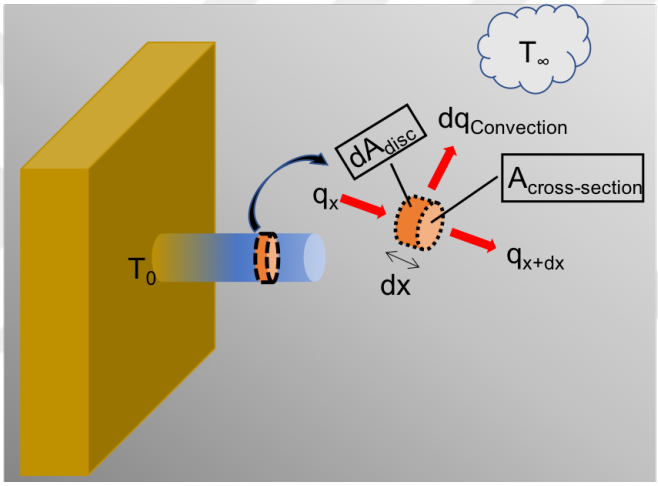

Figure 1.8 : Energy continuity of extended surface [2] is illustrated with heat (q_x) is transferred by conduction along a cylindrical fin through cross-sectional area ($A_{cross-section}$) in a unit length of dx while convection heat transfer ($dq_{convection}$) occurs through side infinitesimal area (dA_{disc}).

There are efficiency functions for various fin geometries such as conical and cylinder (flat punch). We will consider in the calculations and for the fit trials these two shapes. For cylinder [2]:

$$\eta_{cylinder} = \frac{tanh(mL)}{mL} \tag{1.31}$$

L is $\left(d + \frac{a}{2}\right)$, where d is the depth and a is the radius of the cylinder extension, and m is

$$m = \sqrt{\frac{2h}{ka}} \tag{1.32}$$

Thus, time constant for cylindrical extension can be written as below:

$$\tau = \frac{c_1}{tanh(c_2(d+a/2))}\frac{(d+a/2)}{d} \tag{1.33}$$

where,

$$c_1 = \frac{C}{2k'\alpha}\sqrt{\frac{2h}{ka}} \tag{1.34}$$

and,

$$c_2 = \sqrt{\frac{2h}{ka}} \tag{1.35}$$

For conic geometry [2]:

$$\eta_{cone}(d) = \frac{2}{md}\frac{I_2(md)}{I_1(md)} \tag{1.36}$$

$$m = \sqrt{\frac{2h}{ka}} = \sqrt{\frac{2h}{ktan(\theta)d}} \tag{1.37}$$

where d is depth and a is radius of the fin that can be written in terms of the depth with help of half cone angle θ. The I_1 and I_2 are the Modified Bessel functions of first kind at first and second order respectively. When we look just these special functions' graphs; we see more rapidly increase with decreasing order of function. Hence, division of the order of the second to the one always gives a number smaller than one.

Consequently, we may put the conical efficiency function in the time constant function τ (eq. (1.30)):

$$\tau = \frac{c_1}{\sqrt{d}}\frac{I_1(c_2\sqrt{d})}{I_2(c_2\sqrt{d})} \tag{1.38}$$

where

$$c_1 = \frac{C}{k'\alpha}\sqrt{\frac{h}{8ktan(\theta)}} \tag{1.39}$$

and,

$$c_2 = \sqrt{\frac{8h}{ktan(\theta)}} \tag{1.40}$$

Therefore, we will seek for parameters c_1 and c_2 by fitting the experimental time constant results to equations for cylindrical (1.33) or conical (1.38) cases due to the shape of the indenter. Moreover, some calculations had been pursued for the analyse of the saturation behavior in the contact heat transfer, and simulation results are also supported for finding the transition from effective to saturated contact depth. In

addition, the parameters c_1 and c_2 have emerged an interesting parameter together such as;

$$\frac{c_2}{c_1} = p_0 \frac{k'}{C} \tag{1.41}$$

which is dimensionally equivalent to thermal diffusivity per volume. Hence, the ratio of the efficiency fit parameters c_2 to c_1 may provide an effective thermal diffusivity for the contact with a proportionality constant p_0.

On the other hand, the surface conductance coefficient (h) has been intentionally kept as a constant parameter that is thought to be the intrinsic nanoscale interface conductance while the contact conductance of microscale contact has determined by spreading effect and efficiency function together for the sake of the fin similarity context of contacts created by indentation.

In a work of Majumdar et.al. [24], the difference of increase in conductance between the deformation of asperities and asperities deforming the surface for a macroscopic contact case had been investigated. They found that the case of deformation of the asperities (flattening of asperities by crushing them) is more effective than asperities creating channels in the softer body. Then, it is related to the increase of contact area is higher for flattening asperities than for the hard asperities indenting the soft body due to lower load exponent for asperity penetrating case. However, the result was seen maybe also partially affected by the fin effectiveness function as conducted above in this study.

On the other hand, recently in a study of R.Dou et.al [18], the efficiency function of contact fins is deduced by decreasing pressure on the sidewalls due to inclination to the normal force. Even so, the mentioned study had examined millimeter size fins, therefore, they could write the pressure relation for the contact (equation (1.25) was used; just the pressure exponent of 0.85 is indicated in the paper) which is obtained through a statistical deformation analysis of surfaces to include real to apparent area difference as mentioned above. Besides, our work here is just the single asperity establishes a micro contact that is one of the asperities of averaged many of the statistical studies'. Thus, it is found tricky to use the average formula for conductance for the sake of a single micro contact case for varying indentation depths.

Lastly, it is important to emphasize that the mentioned gradient occurrence along the tip should be thought to be just in a very narrow regime and, it is just to put an alternative explanation for the saturation behavior of contact conductance. Yet, we do not assume any significant gradient along the tip that is much bigger than the contacting volume. Hence, the lumped analysis application for the measurement does not contradict using the fin approach for the contact analysis as long as the Biot number is kept small (see eq. (1.2)). The effectiveness of the gradient occurrence in contact will be shown with simulation results too.

1.2.2 Conductance of gap

The term thermal contact conductance is generally used for the sum of solid spots' conductance (which is explained above with constriction resistance) and conductance of gap [9,11,32]. Unless the gaps between solid spots are evacuated, confined gas contributes to conduction [33]. Moreover, radiation heat transfer through surfaces occurs, but generally it can be neglected for near room temperature [11,34].

For our study, it is not intended to extract gas gap conductance parameters and, we have not controlled the medium. However, the steady-state thermal equilibrium before oscillatory experiments is achieved via conduction to the tip that is exposed to convection of stable ambient air (with system isolation), and because indenters have been held close to sample surfaces, gas gap conductance from the encountered surface of the sample to the tip occurs. Hence, each contact and separation cycle of periodic experiments, i.e. for a hot sample and cold tip, heating time constants (contact sequences) are related to solid spot conductance, and cooling down (separation sequences) time constants are related to a gap conductance equilibrium with medium (tip holder system's conduction and its equilibrium by convection of surrounding room temperature medium).

Moreover, the change of time constants with respect to the contact depth depends on the increase in the contact area and decrease in the gap at the same time. However, indenting shallower levels, which is a small fraction of an overall tip, could allow us to neglect the decreasing gas gap conductance term for the contact intervals. Finally, for the assessment of the results of this thesis, time constants for the contacting periods of

the oscillations will be interpreted as a direct measure of the thermal contact resistance for a given indent level. On the other hand, the time constants belonging to the non-contacting periods will be assessed for the equilibrium of the gap conductance with medium.

Below Figure 1.9 gives a picture of the thermal system with explicit illustrations of the tip, sample and contact resistances as gap resistance R_{Gap}, contact resistance $R_{Contact}$, convective resistance R_{Conv}, conduction resistance R_{Cond}, radiation resistance R_{Rad}. The sample holder, heater, tip holder and actuator resistances are indicated with their equivalent total resistances (R_{eq}), heat provided by heater is given as Q, generally stable actuator temperature is given as $T_{actuator}$ and stable ambient temperature is shown as $T_{ambient}$.

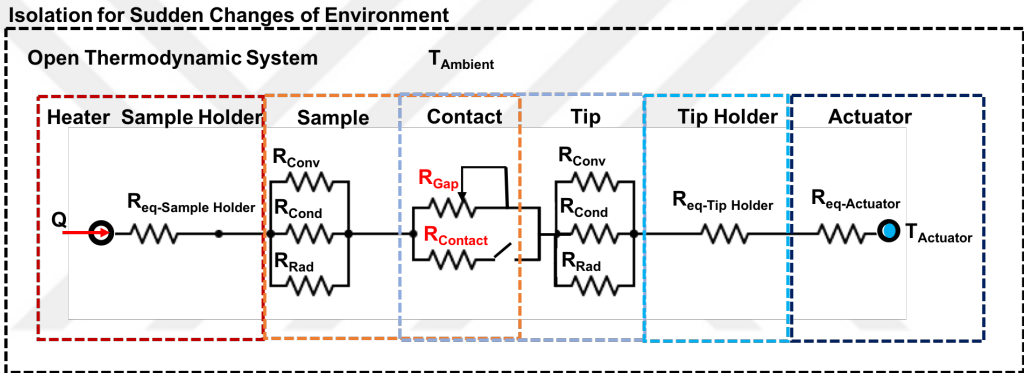

Figure 1.9 : Electric circuit scheme equivalent illustration of thermal equilibrium is drawn.

1.3 Mechanical Model

There are many thorough explanations of the mechanical deformation process of indentation in literature [35]–[37]. However, for the scope of the thesis, investigation of the contacts between generally a high modulus tip and a high plastic body (i.e. diamond tip and copper sample, respectively) should be carried out. Hence, plastic flow during indentation needs to be analyzed. Since there is not an easy and accurate way to approach plastic flow analytically, we did simulations to understand this process. Moreover, this thesis is based on a more experimental investigation of thermal contact conductance so, mechanical interpretations are mainly made for optimizing load versus contact area as indenting into the surface. In Figure 1.10, an indentation

cycle is depicted with several important quantities for extracting material properties emphasized on it. These parameters are going to be explained and used for the sake of extracting sample properties.

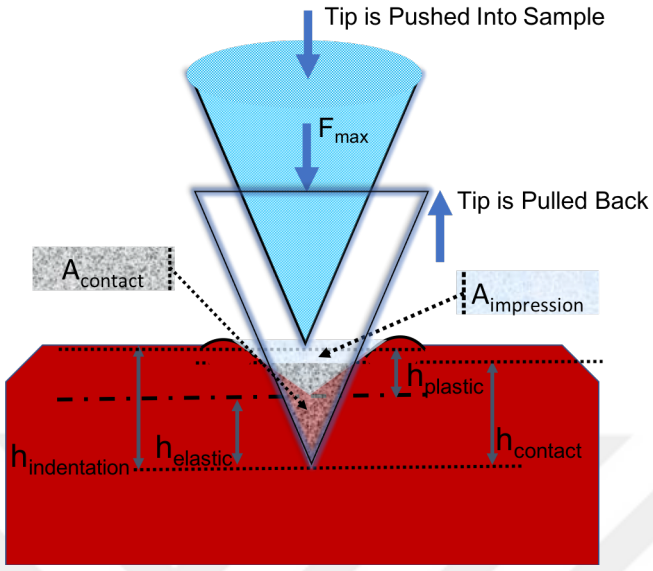

Figure 1.10 : Indentation of a sample with a conical tip is demonstrated.

Basically, an indentation is the application of force through a body to another that might be firstly viewed as a system composed of two springs in series. This first stage is nothing but an elastic relation that complies with Hook's Law and a contact stiffness parameter (a measure of Young's Modulus of materials) can be derived. Moreover, a more complete understanding should include the shape of the indenter so, Hertzian contact relations and pinned geometry derivations of Sneddon's are used [36,38,39]. Analytical expressions for relating applied force to depth vary with the shape of the indenter such as; exponent of depth varies from 1 to 2 while changing the tip from flat punch to a pointy (conic) one. To demonstrate that clearly, the below functions are given [39]:

$$Flat\ \ Punch : F = 2aEd \tag{1.42}$$

$$Spherical : F = \frac{4}{3}E\sqrt{R}d^{1.5} \tag{1.43}$$

$$Conic : F = \frac{2Etan(\theta)}{\pi}d^2 \tag{1.44}$$

where ‘a’ is the cylindrical flat punch’s radius, ‘R’ is the radius of spherical indenter and ‘θ’ is the half angle of cone and ‘E’ is the reduced modulus as:

$$E = \left[\left[\frac{1-\nu_{tip}}{E_{tip}} \right] + \left[\frac{1-\nu_{sample}}{E_{sample}} \right] \right]^{-1} \tag{1.45}$$

Here E_{tip} and E_{sample} are elastic moduli of tip and sample respectively and ν_{tip} and ν_{sample} are Poisson’s ratio of tip and sample respectively. Poisson’s ratio provides including strains (ε) due to material’s compression/stretching in the perpendicular axes to indent with respect to indentation load which can be expressed for isotropic material:

$$\nu = -\frac{\varepsilon_{perpendicular}}{\varepsilon_{indent}} \tag{1.46}$$

Furthermore, it is evident that the spring-like approach has a limit as beyond a certain deformation, bodies do not turn back to their initial positions. This certain deformation for materials is named as Yield Point and plastic deformation begins after that point. However, because of the singularities at various indenter geometries (especially pointed indenters), there are rapidly emerging high-stress regions that cause to be about all the deformation is elastoplastic. Hence, elastic contact properties cannot be deduced from directly loading portions of F-d curves. Besides, the unloading part of an indentation cycle would give the contact stiffness since returning material should demonstrate mostly elastic behavior. Hence, by differentiating the Sneddon’s formula for an elastic contact of conical tip and flat specimen (eq.1.44):

$$S \equiv \frac{dF}{dh} = 2\frac{2Etan(\theta)}{\pi}h => \frac{dF}{dh} = 2F/h \tag{1.47}$$

To avoid confusion with differential “d”, “h” is used as depth in above equation and “S_{con}" is defined as contact stiffness. This equation indicates that slope of F-d is twice of the load to displacement ratio for any point if only the contact is purely elastic. Moreover, by using the Sneddon’s depth to contact radius relation:

$$h = \frac{\pi}{2}acot(\beta) \tag{1.48}$$

in eq. 1.47:

$$\frac{dF}{dh} = 2\frac{2Etan(\theta)}{\pi}\frac{\pi}{2}acot(\theta)\frac{dF}{dh} = 2Ea \tag{1.49}$$

Note that, on that step, the same stiffness relation has been obtained for both cone and flat punch which can be easily seen by differentiating eq.(1.42). Moreover, to obtain a more general equation for any axis-symmetric indenter, the projected area should be used as:

$$A = \pi a^2 \tag{1.50}$$

Therefore, we may write the last version of contact stiffness:

$$S_{con} = \frac{dF}{dh} = 2E\sqrt{\frac{A}{\pi}} \tag{1.51}$$

and hence the reduced modulus 'E' can be found in terms of projected area and contact stiffness:

$$E = \frac{\sqrt{\pi}}{2}\frac{S_{con}}{\sqrt{A}} \tag{1.52}$$

A generic contact stiffness curve can be seen at Fig.1.11(a) as curve 'c' which is calculated from first %10 of the unloading F-d curve (curve 'b' in Fig.1.11).

Calculation of contact stiffness by finding tangent to start of (d $<$ %10) retraction curve is known as Doerner-Nix method [40]. However, Oliver and Pharr (1992) [37] has shown that it is vulnerable to errors because of using flat punch elastic relation (shown in eq.1.49). They discovered a power-law method which is more appropriate to use for axis-symmetric indenters. The method enables to use about all unloading F-d curve with a least-square fitting to such function:

$$F = \zeta(d - d_f)^m \tag{1.53}$$

where 'ζ' and 'm' are constants of indentation and '$(d - d_f)$' is the elastic recovery depth. Hence, they claim a power-law relation which is similar to given elastic relations of the load-displacement equations [1.42,1.43,1.44] (where the exponent m is in between 1 and 2). Moreover, the geometrical assumption of the exponent is also interpreted as a flat punch of varying radius by depth. Then, the remaining is just taking the first derivative of the fitted function and evaluating at the maximum force to extract contact stiffness properly.

In addition, the hardness of the materials can be derived from the plastic regime of deformation. Generally, the ratio of maximum applied force of indentation

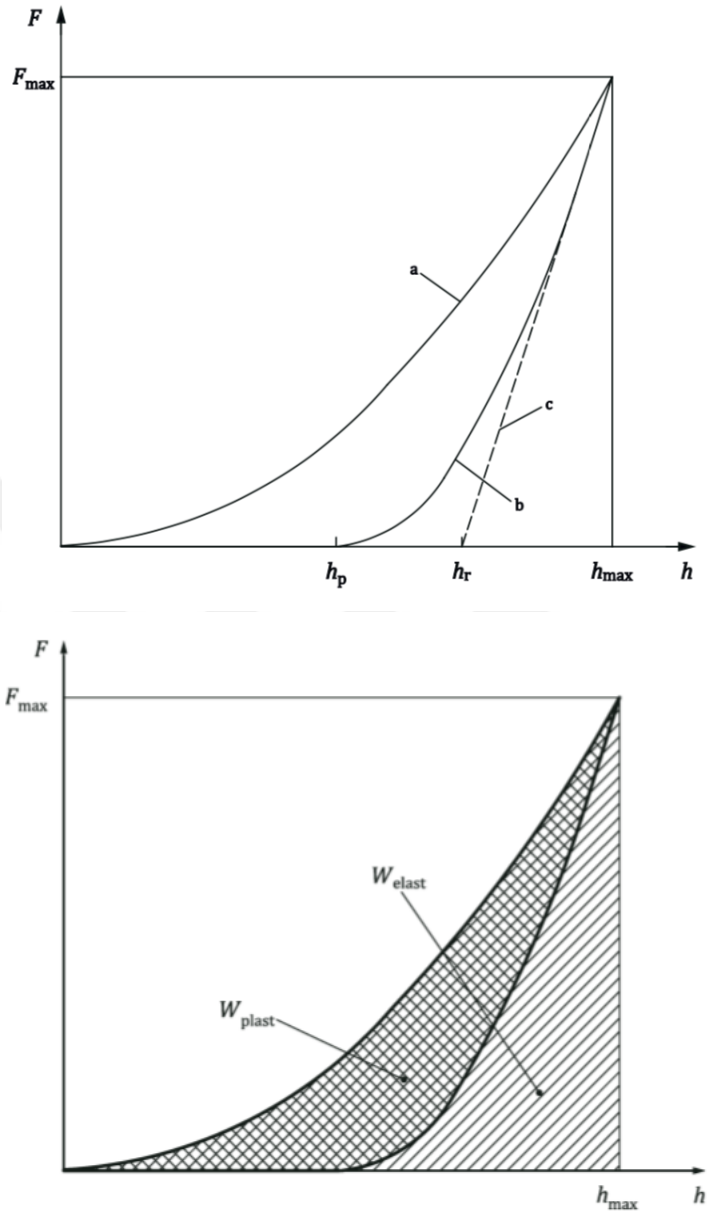

Figure 1.11 : A Generic Elastic-Plastic Indentation's Load versus Depth (F-d) Graph [3], on the left Indentation up to load F_{max} and depth h_{max}, plastic deformation depth h_p is indicated as zero load point of unload curve and tangent's intersection to displacement axis h_r or contact depth for flat punch. (a: Loading F-d Curve, b: Unloading F-d Curve, c: Tangent to Unloading Curve at F_{max}), and on the right Demonstration of Elastic (W_{elast}) and Plastic (W_{plast}) Energies of Indentation Process

to impression area gives hardness of the material and, there are several highly standardized measurement procedures in engineering communities [3,39]. Hardness can be expressed as :

$$H = \frac{F_{max}}{A_{impression}} \tag{1.54}$$

Consequently, measurement of maximum force while indenting the surface with a high modulus tip and inspecting the impression remained after the indentation with a microscopy method (optical, AFM, SEM) would provide the hardness information of indented material.

Even though microscopy inspection is still important for especially calibration of tip shape and instrument, there has been no need to direct measurement of the residual sunken area with the standardization of Instrumented Indentation technique [3,36,37]. Instead of direct measurement of the impression area, analysis of unloading F-d curves enables calculation of contact area for the known depth-to-area function of the tip [41]. In curve c of Figure 1.11(a), a typical F-d curve and contact depth (h_c) analysis by calculation of the first derivative of retraction F-d is shown. As emphasized earlier, the Oliver-Pharr method would give more accurate results for the contact depth evaluation too. Here, with the emphasis on plasticity, we may try to analyze where the flat punch assumption has been made (as Doerner-Nix). Utilizing the Sneddon's formulae for just elastic portions in equations 1.47 and 1.48 caused to end up with the eq.1.49. Yet, with the awareness of elastoplastic contact, we should take into account the relations for outside the contact such that [37]:

$$h_{out} = \frac{\pi - 2}{\pi}(h - h_{plastic}) \tag{1.55}$$

and the stiffness (S_{con})-force (F) relation as:

$$h - h_{plastic} = 2\frac{F}{S_{con}} \tag{1.56}$$

whereas $h_{plastic}$ indicates the impression depth after unloading and, h_{out} is the depth of untouched deformation (bending) that is outside of the contact radius. Using above relations, again a general expression for axis-symmetric indenters can be derived as:

$$h_{out} = \varepsilon\frac{F}{S_{con}} \tag{1.57}$$

where the ε is the geometrical parameter for indenters, ε is 1 for flat punch and smaller than 1 (about 0.7) for the more conforming shapes (i.e. cone, sphere, etc.). Chudoba and Jennett (2008) [36] introduced a more accurate calculation of ε factor with load dependence addition and radial contributions. Consequently, using the ε factor and power-law fitting, the unloading curve analysis can be resulted by finding the contact depth $h_{contact}$ at maximum load:

$$h_{contact} = h_{indentation} - \varepsilon(h_{indentation} - h_r) \tag{1.58}$$

$h_{indentation}$ is the maximum depth indented and h_r is the intersection of stiffness curve to displacement axis (as shown in Figure1.11). With the information of the contact depth, a different Hardness (H_{O-P}) can be estimated with using projected contact area and maximum load rather than actual impression area and maximum load:

$$H_{O-P} = \frac{F_{max}}{A_{projected}(h_{contact})} \tag{1.59}$$

The ability to estimate the projected area by just contact depth for hardness calculations stems from the absence of radial elastic recovery of corners of the impression when a pointed tip with sharp corners indents (Berkovich). However, there may be deviations for smooth-rounded tips [37]. Moreover, employing the indentation energies' ratio (elastic/total), elastic modulus to hardness ratio of the sample can be extracted [35,36].

It may be useful to mention that the ductile materials like metals show plasticity while the brittle materials show very little or no plastic deformation by exhibiting an incident fracture. The elastic regime is generally the first 1% of strain during deformation and, easy glide, work hardening, necking, and fracture processes follow due to rearrangement of the defects in ductile solids while conducting a pulling test. However, in compression tests of ductile materials, the necking and the fracture regimes are rarely seen but enormous plastic shear flow results as pile-up or sink-in generally.

The analyse of deformations for the sake of transient contact conductance investigations have some discrepancies with standardized indentation test. Thermal gradient through the contact is normally an effect wanted to be overcome for even elevated temperature indentation tests. Wheeler et.al. [42] have conducted

comprehensive experiments for thermal drift issue at the elevated temperature Nanoindentation. However, for our case we intentionally provide a quasi-steady state condition between the tip and sample to measure contact heat transfer. Consequently, experiments of the thesis are not conducted for neither the nano range nor the exact deformation analysis. Furthermore, plastic deformation is a function of temperature due to the defects in the solids responsible for the plasticity [43]. Thus, one should be aware that our results predict parameters at the average temperature of contact during the experiments. Moreover, studying the temperature effects on ductile-brittle transition, plastic strain and pop-in events while loading have been intriguing research areas with the developments in the instrumentation [42,44].

Beyond the elastic property extraction through retraction sequences, adhesion parameters can be also extracted via the proposed setup [45]. However, studying the adhesion effects on the TCC is beyond the scope of this thesis.

By controlling the geometry and the load, one can optimize the contact area. Consequently, the TCC can be controlled by adjusting the contact area which has been our main goal in mechanical analyses and simulations in this study.

1.4 Periodic Contacts

In this study, a periodical contact procedure has been developed for mainly the ease of the transient analysis. The procedure consists of slow indentation followed by square wave application which is similar to an impact test rather than an indentation. Impact tests are well-standardized experiments to examine the failure modes of materials (ASTM E2248-18). Moreover, there are cyclic indentation tests rather than impact testing that are focused on extracting loss and storage moduli of specimens. As indicated above, here our perspective is neither of them.

In addition, periodic contacts are important on the TCC studies too. Thermal periodic contact resistance subject is by itself a research area with scientific and industrial importance. There is even an early work that just investigates periodic contact resistance without taking into account the TCR using an analogue computer in 1970 [46]. After that study, Howard and Sutton [47] included TCR in their analogue study,

then Howard published experimental work on the subject [48]. In those studies, Periodic Contact Resistance (PCR) and TCR parameterized with an effective length as if the material length was elongated to cause an extra resistance. They also found that the effect of TCR becomes more pronounced while the total contact time is increased. Moreover, they had tried to correlate the two constrictions of electrical and thermal in the experiments, and reached a discrepancy between small effective radius of contact found by electrical resistance when compared to higher heat flow. This problem could not be solved, but electrical insulating film or gas gap conduction effect had been suggested [48]. The wear effect had been also observed for many impact cycles as emergence of oxidation and sediments at the contact. However, impact effect for the first contact creation had been found advantageous rather than slowly pressing due to local bonding between metals can take place with high impact [48].

After the mentioned pioneering works, analytical and numerical studies on the transient and periodic contacts also had been gained importance [49,50]. In the proceeding experimental studies, effect of duty cycle of oscillatory contact and contacting same/different materials have been investigated [51]–[54]. Those works of Moses and Johnson (1989) [52] and Moses and Dodd (1990) [53] have provided us insights on the data analysis and quasi-steady condition that will be mentioned at the Experimental Results [Ch.3]. Moreover, for short contact times, they claim that the TCC can not reach to its steady value, so high frequency applications needs transient parameters to be extracted.

Later, Williamson and Majumdar (1992) had conducted an extensive work of the deformation mode effects on TCC [24]. They argued that prior investigations had lacked determining accurately the deformation mode, and they proposed fractal surface analysis prior to experiments and load cycling during the experiments. The load cycling enables to make judgement about the deformation mode as mentioned in the Mechanical Model section [Ch.1.3]. Unloading parts of the cycles would elucidate the ratio of deformation modes along one cycle. Consequently, they found that at the first loading cycle mostly the plastic deformation has been observed with some elastic contribution, but after the first cycle mostly the elastic deformation takes place. Moreover, they had also observed the temperature effect on the plasticity

while elevated temperatures continued to demonstrate plastic deformation after the first cycle. Lastly, they investigated the difference of the plastic deformations of asperity penetration and asperity crushing in the contact that we mentioned in the last part of the Fin Efficiency discussion [1.2.1].

Following the prior works, Wahid and Madhusudana (2002) conducted research for revealing overloading and load cycling effects on the TCC [55]. They had shed light into hysteresis effect (higher TCC while unloading) and dependency of the increase in TCC to the number of cycles. Generally, their results agree with the prior work of Williamson and Majumdar [24] on the variation of the plastic deformation occurrence rate along the cycles. Furthermore, the hysteresis effect had been related to maintained conforming after loading step due to elastic recovery during the unloading. The improvement on the TCC due to the load cycling had credited to mainly plastic deformation, so they deduce the sharp decrease in the improvement after the first cycles related to the end of the plastic deformation. Lastly, they had found interesting results on the effects of the surface roughness with overloading. Although the intuitive expectation may be more improvement due to plasticity should occur for the rough surfaces, they had found that for the smooth flat metal contacts both the initial TCC and increase in the TCC are greater than for the rough metal contacts.

Periodic macro-contacts had been analytically investigated by Wang and Degiovanni (2002) with the development of the method of quadrupoles [56]. The hardness of the periodic and transient experiments stems from finding solution to the ill-posed inverse heat transfer problem that provides the conductance parameter. There are several approaches in the literature besides of the using mentioned analytical approaches. James V. Beck (1985) [57] has developed methods to solve parameter estimation besides of many other problems, and beyond that he suggested optimization methods for the experiments to investigate transient parameters [58,59]. Based on his procedures many extensive researches on the periodic and transient contact conductance have been become possible by easy thermocouple measurements. Beyond thermocouples, IR thermography based experimental methods and inverse heat transfer methods have been developed by Fieberg and Kneer since 2006 [60] based on Beck's works [57], and many seminal works with IR have followed [23,61]–[64]. The lastly

mentioned solutions of experimental interpretations and parameter extractions are based on the division of the experimental data to reasonable sequences to fit a model function.

Moreover, Goudrazi and Shojaeefard (2009) have improved experimental techniques with emphasize on the contact frequency [65], it is followed by developing methods to model the periodic contact experiments based on inverse heat transfer solution by conjugate gradient and transfer function identification methods [65]–[68].

As introduced here and may be found more, there are extensive studies on the transient contact heat transfer with focus of periodic contacts. On the other hand, our objective is to show conductance change by penetration of a single asperity. The purpose of periodic contact application in this study is to provide resolvable temperature data for lumped analysis. Consequently, relying on the prior periodic contact works, we extract TTC of various depth of indentation by averaging many oscillations. Furthermore up to our knowledge, with this study, we are conducting contact heat transfer experiments for single microcontact with periodic contact/transient approach for the first time.

2. EXPERIMENTAL SETUP AND PROCEDURE

To measure the thermal time constant of the contacts while controlling the contact depth and the sample temperature, an experimental setup has been constructed, and several experimental procedures have been developed for extracting results via the mentioned lumped analysis [1.1] of exponential fit to tip temperature.

In the literature one can find many approaches to measure thermal contact resistance (TCR) [58,69,70]. These can be investigated in sections such as contact depth/load scale, heat transfer regime (steady/transient) and, for the transient whether it is the heat in transient regime or contact itself. Furthermore, periodic behavior of contacts has been also an intriguing research area as mentioned in the Introduction [1.4].

In this study, contact size/depth dependent measurement of thermal contact resistance has been realized by Nanoindentation (Instrumented Indentation) technique. Controlled and repeatable contacts had been created via indenting metallic surfaces with a variety of materials (mainly diamond or materials harder than metals). However, standards of Nanoindentation (ISO 14577) has been used as a guide to development of the system and protocols, so it is not intended to be strictly in boundaries of standards. Moreover, our proposed experimental protocols need to be in transient heat regime, and from this point of view the setup is similar to explained in longitudinal conductivity measurement standard ASTM E1225–09. On the other hand, heat transfer side of the measurement had been accomplished via thermocouple measurement through the tip side. Thermocouple's own need of contact and total heat capacity effect on time constant measurements have given struggles for comparison of different tips. However, it is a technical issue to solve for any measurement system and here we suggest a couple of self-calibration solutions. In addition, other possible measurement techniques for heat transfer have been studied, and will be mentioned.

Nevertheless, main experimental setup consists of a thin (25 um) thermocouple attached to the indenter tip that is positioned and loaded to sample surface with a

homemade indenter system. Experimental procedures will be mentioned thoroughly in the next sections and, may vary but; generally ISO standard complied slow speed -quasi static- approach to surface and indenting a desired depth followed by sub 1 Hz square wave oscillation in surface has been used for gathering exponential rise and decay of temperature through the tips. Indeed, square wave type oscillation is not easily interpretable in terms of mechanical characterization-indentation- but, it is found to be the easiest way to obtain data for fitting exponential-lumped capacitance model. Because, square wave oscillations provide incident contact establishment and vanishing periodically so, we can have on/off states for contact in various depths. This general procedure makes easy to analyze data and, as long as Biot number allows [1.1], we do not need to know exact heat transfer process through the contact to the thermocouple.

Moreover, many oscillations at a sole indent level has been applied for increasing signal to noise ratio but, it has also been found useful for analyzing change of RC along with periodic contacts. Increase of signal-to-noise ratio (SNR) is not directly dependent to number of oscillations but, it statistically increases the probability of taking low noise individual temperature rise/decay data through each cycle 3.1.2. However, there is a more important factor that affects experiments in the manner of SNR. Because the main extraction of time constant is due to change of temperature between two positions of the tip, the oscillation amplitude directly determines the amount of signal. Consequently, to increase the visibility of each time constant of periodically created contacts, one should increase the difference between on and off (contact) state's steady (or quasi steady) temperatures. Hence, there are many other ways to do that such as increasing initial temperature difference or putting system in a vacuum to eliminate/adjust interstitial gas conduction (though it may make worse) or increasing wave period for allowing the tip to be closer to steady temperature.

To conclude, the setup is home-built including the software and electronics. We can examine the experimental setup in four main parts such as Nano-positioning (loading) unit, coarse positioning unit with mechanical design issues, software/hardware control unit, and data acquisition (DAQ) unit. However, beyond all mentioned main blocks of the rig, it should be appreciated that preparation of tip (as a probe with thermocouple

attachment) and sample is crucial -preliminary- part of the thermal time constant experiments.

2.1 Tip and Sample Preparation

Utilizing diamond as an indenter tip is widely studied and, is commercially established too. Hence, it is not a surprise to use in our experiments, but diamond also provides superior thermal conductance and that makes it a suitable thermal probe for the TCC experiments. It should be noted that, here the "probe" itself creates contact with another material so, measurement is directly dependent on contact between probe/tip and sample.

In addition, the temperature has been measured through thermo-electric (Seebeck) effect via thermocouple. Therefore, the actual probe for temperature is the thermocouple that attached to diamond/or any tip while (see Fig. 2.1), the measurement of contact resistance derived from transient behavior of that temperature as mentioned in the Introduction (Lumped Analysis). However, information of the contact is obtained via the tip-to-thermocouple lumped capacitance so, for the sake of TCR measurements, the term probe is defined as all system from tip to thermocouple.

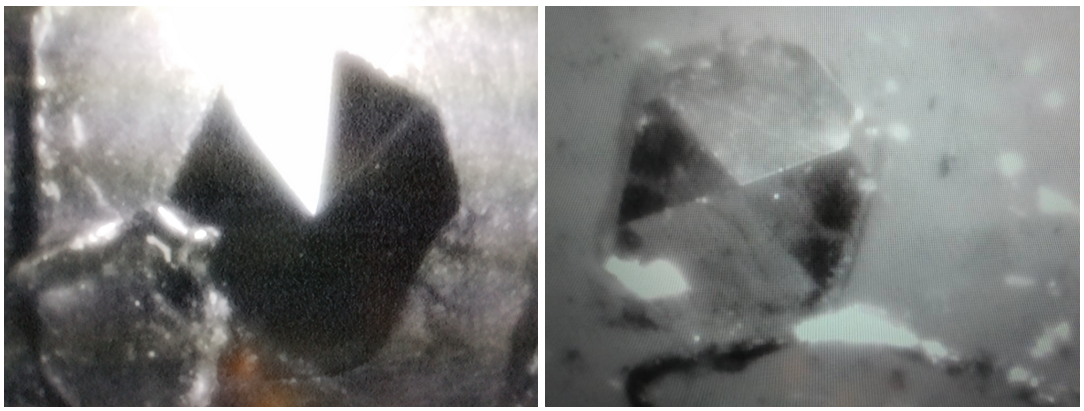

Figure 2.1 : Examples of prepared tips, 25 μm thermocouple is attached to conical indenter tip (left) and diamond micro particle (right).

Indenter tips have been prepared by attaching them to a screw for connecting firmly to actuator. Then, a thin thermocouple (size 25 μm) is glued as close as possible to the end of tip. Moreover, gluing has been made carefully to avoid any loose contact and leakage of glue between the thermocouple and the tip. To accomplish this in a

reproducible way, a tip preparation system was set up with micro-positioners. Utilizing a long working distance camera with the setup has enabled us to position thermocouple at desired location of the tips. After attachment is done, a rough trial for thermal contact of thermocouple to tip is conducted with a multimeter at tip preparation setup. A sudden touch to tip with a hot needle shows a rapid increase on voltage/temperature measurement that gives us a sense for connection quality. However, the real test is made on system with contact experiments directly, and gives generally 100 ms to 1 second time constants of the series of contacts.

Here, it may be useful to mention about a study of Loulou and Bardon (2001) [71] that focused on analysing the TCC while spot welding process. They have a similar transient measurement approach with thermocouples that are soldered to copper electrode plate so that they could achieve intrinsic junction. They provide an equation for the time constant of measurement:

$$t = 44\frac{r^2}{\alpha} \tag{2.1}$$

where 'r' is the radius of the thermocouple wire and α is the diffusivity of the soldered medium (copper for their case). Another more extensive analytical and experimental study for the transient beahvior of intrinsic contacts with thermocouples gives the relation for 95% of the saturation [72]:

$$t \approx 31.83\frac{r^2}{\alpha}\frac{k_t}{k} \tag{2.2}$$

here k_t and k are the conductivities of thermocouple and (hot) junction medium respectively. Indeed, our measurement is not intrinsic, but we may use these relations to estimate an upper limit for transient measurement through diamond contact to thermocouple. Because, intrinsic contacts have been found the fastest response above all junction types. A comparison between intrinsic and surface-bonded thermocouple junction was given as about more than five times higher time constant in the surface-bonded (welded) type [72]. However, our thermocouple junction was neither welded nor soldered, but just mechanical contact supported by glue due to hardness of surface bonding to diamond tips. Yet, we may estimate some upper limits for the response time of thermocouple by using above formula as about 0.6 μs for "intrinsic"

diamond-thermocouple contact. Moreover, results demonstrates that we are able to find overall time constants as low as 100 ms with contact heat transfer through sample to thermocouple via diamond tips.

For sample preparation, cleaning the surfaces with propanol and blowing nitrogen are common for all samples. Prior to cleaning, grinding and/or pressing to reduce surface roughness and waviness is employed in several cases. Nevertheless, surfaces intentionally have been kept non-uniform to demonstrate effects of plasticity more distinctly. Subsequently, the sample is mounted on the sample holder by a mounting adhesive (Crystalbond 509 Electron Microscopy Sciences) which is stiff enough to use at temperatures below 70 Celcius (about 8 MPa of Tensile Strength [73]).

This measurement setup with thermocouples is very versatile for employing various shapes of tips as long as the tip size allows. However, thermocouple itself suffers from constriction issue when it is conducted for measurement through surface of a body. Hence, using thermocouple to measure contact conductance of a tip-sample interface through tip surface temperature variation is actually measurement of series of two contacts. Nevertheless, as long as thermocouple stands still on the tip's surface, results of time constant measurements would be interpretable in terms of tip-sample contact quality.

In addition to thermocouple measurements, there are various methods for extracting temperature of contacts/near contacts. For instance, since they are already in use for indentation experiments widely, diamonds can be utilized as temperature sensors that would be accomplishing two measurements with one probe. To make diamonds reliable temperature sensors, boron doped diamonds can be employed due to their electrical resistivity that is dependent to temperature, or creating NV centers in diamond tips enables optically detected magnetic resonance (ODMR) measurements which has phononic contributions that provides high sensitivity temperature measurements. Because, nowadays with technical improvements it is easy to utilize NV diamond as temperature probe [74,75]. There are also 3ω and transient thermo-reflectance methods which have complexities to use with indentation experiments [70,76]. The other common method is using IR radiation to measure

temperature but, generally it is employed for macroscale measurements due to spot size / resolution issues [61]. Hence, thermocouples seem to be the most useful for trying all material types and sizes with ease. Furthermore, if commercial thermocouple thickness exceeds the tip sizes, a thermocouple could be created directly on desired material via coating techniques, so the major part of the constriction issue and size limits could be overcome at the same time [77].

2.2 Coarse Positioning System and Mechanical Design

Making repeatable experiments on samples depends on coarse positioning system as much as fine positioning/loading unit. Because, there should be a single approach mechanism to take actuator/tip to the starting point of contacts with a known error in an interval. So, we can assess many indent results in an acceptable uncertainty. Moreover, there should also be robust and stiff positioner in the perpendicular directions to indent (XY positioner stage).

Design of coarse positioner system is not only about positioning prior to indent but includes mechanical design requirements of an indenter. With sensors and tip/sample holders being on it, a coarse positioning system should provide accurate and precise motion and stability. In the beginning of this work, a single 3-axis micro-positioner had been employed for coarse positioning system. However, small range of movement by manual adjustment emerged problems for the ease of use and repeatability. Moreover, possibly low stiffness of positioner could cause errors for data analysis.

Considering above mentioned issues, orthogonal to indentation positioning system (KT180-DC XY stage) was implemented with a robust attachment on to 2 cm thick, 30x30 cm^2 wide Al-5083 base plate. A bar type loadcell, with sample holder and sample heater unit are on it, was firmly mounted on the XY stage. The displacement of the loadcell due to its finite stiffness is subtracted from the total displacement in order to extract true indentation depth.

The vertical direction (indent axis) coarse positioning has been developed homemade by utilizing a linear rail system with worm screw. The linear rail and the screw was connected together with a specially machined Al-5083 part and linear rail car.

Table 2.1 : Coarse positioning system parameters are given.

Positioner Direction	Range	Resolution	Axial Strength	Tensile Strength	Min. Drive Speed
XY Stage	50 mm	+/- 5.5 μm	60 N	25 N	2.5 mm/s
Z Stage	200 mm	625 nm	10 N	3 N	12.5 $\mu m/s$

There is a screw hole for the actuator at the end of the specially designed moving part. In addition, Nema-17 step motor holds the trapezoidal worm screw for consistent motorized positioning.

Coarse positioning system parameters are given in the Table 2.1.

Furthermore, an SEM holder has been employed for a heater compatible sample holder and, was seated on a machined special designed metal-alloy disc that is screwed on loadcell.

Heater unit is a Joule (Resistive) Heater which is also a common part for 3D printers' extruders. The resistance part was mounted inside sample holder to distribute temperature evenly. Intercessor MCU and a power transistor provides PWM drive of heater for fast and secure adjustment of sample temperature. Overall experimental setup can be understood with the help of drawing in Figure 2.2.

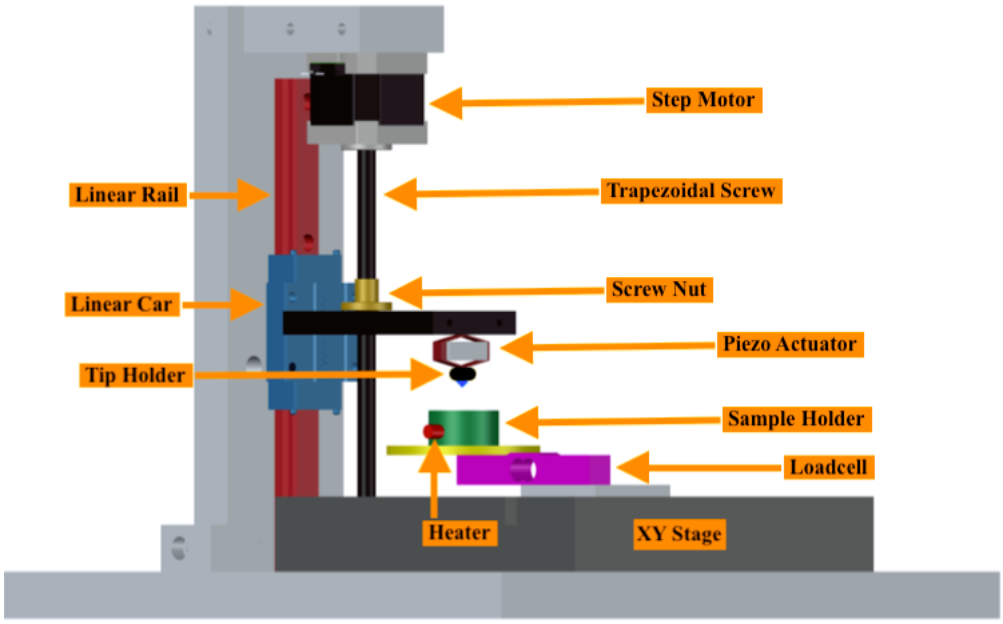

Figure 2.2 : Indenter Setup elements is shown in the drawing.

Last but not the least, isolation has been constructed since the beginning, from the selection of all parts to designing the system . In addition, black-opaque plexiglass covers have been used to block the IR radiation and air flow so that thermal experiments have not been affected by sudden external changes. Moreover, cabling has been made carefully with wrapping grounded cables on the signal carrying cables due to expected noise of motors, resistive heater and external electromagnetic noises.

2.3 Nano-positioning and Loading System

Since the main objective is to create micro-contacts in a repeatable and precise way while heating the sample, firstly, a piezo actuator (CEDRAT APA-60S) was implemented. Amplified Piezo Actuator (APA) is manufactured by piezo stacks that stuck on each other with a parallel electrical connection. Hence, controlling applied voltage in high resolution gives precise motion and, fine stacked structure provides to exert high load. Moreover, for actuation stability and safety, a stainless-steel case covers the stacks like a bow. Therefore, an APA is stainless steel double sided high stiffness spring/bow that is stretched by piezo stacks placed in the middle of the two sides. The driving system of CEDRAT APA is shown in Figure 2.3.

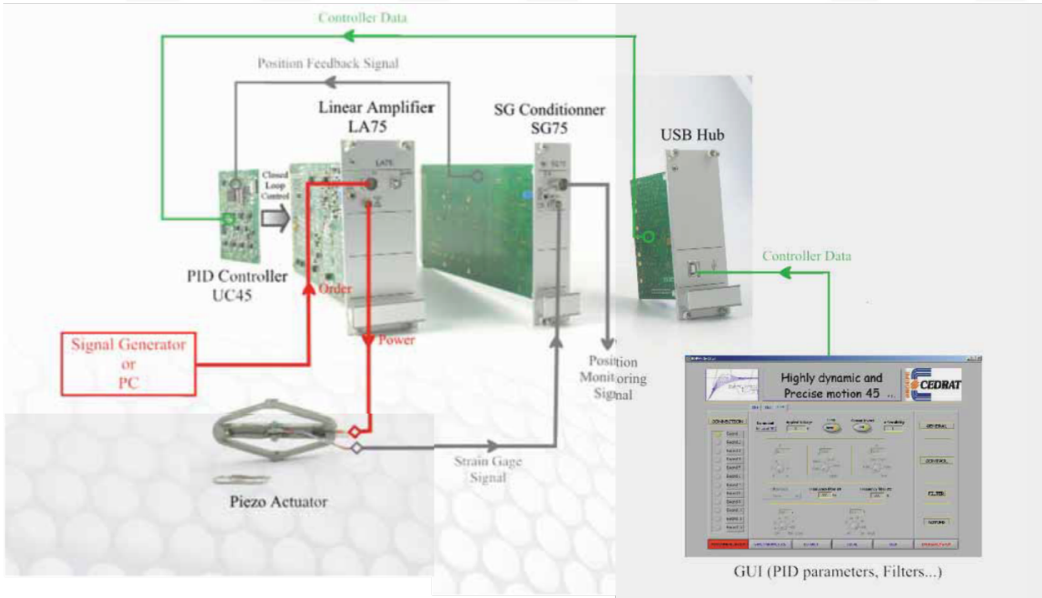

Figure 2.3 : CEDRAT APA Driving System is shown as pictures of electronic cards (middle), APA (bottom left) and GUI (bottom right).

2.4 Control Software and Electronics

The APA has been controlled by a control card (UC45) that governs 26 dB gain linear amplifier (LA75). There is a built-in full-bridge strain gauge on piezo stacks that provides direct information about displacement of piezo. Moreover, a calibrated strain gauge conditioner (SG75) has been used to amplify and scale strain gauge signal. Thus, acquiring output of SG75 provides direct measurement of the tip that is located on steel case of APA. Fiber interferometry calibrations had been made for converting voltage value to real displacement that will be given in Calibrations section. Moreover, SG75 is connected to UC45 to enable PID feedback mechanism that is very useful for eliminating piezo hysteresis effects (see Fig. 2.4 for schematic of PID mechanism).

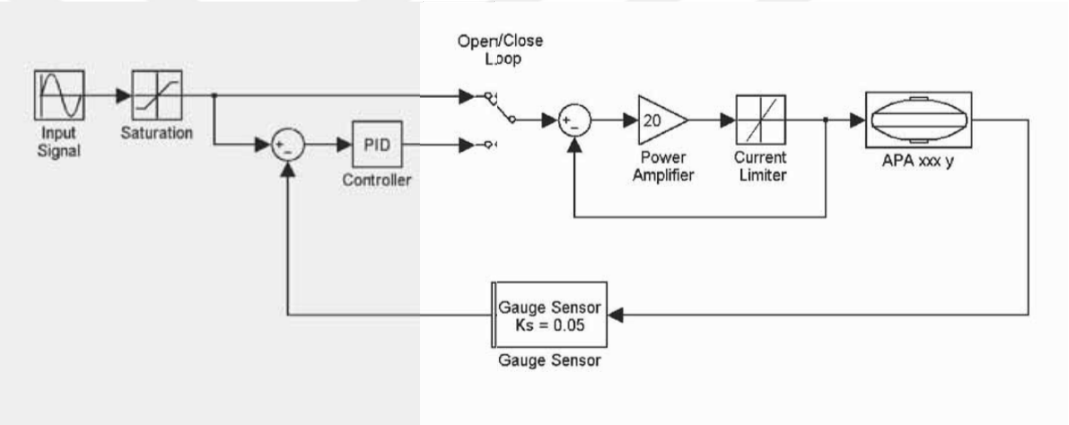

Figure 2.4 : CEDRAT APA open/close loop control is shown as a schematic.

However, with all above mentioned superior properties, UC45 and its commercial software is found to be much behind the capability of making controlled Nano/micro indents. There was need for continuous communication with UC45 and give new voltage/position value. To make it happen, firstly serial communication between PC software and UC45 was decrypted by using a "serial sniffer" program. After understanding the communication protocol for start-up and all other commands and replies for them, a basic C# program in "dot Net" environment had been written. However, after establishing the contact we needed to make oscillations which depends on precise timing, a PC program was found to be hard to make it properly. Therefore, a micro controller was implemented as an intercessor that takes packaged orders and

applies them with respect to the written algorithms. But, while USB connection to PC is easy, MCU (intercessor) to MCU (UC45) USB connection is not easy to implement, and it is also needless. A direct connection to the UC45 card's microprocessor's USART pins from intercessor MCU's relevant pins solved the issue. Only the communication speed restriction caused by the UC45 has remained unsolved. The minimum time needed between adjacent successful orders is 50 ms to not to break the connection. The intercessor MCU-electronic card design, its program, PC User Interface (UI), data analysis programs and, many sensors and motor driver implementations will be mentioned in this section.

Although the idea of writing a software emerged from insufficiency of APA's commercial software, it transformed the project to make an Indenter independent from many commercial ready to use tools from driving to sensing elements. Even so, in the scope of this work, we will mention the Control Software and Electronics unit as an integration unit between UI and actuation. System schematic is shown in Figure 2.5.

Controlling the experimentation consists of approaching to pre-defined surface location with controlling the load and executing certain indents while holding the sample at a certain temperature. Hence, a microprocessor (STM32F407) has been programmed to utilize our lab's facilities to satisfy mentioned requirements.

The core element of indentation is control of APA-60S for nanoscale resolution movement. Control of APA for the scope of this thesis has been pursued mutually through CEDRAT's LA75 amplifier that is governed by the UC45 microcontroller and the programmed MCU (intercessor). The chain of command for positioning the APA starts with a serial communication between intercessor MCU and UC45 that consists of -1 to 7.5 volts non-amplified voltage information with 6 digit precision. After that, UC45 creates determined voltage for the LA75, and LA75 amplifies the input voltage with 26 dB gain. Finally, amplified voltage is supplied to piezo via the LA75 output.

While controlling the displacement with supplied voltage is enough for this initial stage setup, movement should be controlled via a PID feedback loop by measurement of strain of piezo. CEDRAT provides this control mechanism with a built-in strain gauge on actuator and (SG75) conditioner card connected to (UC45) control card.

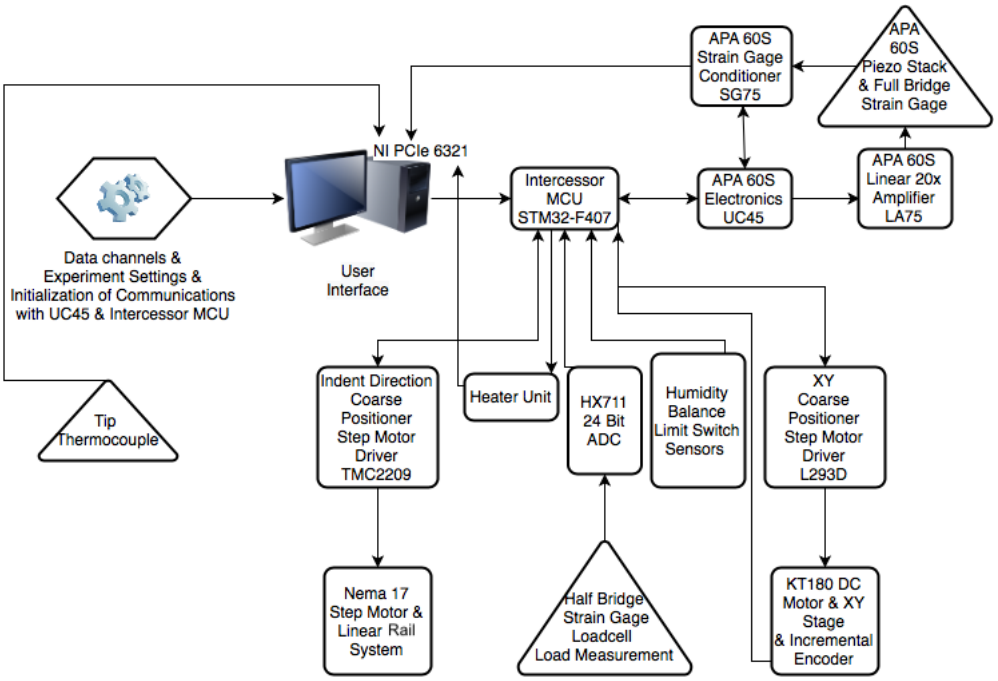

Figure 2.5 : Experiment electro-mechanical system scheme is shown with relavant communication connections by arrows.

In addition to control of displacement, there should be a feedback mechanism to find the touch point to the surface and make the load controlled indents. However, up-to the state of the system for the experiments had been made, load control had been just used to find touch point. Load measurement has been accomplished via a bar type loadcell and a 24 Bit ADC (HX711). Although employed ADC has superior resolution, its conversion speed is as low as 10 Hz, and load data is transferred through intercessor MCU to PC at 10 Hz rate. Because the main scope is TTC measurement, load data has been a secondary measure for contact but, significant for acquiring reproducible depth dependent TTC with sensitive surface touch find capability.

Moreover, load controlled approach has an other key element due to need for a long distance search of surface. Hence, a step motor was implemented with a high resolution (1/256) driver (TMC2209). In addition, a basic algorithm for approach has been developed to use coarse and fine positioners in harmony. The algorithm provides about 10 μm fine forward movement while controls whether the load threshold is exceeded. Unless the surface was found, actuator is pulled back to initial position and step motor approaches to sample, then actuator is being moved slowly to find surface again. Thus, this actuator and step motor sequential movement cycles enables us to

find the initial contact accurately in a certain error threshold. Furthermore, indent axis (namely Z axis) coarse positioner can be separately used with implemented joystick and UI program for faster applications and, also be employed to make all indentation process without the actuator for high range/low resolution indentations.

In addition to Z axis coarse positioner, XY positioner has been controlled by implementation of DC motor driver IC (L293D) and intercessor MCU. Beyond moving above the surface precisely, XY motor control has enabled us to utilize experiment routine to sequentially indent different desired locations automatically with the help of approach and retract mechanism.

Finally, the last control element of setup is the heater unit. The heater is controlled via a 1 kHz PWM signal provided through intercessor MCU that is supplied to the base leg of power transistor. The transistor's emitter leg is on the ground and, collector is supplied to 12 Volts. A schematic of heater circuit depicted in Figure 2.6. The resistive load is connected to heater unit's 1-2 outputs that can be perceived from the Figure. Without the PWM application these two outputs have 12 Volts and, there is no current occurs through resistance. Henceforth, when the desired duty cycle PWM is applied, for each rise period of voltage on base of transistor provides to GND leg (leg 2 in figure) of heater is set to 0 Volt relative to V_{in} (12 Volts). Thus, an output current on the connected resistive load is obtained.

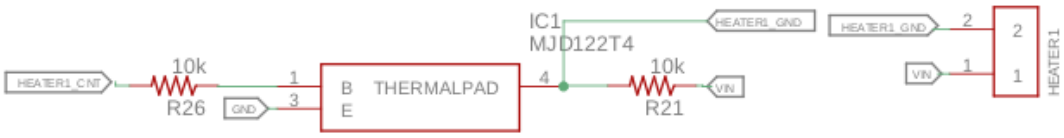

Figure 2.6 : Heater unit circuit schematic is shown.

Even though the intercessor MCU and other ICs are enough to operate the indentation experiments properly, a PC UI has been programmed for the ease of control of system. The UI provides serial communication with intercessor to give packaged orders to be started related algorithms programmed on MCU. Beyond that, it also communicates with the NI-PCIe 6321 card to obtain data of sensors that connected through NI extension card. Moreover, a PID type algorithm is written for continuously control the PWM duty cycle with respect to the sample temperature reading that is made via

the NI DAQ. A summary for overall DAQ system of the setup will be given in the next section.

2.5 Data Acquisition System

The Data Acquisition system (DAQ) consists of National Instruments PCIe 6321 card (NI PCIe 6321 or NI-DAQ), HX711 ADC, analog sensors and digital sensors.

As mentioned earlier, temperature measurements are obtained by thermocouples. For the tip thermocouple, a special (Omega) thin K-type thermocouple of 25 μm has been employed. Moreover, for the sample temperature measurement a 1 mm thick commercial K-type thermocouple has been used. In addition to thermocouples, a digital temperature and humidity sensor (DHT11) is implemented to acquire ambient conditions of setup. The digital sensor directly communicates to MCU with update periods of 2 seconds. However, analog voltage measurements of thermocouples have been read by NI-DAQ with its 16 Bits ADC up to hundreds of kHz.

The thermocouple measurement of temperature depends on Seebeck effect of metals that simply stems from thermo-electric coupling when a temperature gradient is provided. Therefore, making a junction of two dissimilar metal wire and holding the junction and the other end at different temperatures generates a voltage difference between two wires due to their different Seebeck coefficients. Hence, holding the voltage measurement side of the wires at constant known temperature and reading the voltage would provide a relative measure of temperature of junction end.

As can be perceived from the concept of thermocouples, this measurement is vulnerable to errors due to need for constant reference temperature and junction quality. Moreover, due to typically being at the order of 10 mV level of resulting voltages, amplification and analog to digital conversion stages of the thermocouple readings would cause errors and determines the measurement resolution. Employing the 16 Bits NI-DAQ as the temperature reader with 200 mV reference results in 3.05 μV that corresponds to 0.0763 K minimum measurable temperature difference with K type thermocouples (Seebeck coefficient is 39.48 μV/K). Yet, there are mentioned

noises due to the reference junction temperature, DAQ gain, DAQ offset, DAQ uncertainty and random error.

Briefly, reference junction temperature error is the largest one among all. Because, fundamentally the measurement depends the temperature difference between cold junction and thermocouple junction and, noise of the reference directly affects the absolute measurement. On the other hand, reference temperature of the thermocouple wires have been kept at the stable ambient temperature that is almost constant with covers of our setup. Moreover, reflection of absolute measurement error on experiment of periodic contacts is lowered due to averaging, and extracting the time constant due to change of temperature with respect to application of square wave oscillation of position needs a relative change rather than absolute reading.

Furthermore, errors due to DAQ instrument are significant for absolute measurement accuracy too. The most important one is the offset error that stems from the residual offset error, change of the temperature from the last internal calibration and the integral non-linearity (INL) error of ADC. However, as being in the reference junction error, the offset error should not be significant for relative temperature measurements of periodic contacts, due to the fact that it affects absolute accuracy limit.

Additionally, built-in strain gauge of piezo actuator (APA-60S) is amplified and scaled to about 8 Volts by CEDRAT's SG75 card. Then, output of SG75 converted to digital data through a NI-DAQ channel. Due to fiber interferometry calibrations of piezo actuator movement while measuring conditioned built-in strain gauge voltage (SG75 output), the minimum displacement measurable is 3 pm. However, as mentioned for the thermocouple, there are noises limiting this high sensitivity. Furthermore, sometimes a cable junction problem occurs on strain gauge cable to SG75 card connection that mainly shadows all other errors in measurement. For a proper junction a 10 nm of resolution could be obtained while it may increase to 1 μm due to junction problem.

Moreover, DAQ rate should be greater than the measurement frequency and, should be sufficient to extract time constants. Hence, due to low (sub-1 Hz) oscillation application and in the order of 100 ms time constants of micro-contacts allowed us

to use 200 Hz DAQ rate for the measurements acquired through NI-DAQ. Moreover, indentations have been conducted with speeds in the order of 10 nm/s (in general 50 nm/s has been set).

Consequently, two temperature channels and one differential voltage channel (8 Volts scaled strain) have been acquired through NI-DAQ. The NI PCIe-6321 has maximum multi-channel aggregate sampling rate of 250 kS/s with 10 ns timing resolution. Moreover, the timing accuracy is 50 ppm of the selected DAQ rate that is mostly 200 Hz for the experiments so, 25 ns timing accuracy is obtained.

Over and above, multi-channel measurement through NI-DAQ causes a cross-talk between channels. Due to the specification of the NI PCIe-6321, cross-talk of the adjacent channels is given as -75dB and, it is -90dB for non-adjacent channels at 100 kHz rate. Therefore, by connecting strain and temperature channels to non-adjacent channels, we may expect a coupling of 0.032 V/V for 100 kHz (signal frequency). Consequently, we may expect a 65 Kelvin of cross-talk from maximum change of 8 volts through strain measurement for the worst case scenario. However, we observed 3 Kelvin of cross-talk in both temperature channels simultaneously, which corresponds to about -156 dB cross-talk for 200 Hz DAQ rate and 9 mV/s strain gauge voltage change as can be seen in Figure 2.7. We are ensured that the observed cross-talk is due to the measurement of the strain gauge, but it is not related to high voltage change/coupling on the piezo by repeating the experiment with unplugging the strain voltage measurement on the NI-DAQ.

Furthermore, as soon as the voltage change is small such as half volt of strain, about 0.2 Kelvin cross-talk occurs which is not resolvable. Thus, corresponding to about 5 μm displacement of the actuator, 500 mV of strain change and below would cause non-sensible cross-talk at the temperature data. Even so, abrupt changes and high strain applications can be post-processed properly to get rid of cross-talk effects. However, it would not matter for the sake of analysis of temperature measurement through square wave type strain changes by exponential fitting the temperature difference of one position separately. Because, the tip is held at the almost same position during

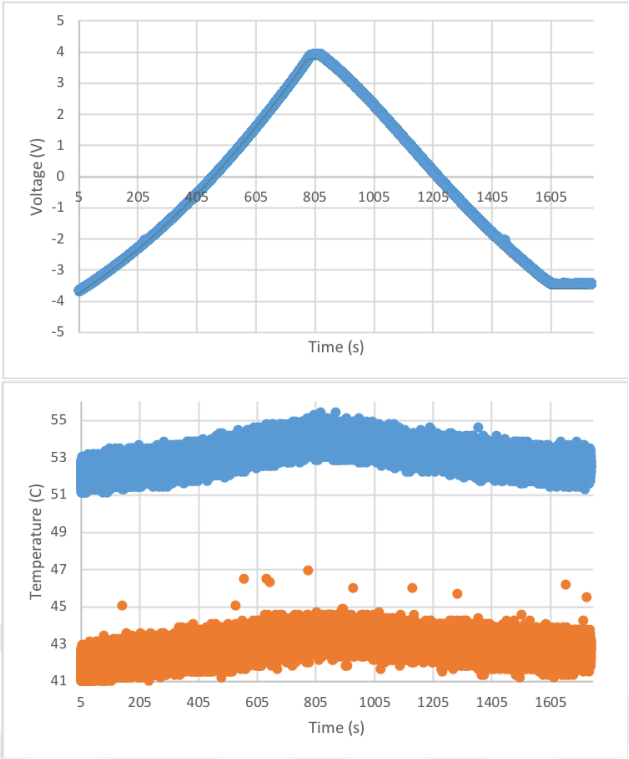

Figure 2.7 : Cross-talk in temperature channels (bottom graph: blue is sample, and orange is tip temperatures) is caused by strain gauge voltage change (top) due to full-scale piezo actuator movement.

each separate exponential fitting, so even there is an observable cross-talk, it would just affect the absolute measurement not the difference to be fitted.

Consequently, acquired NI-DAQ data has been written as TDMS files which is set to be in groups for steps of experiment such as approach, indent, oscillation etc. TDMS files hold zipped data with proper time stamping, so it provides an efficient storage and post-processing with easy control by written UI and data process programs.

In addition, load has been measured through strain of lever type loadcell that is acquired by 24 Bits ADC (HX711 IC). The employed loadcell is half bridge and absolute measurement is significantly affected from change of temperature. Hence, because of the heater is located on the loadcell, temperature has been awaited to reach a steady condition prior to experiments. Besides, 5 mN of noise limit has been observed while the minimum measurable load interval is 46.5 μN (23.25 μN resolution).

Although utilizing the HX711 IC satisfies the load resolution requirements with 24 Bits, its 10 Hz DAQ rate is a significant issue. Because, the low rate causes both

the limitation to compliance to Nyquist criterion and integrity of DAQ system to assess the results of NI-DAQ and HX711 together. Nevertheless, the actuator control is also made with at least 100 ms steps due to communication requirements, so setting the control steps to 200 ms would ensure us to provide Nyquist criterion. Furthermore, for the scope of the thesis, load data is a subsidiary measurement to interpret contact measurements and, it can be post-processed to demonstrate load-displacement/temperature type data representations [78]. Sure, it may be improved to acquire load data through NI-DAQ or an other fast ADC but, for the sake of our technical and economic capacity HX711 seems adequate.

Finally, there are miscellaneous digital sensors that are connected to MCU such as XY positioner encoders, end-stops for coarse positioners, proximity sensor for indent direction coarse positioner and accelerometers. Except of accelerometers, these sensors are auxiliary elements for coarse positioning. Accelerometers are implemented to be assured of orthogonality of indenter, sample holder and step motor bases by measuring 3 axis accelaration. Because the accelerometers should measure 1G at the indent axis while all are the stable and in balance, the deviation from that would indicate the obliqueness and its direction. However, after the first setup, due to complex-crowded cabling of I2C communicated accelerometers, they are subtracted from the setup. Lastly, there is a microscope camera for the ease of positioning and determining the indentation area on sample.

2.6 Calibrations of Experimental Setup

2.6.1 Piezo actuator displacement calibrations

Firstly, actuator movement was measured under an optical microscope by carefully adjusting the focus while changing the piezo voltage. Hence, recording optical microscope focus positions and corresponding piezo voltages provided hysteresis loop and piezo constant roughly. Moreover, strain gauge measurement was recorded to calibrate measurement of strain gauge to actual piezo voltage. Results show (in Figures 2.12, 2.9), 85 μm total displacement for 170 Volts of voltage change while hysteresis holds for both strain gage and optical measurement of displacement.

Furthermore, by attaching a fiber on the actuator (see Figure 2.8), small and full range behavior of actuator had been examined using the fiber interferometry technique. Fiber interferometry technique, which we have used for many other small displacement measurements, has been conducted with help of NanoMagnetics Inc Fiber Interferometry card. The attached fiber is connected to the Interferometry Card that enables to couple 1330 nm laser light into fiber. The other end of the fiber was aligned on a mirror that is on the XY stage. Hence, we could obtain an interference of light reflected from the mirror and the fiber end.

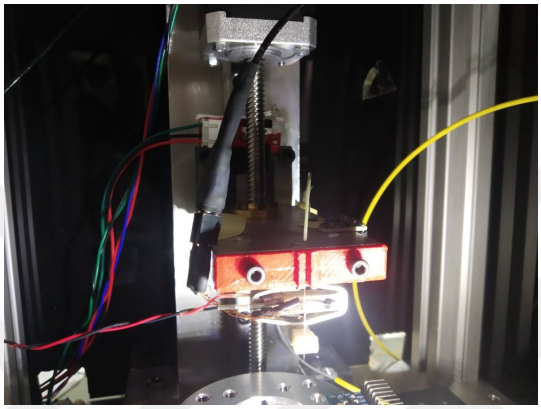

Figure 2.8 : Fiber was attached to piezo and aligned on a mirror for fiber interferometry.

This interference created by mirror-fiber end Fabry-Perot ethalon is read by Interferometry card's photo diode. The signal from photo diode is appropriately amplified to output of the card to be acquired by user. Therefore, moving the actuator with slow steps creates a resolvable periodic pattern of interference with half wavelength (655 nm) intervals. Moreover, with a proper (post) process of obtained interference patterns, the calibrations would be made more sensitive than counting the full periods (655 nm) (full scale and small range displacement calibrations are shown in Figure 2.14).

Actuator has been driven through a high voltage amplifier (CEDRAT LA75) as mentioned. The open/close loop characteristics of piezo drive are studied, and some optimal parameters are found for the setup after several PID parameters were tried. Below Figure 2.10 shows open loop and close loop movement graphs of the actuator. Here, for the control of the applied voltage 600 mV steps were applied at 10 Hz while built-in strain gauge voltage was being recorded. Close loop parameters has been used

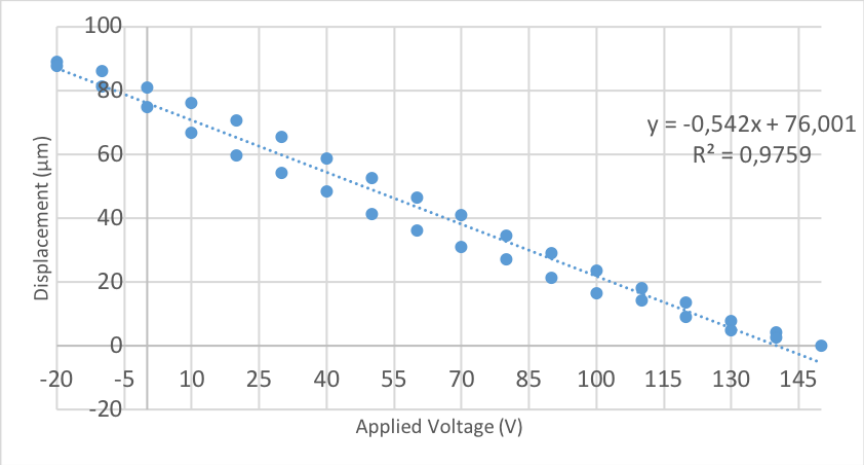

Figure 2.9 : Hysteresis Loop of Piezo Actuator Obtained from Optic Microscope Focus Adjustment.

at 80% proportional gain, 1.25% integral gain, and 100% differential gain with 50 Hz low pass filter applied on the strain feedback.

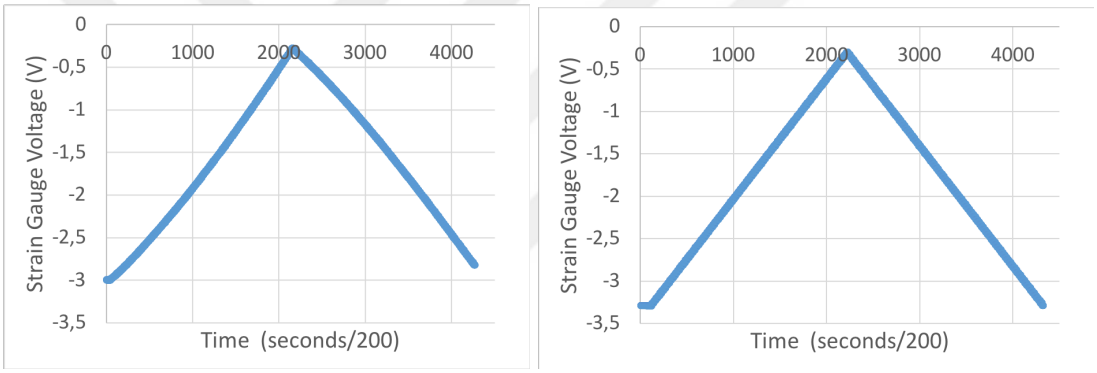

Figure 2.10 : Approximately 30 μm forward and backward movement of actuator by 100 step 600 mV per 100 ms drive with (left) Open Loop and (right) Close Loop.

Besides of continuous push and pull, 60 seconds of hold sequence between push and pull was tried to demonstrate creep effects [Figure 2.11]. Note that, with the help of zoom-in, effect of discrete driving can be seen as discreteness on the strain gauge voltage.

Lastly, due to the high voltage amplifier's (LA75) current limit of 90 mA to avoid short circuit and other shock incidents, the given voltage change should be limited to be applied in a certain time lapse that can be given as:

$$I_{limit} = \frac{dQ}{dt} = \frac{d(CV)}{dt} = C\frac{dV}{dt} = 90mA \tag{2.3}$$

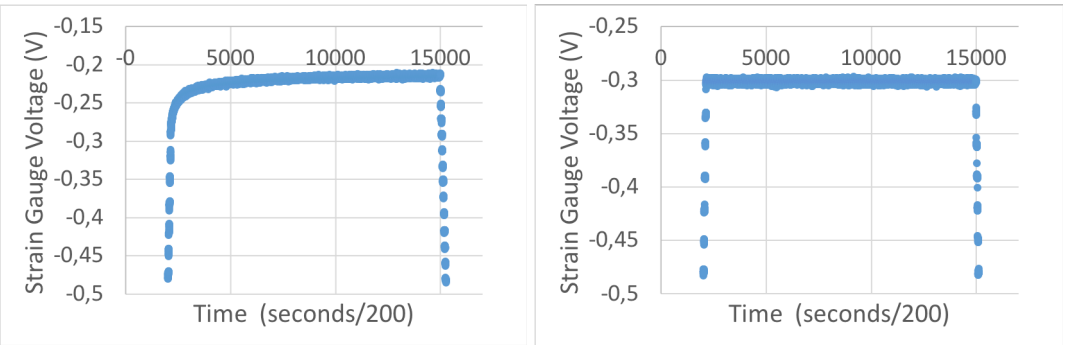

Figure 2.11 : 60 seconds of hold period was waited between 30 μm forward and backward movement of actuator by 100 step (600 mV per 100 ms) drive with; (left) Open Loop and (right) Close Loop, graphs show the zoom-in to hold voltage.

thus, to comply with the current limit (I_{limit}) of 90 mA, with 1.5 μF capacitance (C) of APA60S, we can estimate the time lapse Δt of a finite voltage change ΔV should be:

$$\Delta t(\mu s) = 17 \cdot \Delta V \tag{2.4}$$

Consequently, incident full range change of voltage of 170 Volts should take 2.89 ms to be applied on actuator. For the square wave applications of this study, we are using generally below 20 volts of change (corresponding to 10 μm peak to peak change) that takes 340 μs. Therefore, the time lapse for the square waves does not affect the time constant evaluations that are in the order of 100 ms.

2.6.2 Coarse positioners calibrations

The Z stage linear rail-trapezoidal screw system has been driven through Nema17 step motor with help of a high resolution IC (TMC2209) as mentioned at Section 2.2. Because, the system was constructed homemade, it is optimized by error-trial method to make firm and linear. Afterwards, Fiber Interferometry was conducted to obtain displacement resolution and a sense of linearity. Moreover, full range travel of Z axis was measured by a 1 mm precise ruler.

On the other hand, the XY stage had been also tried to be calibrated by Fiber Interferometry but, it was found hard to capture proper patterns due to relatively higher continuous speed and higher minimum step size (though it is not step-wise drive motor). However, while using the indenter executing sequential indents on the samples has provided a self-calibration with encoder counter feedback (see Figure 2.13).

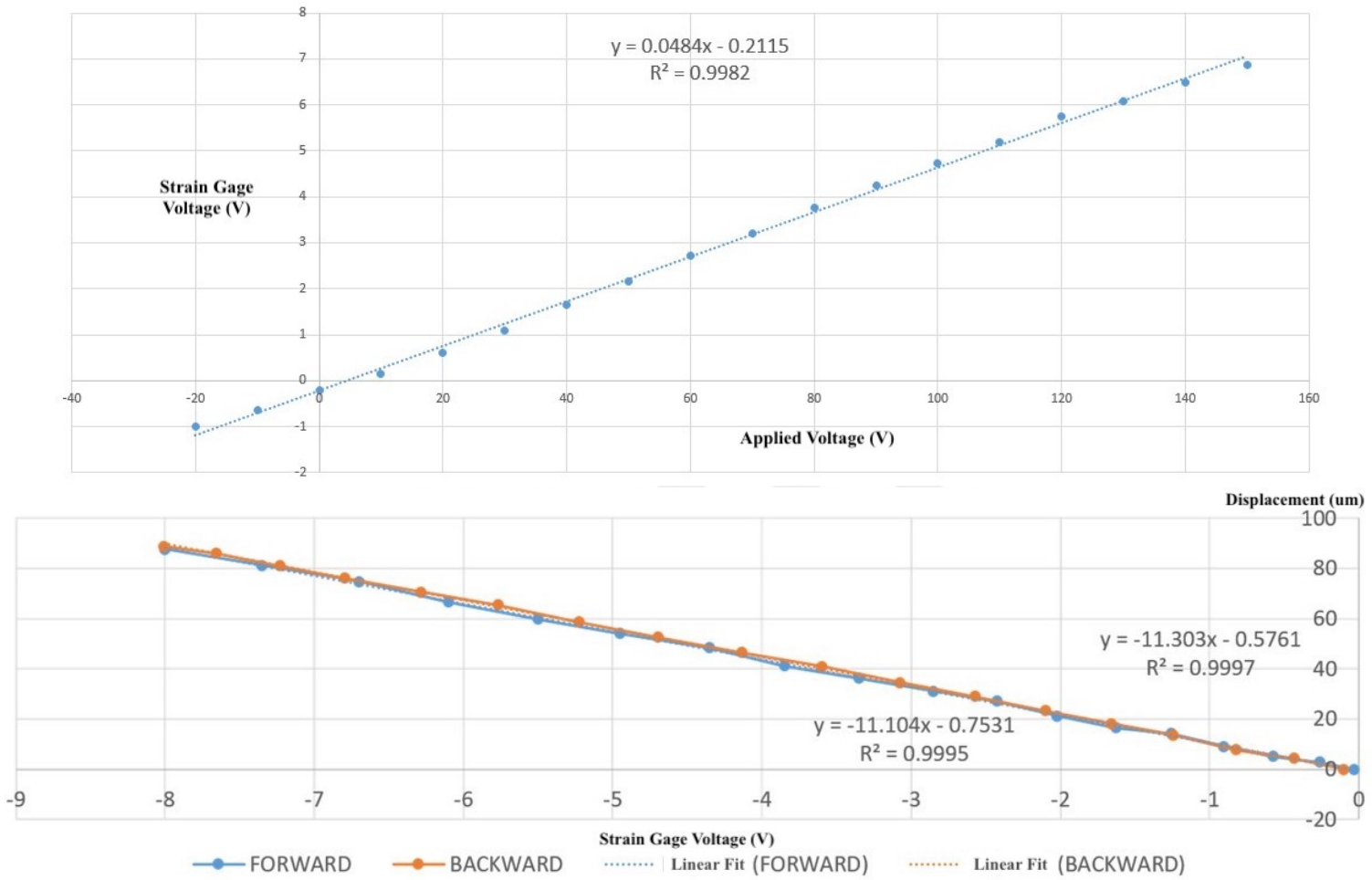

Figure 2.12 : Strain Gauge Voltage versus Applied Piezo Voltage (top), Measured Distance from Optical Microscope Focus versus Strain Gauge Measurement (bottom).

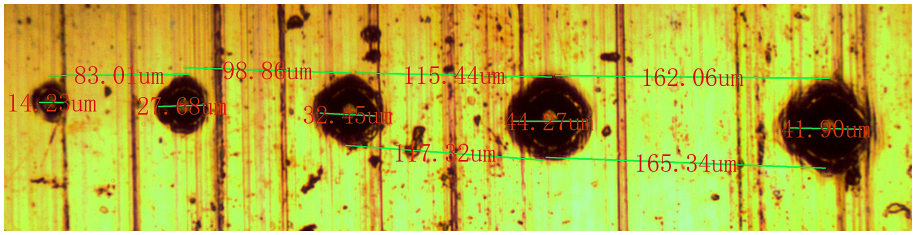

Figure 2.13 : Sequential varying depth indentations on the gold sample were made by auto approach routine and XY positioning. XY stage encoder was calibrated with these optical microscope data.

2.6.3 Loadcell mass and deflection calibrations

Loadcell's mass measurement was calibrated by a proof mass and pre-calibrated 10 mg sensitive scale. In addition, the lever type loadcell's deflection with respect applied force (the force constant) had been measured by a special designed setup of the fiber interferometry and hollow water bottle hung on loadcell. Therefore, the tiny hole of bottle leaks the added water continuously while interference pattern was being counted and, the load was being measured.

After many careful experiments, an average of 536.5 $mN/\mu m$ was determined for stiffness of loadcell. In Figure 2.15, an example of the loadcell stiffness measurement by water flow (about 400 g of water) is given. Note that, this calibration is made for both force and stiffness, so the top graph of Figure 2.15 shows bits (in 24 Bits scale) rather than the load yet.

2.6.4 Indentation calibrations

Providing reliable load and depth data through an indenter depends on the measurement uncertainties in DAQ system, touch point uncertainty and the frame compliance.

If the amount of indent depth into sample would like to be extracted from a total movement, firstly the touch point should be determined from the increase of the load. Hence, the uncertainty of the load measurement sets the minimum for determining the touch point. Estimating a low load uncertainty may allow to use spherical elastic depth to load relation [eq. 1.43] which assumes depth exponent of 1.5 and dependency to indented material and tip radius. Moreover, the indentation data can

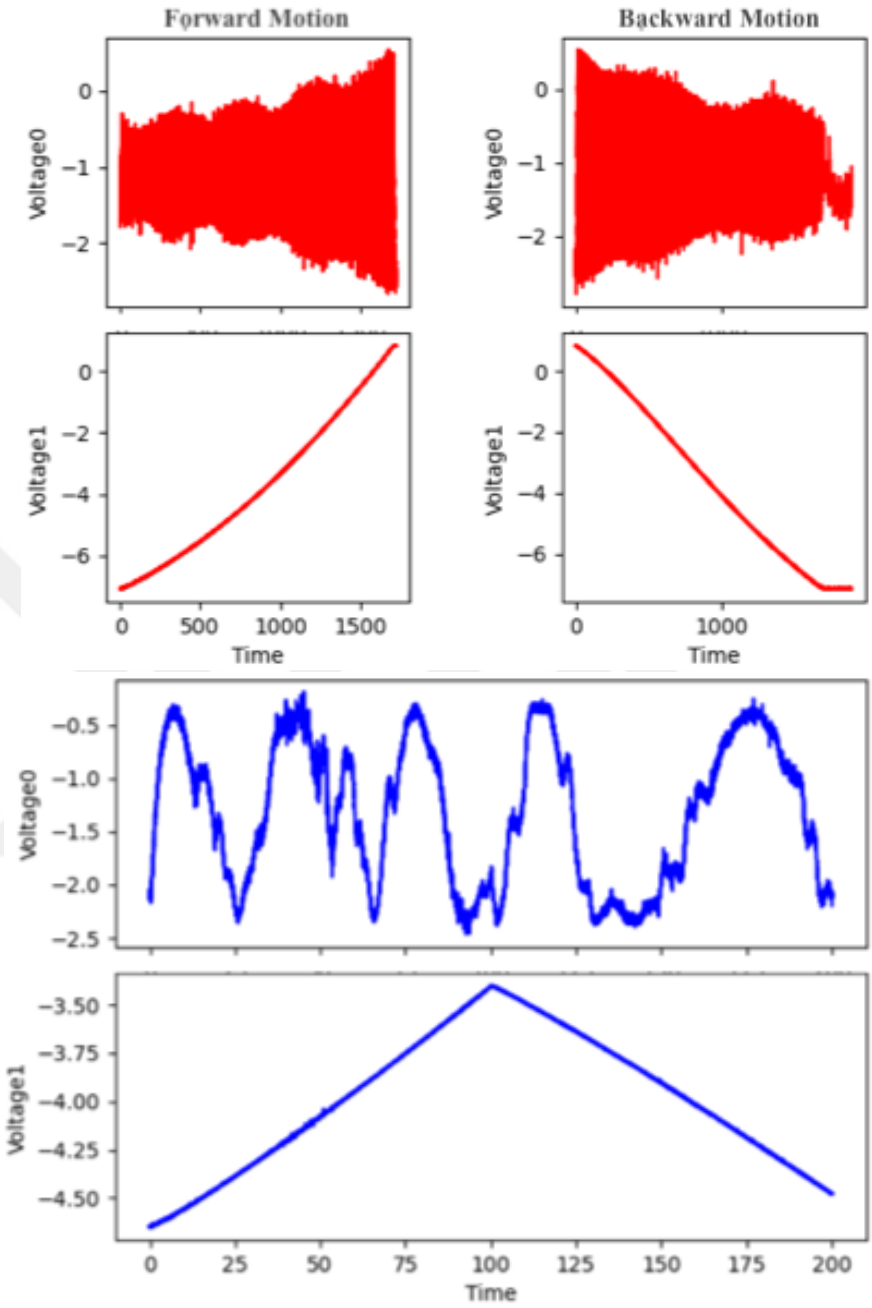

Figure 2.14 : Actuator movement calibration with fiber interferometry; top: Full range push (left) and pull (right) of actuator sequentially: upside Photo Diode Voltage of Interference (Voltage0) and bottom: Strain Gauge Voltage of Actuator (Voltage1), bottom: A small range push and pull of actuator sequentially: upside Photo Diode Voltage of Interference (Voltage0) and bottom: Strain Gauge Voltage of Actuator (Voltage1).

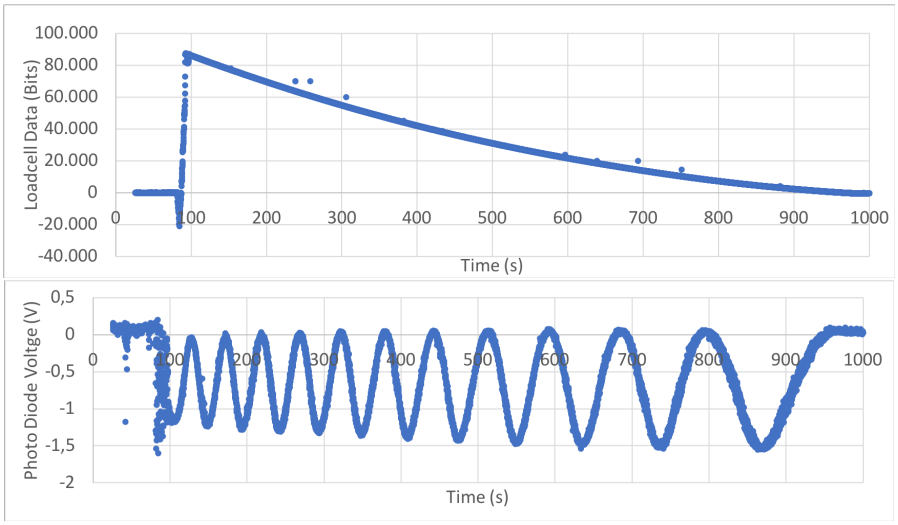

Figure 2.15 : Loadcell stiffness calibration by water flow, (top) measurement of loadcell while water was leaking through hollow bottle, (bottom) Fiber Interferometry measurement while water was flowing.

be post-processed and several standard methods can be applied to find touch point, but above presumptions were made for indicating the dependency of the touch point uncertainty to tip and sample properties as well as the DAQ system uncertainties. In Figure 2.16, an example approach and a typical touch point sensitivity demonstration can be seen.

Relaxation effect on the load takes place for the indentations due to displacement controlled indents after finding the touch point with load threshold. Figure 2.17 shows indentation and hold sequences for depth and relaxation can be seen on the load graph.

The frame compliance is the inverse of equivalent total spring constant of the system. The stiffness calculations 1.47 for an ideal indenter was given at the Introduction 1.3. If we were to assume that all indenter system as connected in series through the contact [3,37]:

$$S_{measured} = \left[\frac{1}{S_{contact}} + C_f\right]^{-1} \tag{2.5}$$

Thus, employing the Oliver-Pharr or Doerner-Nix methods to retraction data, one can find an equivalent stiffness $S_{measured}$ value of contact stiffness $S_{contact}$ and frame compliance C_f.

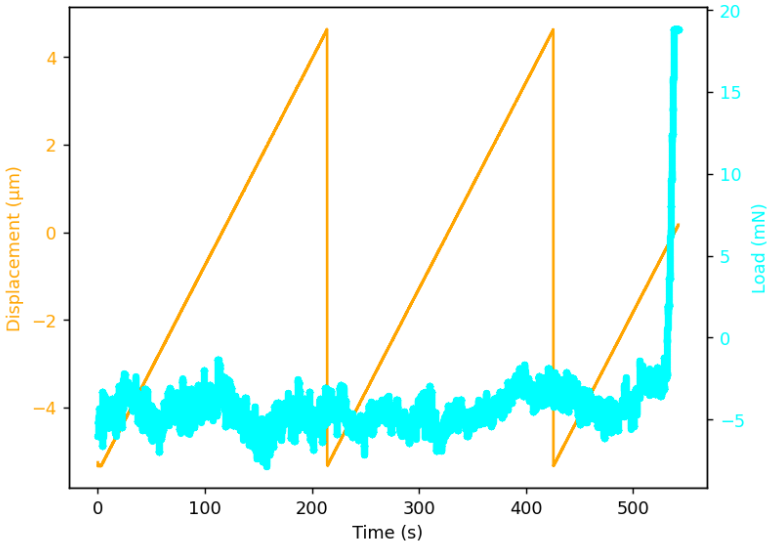

Figure 2.16 : Load (blue) and Displacement (orange) versus time, approach to fused silica surface with mentioned step motor-actuator mechanism up to set point with 50 nm/s speed, step motor movement is not shown here but after each pull back it was driven forward about 6 μm. Relative position zero point set for position of the load set point (20 mN for this example).

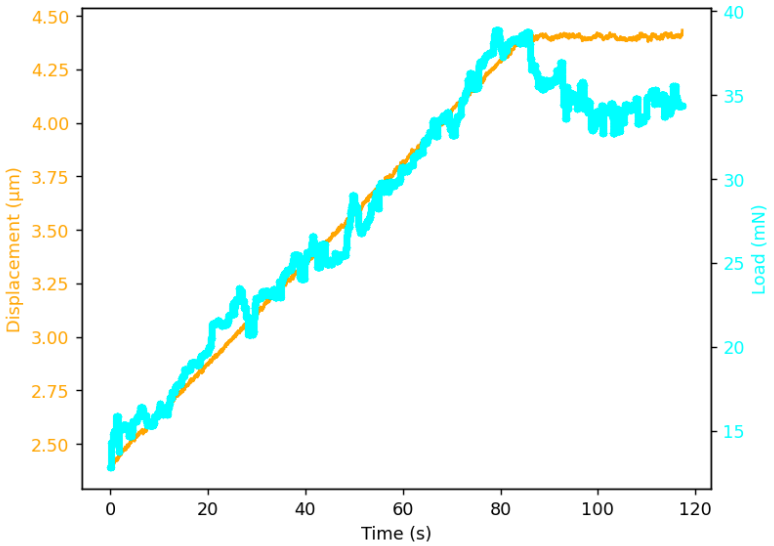

Figure 2.17 : Relaxation effect on the load (blue) is shown while indentation position (orange) was kept constant. Tip is truncated (1.5 μm side length of flat triangle) Berkovich and sample is gold foil (400 μm thickness).

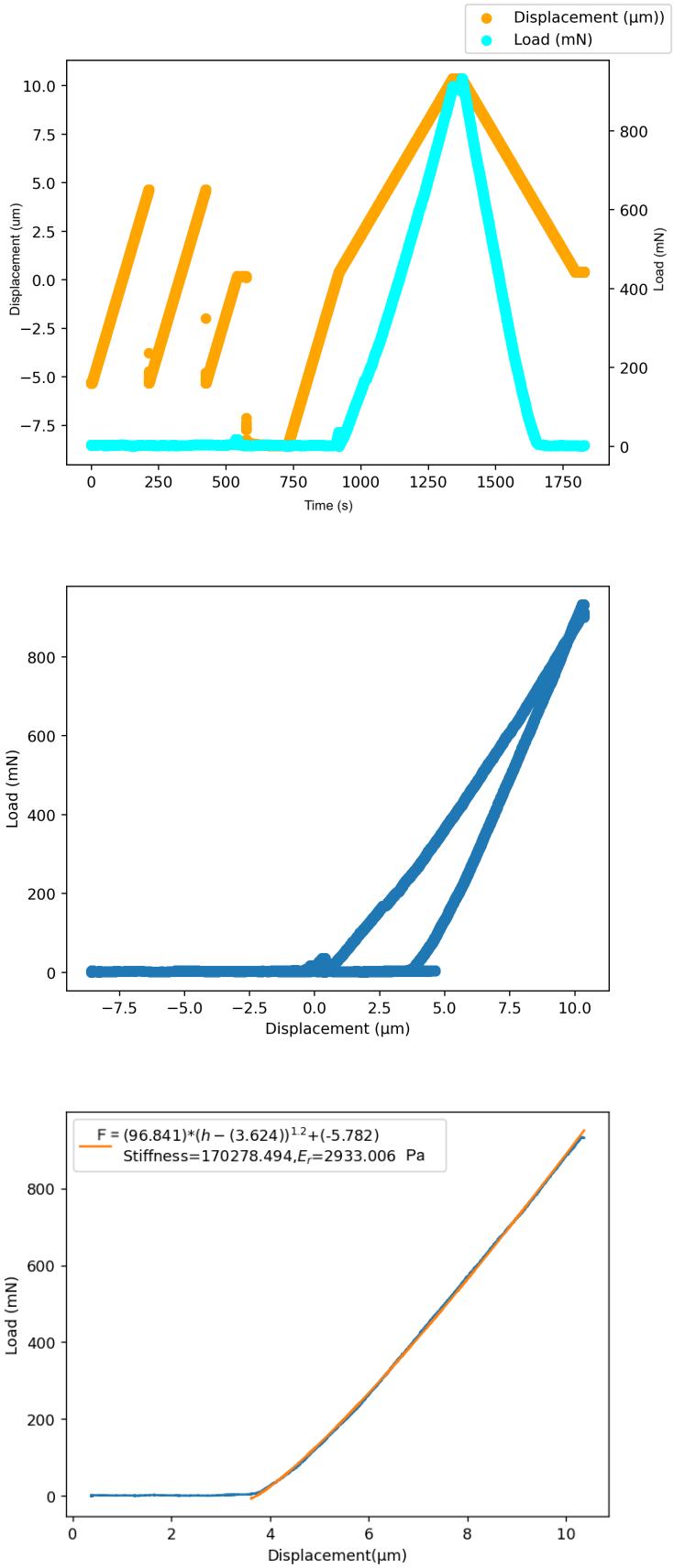

Figure 2.18 : Time resolved load and displacement data of Fused Silica Indentation with truncated Berkovich tip (top), load-displacement curve (middle), and corresponding Oliver-Pharr Analysis on the retraction curve (bottom).

To find contact stiffness accurately, frame compliance should be measured with a known calibration sample. Therefore, we have conducted several experiments on the fused silica, copper and gold to estimate the frame compliance of the indenter setup (see Figures 2.18, 2.19).

Consequently, the depth measurement of the experiments can be denoted as:

$$d = V_{st} c_{cal} - F_{lc} C_f - d_t \tag{2.6}$$

where V_{st} is the strain gauge voltage measurement that is converted to displacement by calibration factor c_{cal} ($\mu m/V$) after the touch point d_t is reached, a subtraction from the total displacement of the actuator should be made for the movement of the frame by compliance C_f times the loadcell measurement F_{lc}.

As mentioned earlier, the touch point uncertainty depends on the indenter shape, sample properties and load uncertainty. However, for the setup, tips and metallic surfaces that had been used, we estimate a flat punch approximation with order of 10 μm radius and metallic surface of 100 GPa modulus:

$$\Delta d_t = \frac{\Delta F}{2aE} = \frac{2.5mN}{2 \cdot 10^{-5} \cdot 10^{11}} \approx 1nm \tag{2.7}$$

However, with the knowledge of the compliance, we could estimate an reduced modulus roughly 5 GPa that makes the uncertainty in touch point 50 nm. Consequently, we can estimate the error in depth equation 2.6 with standard deviation formula:

$$\Delta d = \left[\left(\frac{\partial d}{\partial V_{sg}} \right)^2 \Delta V_{sg}^2 + \left(\frac{\partial d}{\partial c_{cal}} \right)^2 \Delta c_{cal}^2 + \left(\frac{\partial d}{\partial F_{lc}} \right)^2 \Delta F_{lc}^2 + \left(\frac{\partial d}{\partial C_{fr}} \right)^2 \Delta C_{fr}^2 + \left(\frac{\partial d}{\partial d_t} \right)^2 \Delta d_t^2 \right]^{\frac{1}{2}} \tag{2.8}$$

$$\Delta d = \sqrt{c_{cal}^2 \Delta V^2 + V_{fs}^2 \Delta c_{cal}^2 + F_{lc}^2 \Delta C_f^2 + C_f^2 \Delta F_{lc}^2 + \Delta d_t^2} = 0.12 \mu m \tag{2.9}$$

where c_{cal} is calibration constant of the strain gauge voltage to real position, Δc_{cal} is the uncertainty in the calibration, ΔV is the uncertainty in the strain gauge voltage measurement (output from the SG75 card), V_{fs} full scale differential output of the strain gauge voltage output (V_{st}), F_{fs} maximum loading for the experiments measured

by loadcell (F_{lc}), ΔF_{lc} is the uncertainty in the load measurement through loadcell, C_f is the frame compliance, ΔC_f is the uncertainty in the frame compliance calculation and Δd_t is the touch point uncertainty.

Table 2.2 : Parameters of the depth error at 23°C is given.

Parameter	Value
c_{cal}	10.00 μm/V
Δc_{cal}	10 nm
ΔV	5 mV
V_{fs}	8 V
F_{fs}	5 N
ΔF_{lc}	2.5 mN
C_f	5.95 μm/N
ΔC_f	9.7 nm/N
Δd_t	50 nm

Lastly, because of making the experiments at the temperatures higher than the room temperature, we conducted some experiments to reveal effects of temperature on the compliance and absolute load measurements. Consequently, there is a proportional increase observed in the compliance with temperature increase at the sample while the absolute load calibration measurements stand still. However, care should be taken for getting the system to steady state conditions, because the offset of the load measurements drifts with the varying temperatures. 8 mN/K loadcell offset drift has been measured while the 100 g calibration mass has been repeatedly measured between 22°C to 50°C with an average of 986.4 mN and median of 987 mN. All load measurements between the mentioned temperature interval with the calibration mass are obtained between 985 mN to 988 mN which is inside the bounds of the load error $\pm$2.5 mN. The accuracy of the load measurements can be estimated by using 9.81 m/s^2 gravitational acceleration that shows an %0.5 error. We will tune the load calibration constant (of HX711 ADC data) from 46.5 $\mu N/bits$ to 46.245 $\mu N/bits$ by using these measurements to correct the systematic error.

On the other hand, compliance measurements revealed that a 0.63 $\frac{\mu m}{NK}$ increase from the room temperature compliance of 5.95 $\mu m/N$. Therefore, data analysis will be carried out by considering temperature coefficient, and depth value will be found with

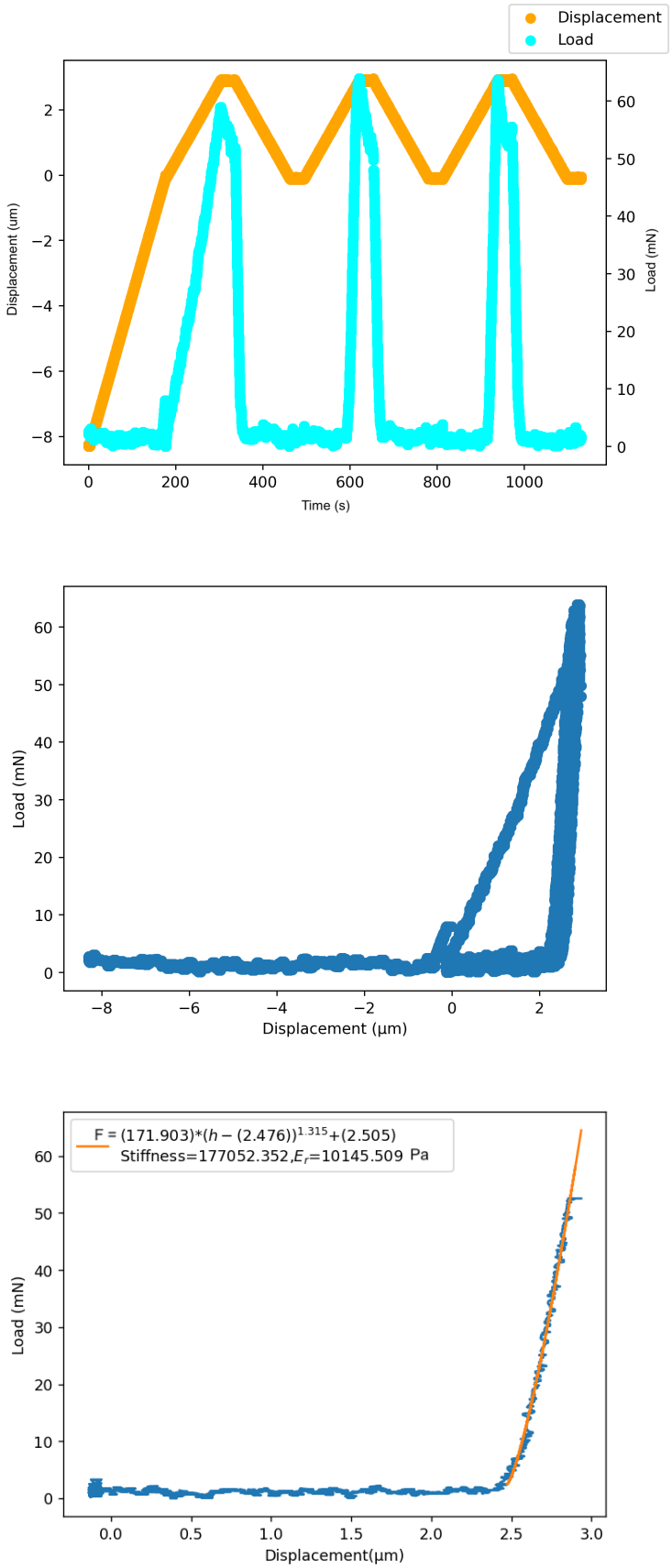

Figure 2.19 : Load and Displacement curves for 2 μm Copper indentations with Truncated Berkovich Tip: time resolved demonstration (top), load versus displacement (middle) and Oliver-Pharr analysis trial (bottom).

Table 2.3 : Measurement (DAQ) system parameters are given.

Measurement (unit)	DAQ Rate (Hz)	Resolution	Noise Floor	Uncertainty
Load (mN)	10	0.465	5	2.5
Depth (nm)	200	0.003	10	120
Temperature (K)	200	0.076	1.5	0.75

the equation:

$$d = V_{st}c_{cal} - F_{lc}(C_f + 0.63\Delta T) - d_t \tag{2.10}$$

Here the ΔT is the difference between the calibration temperature (23°C) and the experiment temperature. Moreover, due to finding the touch point with the load, touch point uncertainty will be increased by a temperature multiplication factor of 3.1 nm/K.

However, re-calibration of the depth with optical microscope and AFM shows there is not a major effect of compliance and temperature of the indenter on the depth of indentation of metal samples. Therefore, we have used the depth data without the compliance correction, but with the loadcell stiffness correction only. It seems, we should develop more the setup for the accurate indentation analysis, and we have left these works for another study.

2.7 Experimental Procedures

The thermal contact conductance investigation while changing the contact itself needs revealing methods. In our experimental procedures, firstly a cold diamond indenter tip is taken into contact slowly (about 50 nm/s) with metal surface mostly at about 100 mN load. After establishing the contact, sub-1 Hz square oscillation of position -mostly with amplitude of half of step's indentation depth- has been applied to the tip for almost 100 cycles of swinging around the contact.

An illustration of the four main protocols can be seen in Figure 2.21 and control flow of the experiments is illustrated in Figure 2.20.

2.7.1 Sequential indentations at single location

This type of procedure has been the main method that we developed for the TCC investigations with respect to the contact depth. As mentioned above, firstly the touch

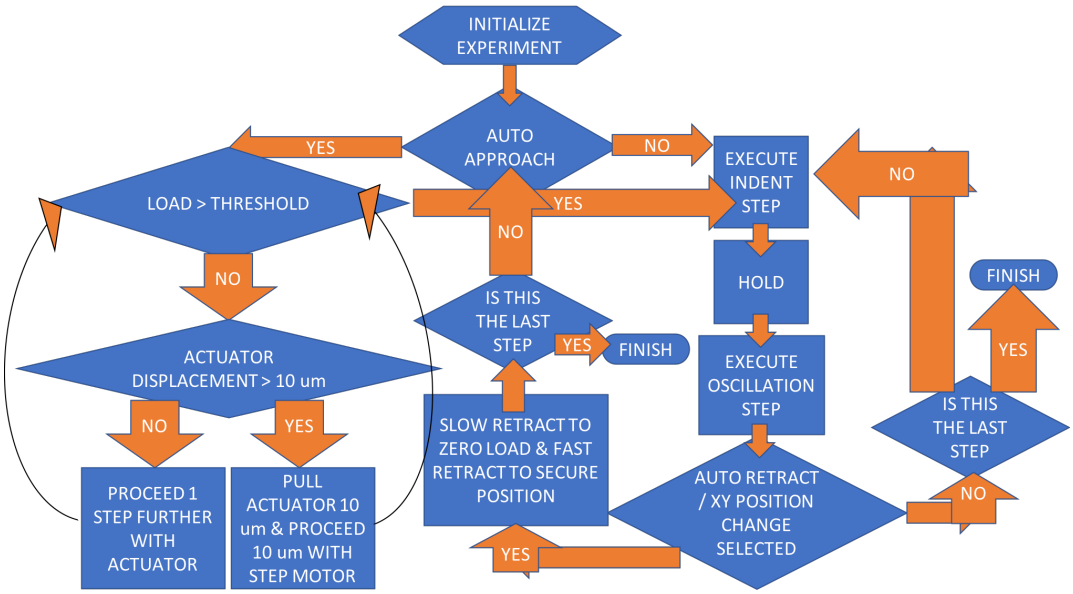

Figure 2.20 : Control Flow of Experiments (10 μm of approach cycle is given as example).

point of tip and sample is found for a certain load threshold level while the tip is held at narrow (below 1 mm) to the hotter sample before beginning to approach. Then, first oscillation sequence is applied after awaiting to reach a steady level of load and temperature at the touch point. After that, a certain predetermined indentation is realized to push further the tip inside sample. Following to that fresh indentation, the same amplitude, frequency and duration of oscillations are conducted at that position. Further, depending on the planned experiment, indent-oscillation cycles are continued respectively to extract thermal time constant of the contact at several levels of depth. At last, the tip is retracted slowly to initial position.

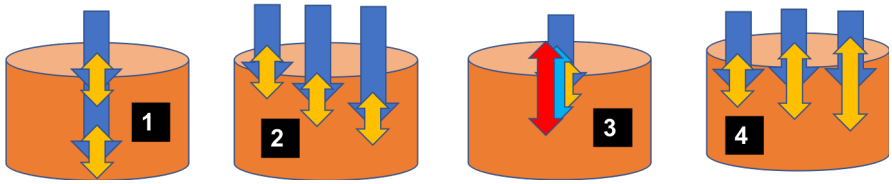

Figure 2.21 : Employed experimental procedures: (1) Sequential indentation steps at same position with same amplitude oscillations in between, (2) Sequential indentations at different locations with same amplitude oscillations in between, (3) Sequential increasing amplitude oscillation application steps at same position, (4) Sequential increasing amplitude oscillation application steps at different locations.

In Figure 2.22 (left) averaged oscillation data for each step is shown for the intervals between single location sequential indentations of this procedure. Contact and

separation sequences of the oscillations demonstrate clear exponential rise and decay while square wave application can be seen by the load and depth averages. After the averaging, each depth of contact and separation is fitted to lumped model of transient heat transfer, so we could obtain the right graph of Figure 2.22 that shows load and depth dependency of time constants due to many oscillations at each depth of the experiment.

Cross-talk can be seen due to averaging also the sample temperature along the cycles, so it becomes visible. The behavior is explained in the 2.5, and square wave application results in square wave type cross-talk while for each indentation level it follows the strain with a proportional cross-talk. Overall effect of the strain-temperature cross talk can be roughly estimated for 12 μm displacement as 0.6 K. However, for the time constant extraction we rely on the each stable strain state for contacts and separations, so cross-talk does not affect the fits of tip temperature and extracted time constants.

2.7.2 Sequential indentations at different locations

As can be gathered from the title, it is the same procedure with the difference of locations of each indent-oscillation sequence of various depths. Therefore, we would interpret the difference of -if any- freshly indented and pre-stressed contact's thermal behavior. Moreover, to anticipate the true contact depth dependency, this technique needs a proper approach, retract and sample-movement mechanism while keeping the touch points at the same level with a certain error. In Figure 2.23 an experiment result is provided to clearly demonstrate the sequential indentation procedure.

To emphasize the sequential indent procedures and show the difference between them, temperature, load and displacement of the indent sequences also are provided in Figure 2.24.

The single location procedure is shown at the top graphs of Figure 2.24 that show a relatively longer first step due to approach to surface then consecutive steps with equal size indents and holds followed. The temperature of the tip (right graph at top in Figure 2.24) shows a long RC behavior while going deeper into sample with indents, but slight

decays can be seen in the beginning of each step due to oscillations in between them caused to plastic deformation further from the last indentation step.

On the bottom graphs of the Figure 2.24, an example of different location sequential indentation procedure's indentation sequences are shown by depth, load and temperature versus time. For this procedure, after oscillations followed by each indentation and hold sequence at one location, tip is withdrawn to initial secure position, and XY stage moves the sample to predetermined position of the consecutive step. Therefore, displacement graph shows indentation and relatively long secure pull-back sequences while load measurement complies with that. Note that, for small indentation depths, there is not any remaining contact at the average position of the oscillations (last indentation position), so that we do not see any load decrease while pulling back the tip. However, for relatively deeper indentations, there is still contact remains due to elastic recovery, so that we can see decreasing load while pulling back the tip at the Step 4 and Step 5. In addition, due to pull back and making deeper indentations, temperature of the tip shows heating up and cooling down RC behavior along with each sequential steps (bottom right of Figure 2.24).

2.7.3 Sequential oscillation amplitudes at single location

In this type of procedure, after touch point is reached and indentation to keep the contact for oscillations is made, small oscillation amplitude to larger amplitudes are applied to the tip for a certain duration (90 cycles generally) for each predetermined amplitude levels. Therefore, it is similar to indent steps of aforementioned sequential indentation procedure due to the fact that increasing the amplitude of the oscillation sequentially with application of many cycles for each level provides sequential increase in contact depth between steps.

Sweeping the amplitudes has a similar effect as making the same amplitude oscillations at different indentations, but, for the aforementioned sequential indent-oscillation procedures, after a certain level of indentation, increasing the amplitude of position oscillation provides increasing temperature difference between contact and non-contact states. Thus, the problem of tip cannot be cooled at non-contact periods

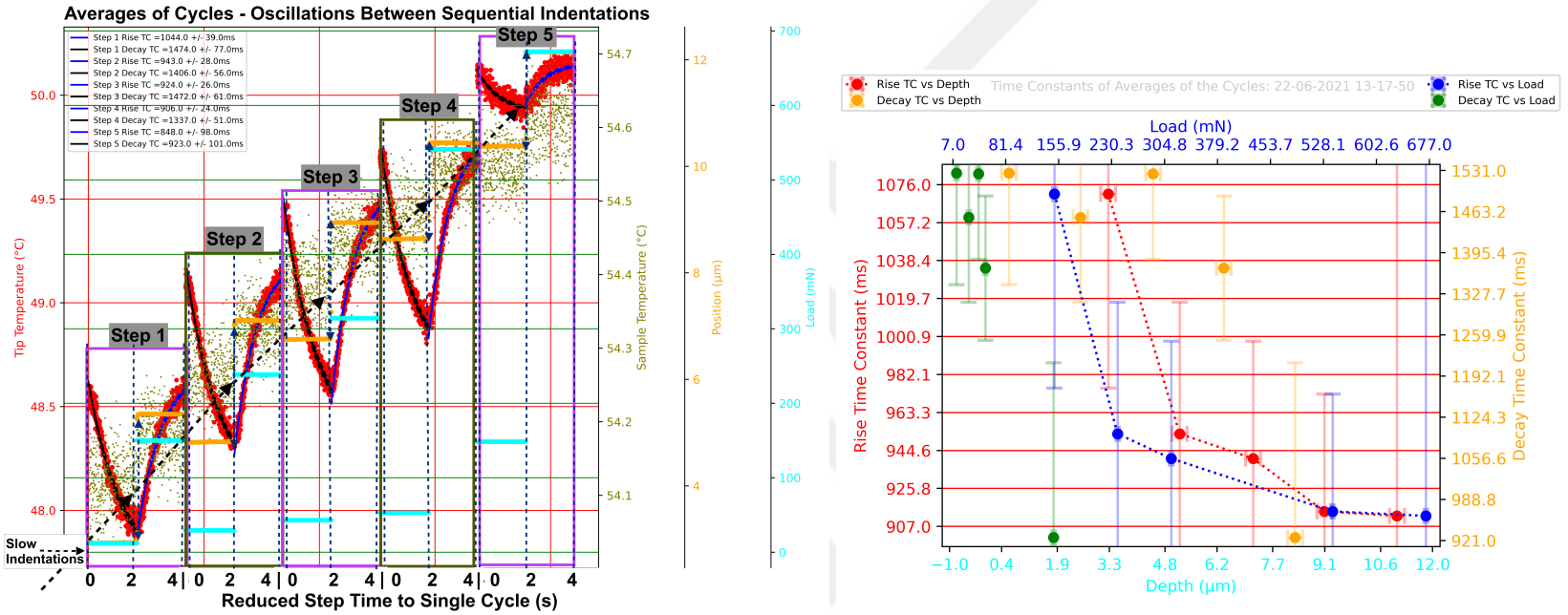

Figure 2.22 : (Left) Averaged cycles of tip (red), sample (green) temperatures, depth (orange) and load (blue) data of a sequential indentation experiment with oscillations at each indent level. Arrows are put to show prior indentations to the mid-point of the oscillations. Note that for this procedure, the effect of being not able to cool is seen at the last step due to elastic recovery sustains some residual contact at separation sequence. (Right) Time constants (TC) obtained from the rise and decay temperature data at each step, contact time constants show high depth and load dependency.

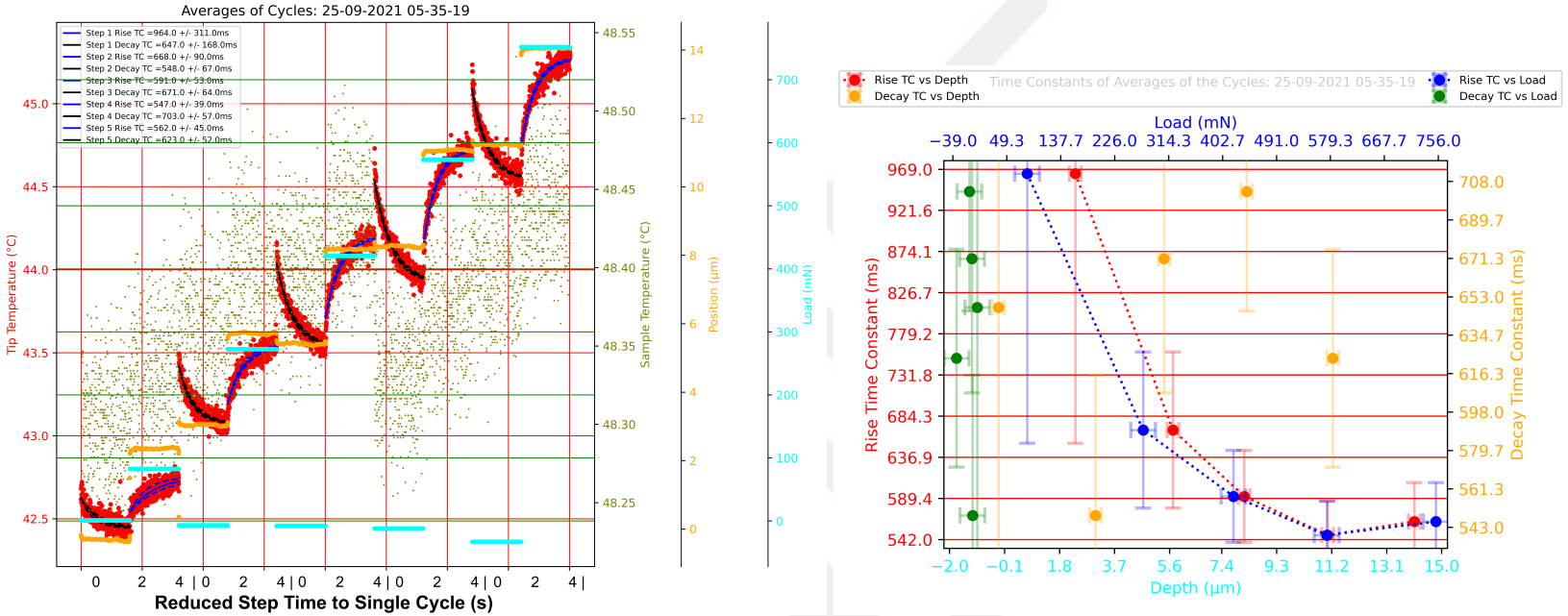

Figure 2.23 : (Left) Averaged cycles of tip (red), sample (green) temperatures, depth (orange) and load (blue) data of a sequential different location indentation experiment with oscillations at each indent level. (Right) Time constants (TC) obtained from the rise and decay temperature data at each step, contact time constants show high depth and load dependency. Note that, insufficient heating up at the contact sequence of first step caused to high error for fitting.

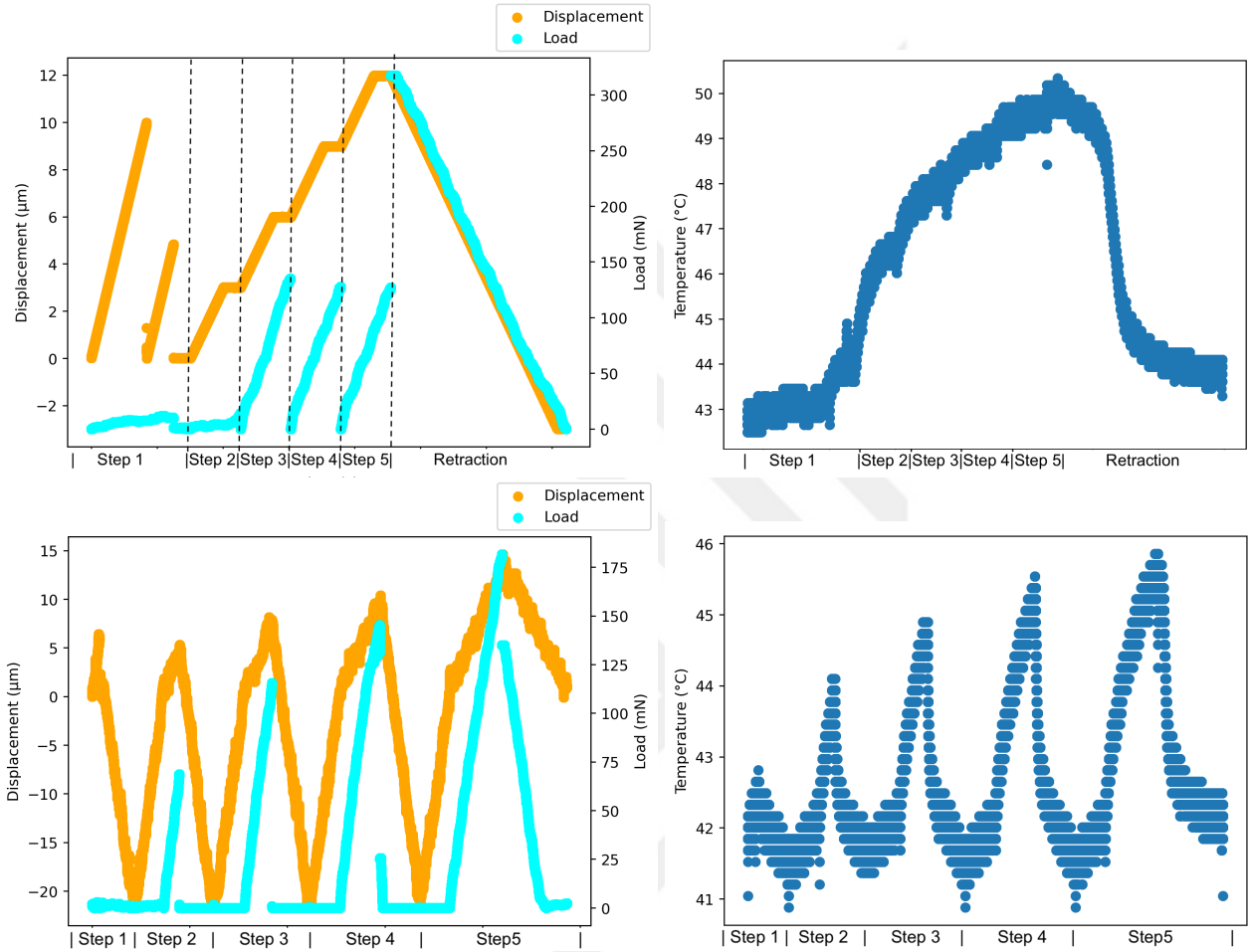

Figure 2.24 : Load and Displacement versus steps (left) and Temperature versus steps (right) graphs of sequential indentation procedure at single location (top) and at different locations (bottom).

of oscillation due to be buried inside the sample after a certain indentation depth is solved. Therefore, amplitude sweeping after reaching to contact could be more explanatory for the sake of decreasing the error through fitting.

2.7.4 Sequential oscillation amplitudes at different locations

This procedure is the same as sweeping oscillation amplitudes of indentation that is mentioned above, except of each oscillation amplitude is applied at a different location after a certain same indentation level. An example experiment result is given in 2.26.

2.7.5 A more comprehensive procedure suggestion

Due to experiences of many experiments, there seems a more accurate procedure to obtain thermal contact time constant at different depths by using oscillations. It is developed to get rid of the problem of not to be cooled at non-contacting (pull back) periods of oscillations.

Actually, the procedure will be proposed is a combination of sequential indent-oscillation cycles and sequential amplitude increase. Therefore, it is presumed that while going deeper inside the sample by each indentation step, oscillation amplitude at each indent level towards to sample will be kept at a constant low value, but pull back periods (half-periods) will be increased such that the tip will be at the initial contact level at every separation period. Consequently, while the plastic deformation part of the work is done by slow indentations, asymmetric to indent level amplitude square wave oscillations would provide high SNR with respect high temperature difference between contact and non-contact cycles.

Furthermore, practically a reverse of that, making oscillations not around the indent level but, only deeper of indent has been experimented. Because, due to material creep and cyclic deformation, loss of contact in some cases had been observed. Hence, oscillating the tip without any initial separation has sustained the presumed contact cycles in actual contact. However, adjusting the indent to oscillation ratio and an adequate alignment of tip has resolved the loose contact problem, so we have not continued on this type of procedure.

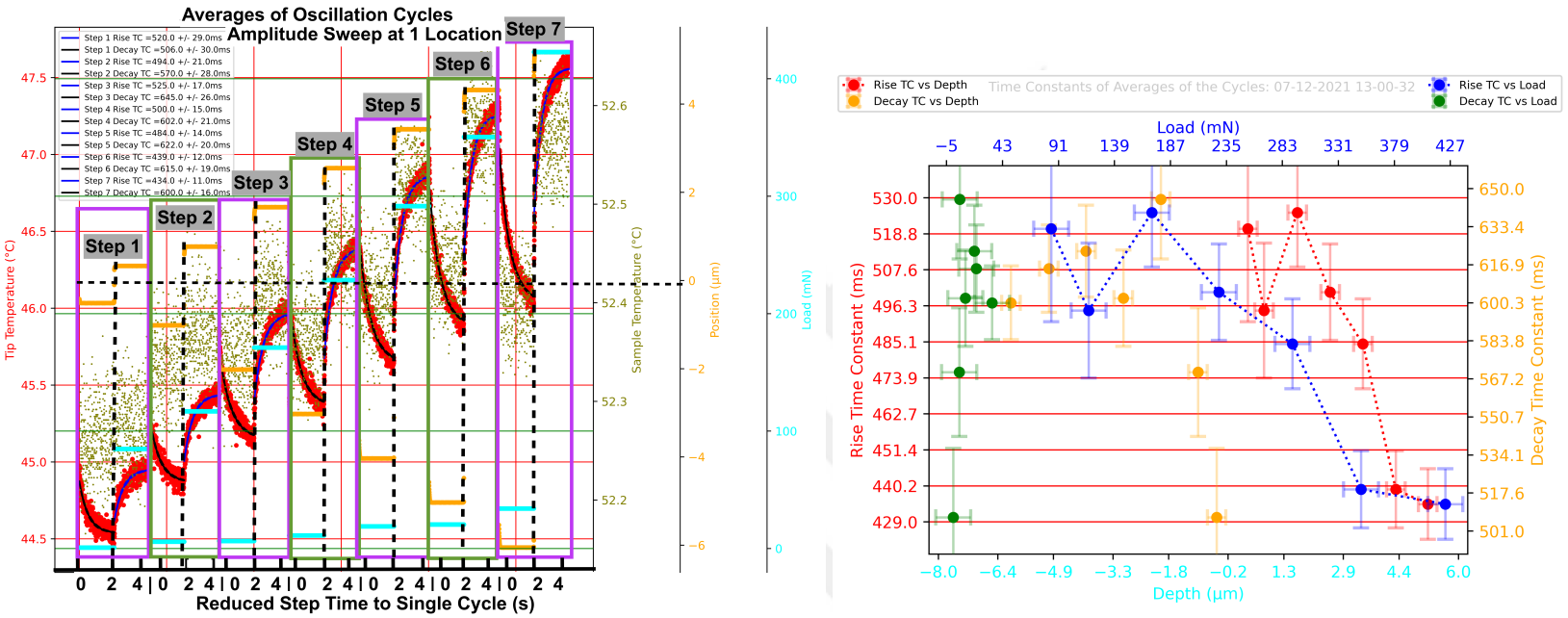

Figure 2.25 : (Left) Averaged cycles of tip (red), sample (green) temperatures, depth (orange) and load (blue) data of a sequential single location oscillation amplitude increase experiment. Horizontal dashed line is put at the average level of the oscillations for steps. The increase in temperature difference between contact and separation (ΔT) can be seen with increasing amplitude. (Right) Time constants (TC) obtained from the rise and decay temperature data at each step, contact time constants show depth and load dependency.

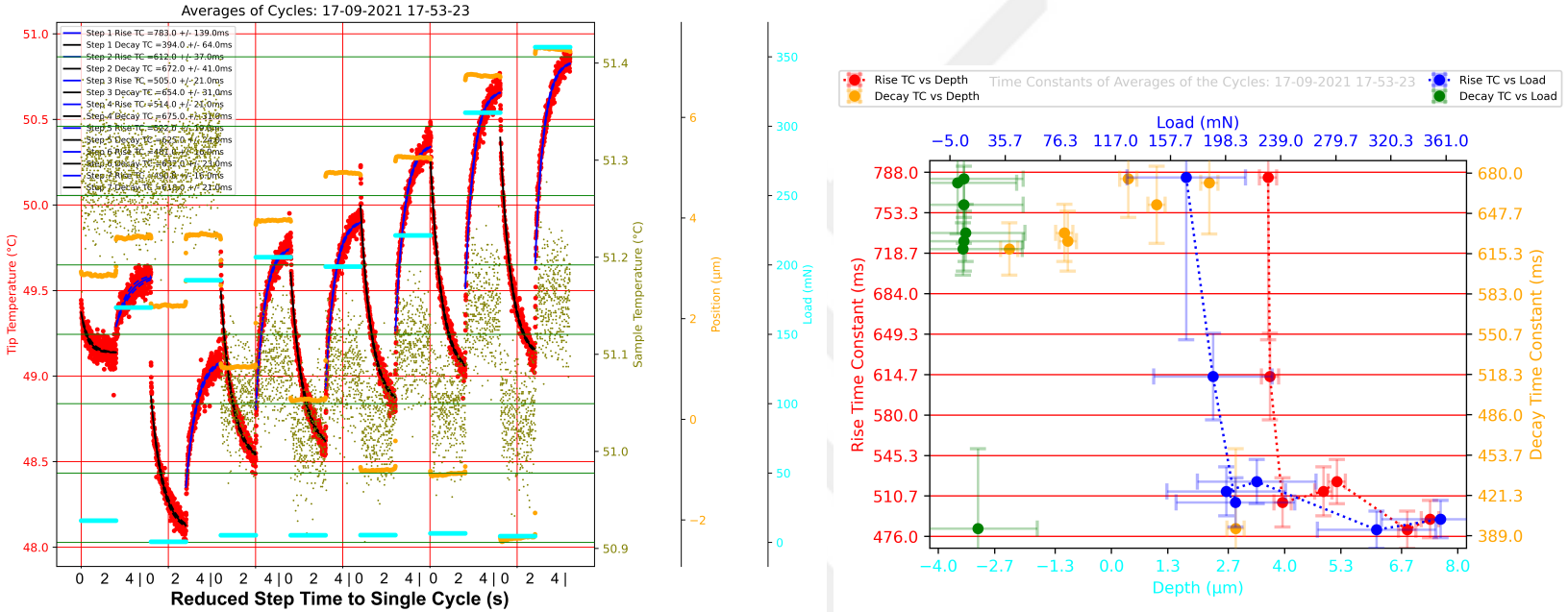

Figure 2.26 : (Left) Averaged cycles of tip (red), sample (green) temperatures, depth (orange) and load (blue) data of a sequential different location oscillation amplitude increase experiment. The increase in temperature difference between contact and separation (ΔT) can be seen with increasing amplitude. (Right) Time constants (TC) obtained from the rise and decay temperature data at each step, contact time constants show depth and load dependency.

3. EXPERIMENTAL RESULTS

Experiments have been conducted with the experimental setup that is mentioned in details in the preceding chapter (Chapter 2). After gathering temperature, depth and load data with respect to time, with the help of the Lumped Analysis introduced at the first chapter (Chapter 1.1), programs have been written to batch processing many experiments. In this chapter, data analysis methods and results of the some of the experiments will be provided.

3.1 Data Analysis

The analysis pursued is mainly focused on extracting time constants from the lumped analysis of averaged cycles of periodic contacts at one depth. Therefore, after raw data is obtained, oscillation cycles' data is subjected to averaging that assumes all cycles are in a quasi-steady situation [51]:

$$T(t_i)_n = T(t_i)_m \tag{3.1}$$

where t_i is the measurement time in between zero to one period, and n and m are the number of any arbitrary cycle. Indeed, this assumption has drawbacks for especially first few cycles, but experiments have been conducted generally for 90 contact-separation cycles, so distortions from the initial cycles are eliminated by averaging. However, investigation of each cycle would be very informative in the manner of analysing deformation mode variation if it was possible. Cycling square-wave and averaging are conducted because of the lack of the signal-to-noise in the thermocouple measurements for the experiments with uncontrolled tip temperature as mentioned in Experimental Setup (Chapter 2). Hence, for the periodic contact experiments, our perspective is limited to extracting the time constant of the prior plastically deformed contact by indentation.

A flow chart demonstration of the data analysis can be seen in the Figure 3.1.

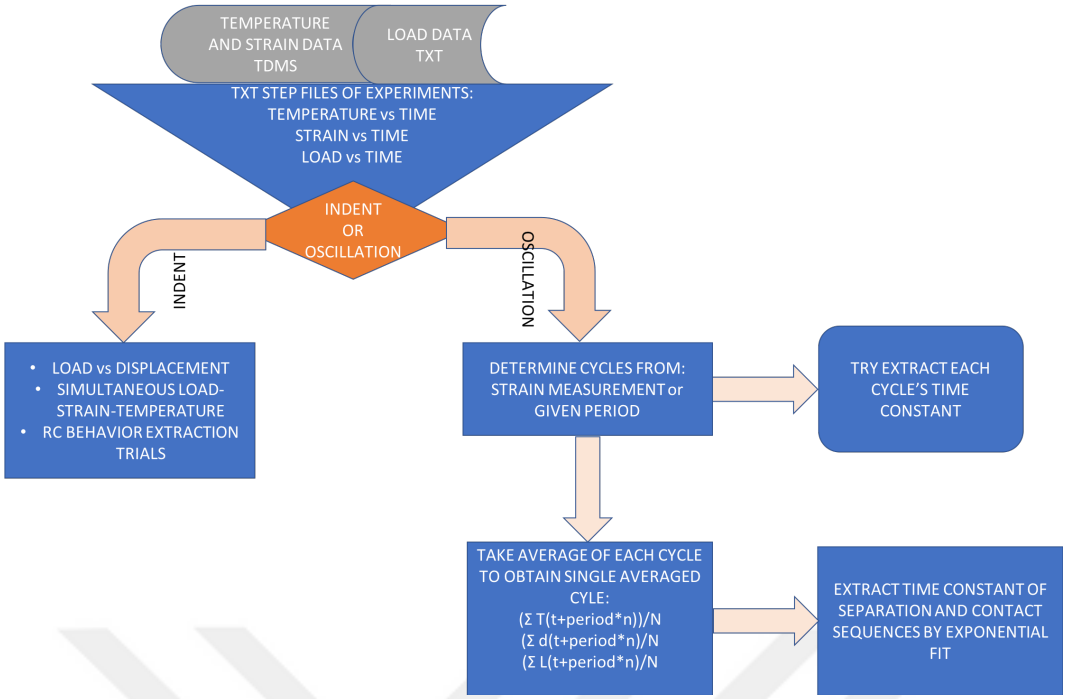

Figure 3.1 : Flow Chart of Data Analysis.

To clarify the concept of averaging with the quasi-steady assumption (eq. 3.1) formula is given below:

$$T(t_i)_{av} = \frac{1}{N}\sum_{n=1}^{N} T(t_i)_n \tag{3.2}$$

where $T(t_i)_{av}$ is the averaged temperature for time t_i in the reduced one period while $T(t_i)_n$ is the temperature of the nth oscillation cycle at the time t_i of that period. The time t_i is the period time that has value between zero to duration of one period. In addition, exception for the averaging protocol has been made for the load measurements due to its low DAQ rate. The averages of load are taken to single value for each contact or separation cycle, rather than each time point averaged separately. This exception does not create any conflict with the the perspective of our analysis due to the fact that we are not interested with impact and time resolved load behavior, but an average contact pressure.

3.1.1 Calculation of thermal time constants

Thermal time constant values are extracted via exponential fit by SciPy package [79] using Python. The exponential function is the result of mentioned lumped analysis can

be written for rise sequences as:

$$T(t) = T_0 + \Delta T(1 - \exp(-t/\tau) \tag{3.3}$$

and, for decay:

$$T(t) = T_0 + \Delta T \exp(-t/\tau) \tag{3.4}$$

Fitting any rise or decay of temperature for a difference ΔT from an initial temperature T_0 gives a time constant τ as mentioned extensively in the Introduction 1.1.

3.1.2 Error and uncertainty analysis

There are several errors occur due to instrumentation and DAQ as mentioned in the Experimental Setup (Chapter 2). Firstly, K type thermocouple has 1.5 °C resolution in measurement that caused by mostly from the reference junction error. On the other hand, we are not interested in the exact value of temperature, so we keep up with a reference temperature of 25 °C for the cold junction. Measurements of the temperature of the setup vary between 20 °C to 30 °C while an average of 22 °C has been observed for about 2 years of measurements.

Moreover, we have not used direct measurement of temperature but the averaged difference between contact and separation by an exponential fit. Hence, for the extracted time constants, we rely on the variance values of the fit parameters that included the absolute error of the averaging. Uncertainty reduction by averaging is a simple form of the uncertainty of the weighted averaging. Simplification to averaging of oscillations is due to the fact that all measurements are considered with the same uncertainty. Hence, weighted averaging of temperatures with the same weights and equation given for averaging (3.2) validated. The uncertainty of average for 90 cycles with 0.75 K uncertainty (1.5 K resolution) [80]:

$$\sigma = \sqrt{\frac{1}{\sum_i^N \frac{1}{\sigma_i^2}}} = \sqrt{\frac{1}{\sum_i^{90} \frac{1}{0.75^2}}} = 0.079 \approx 0.08 \tag{3.5}$$

With the result of the above calculation, one can deduce that about 90 cycles of averaging the uncertainty converges to the limit of used DAQ's resolution of about 0.077 K (see Experimental Setup section for derivations (Chapter 2). Therefore,

selection of 90 cycles is an optimization between the noise reduction and the elapsed time of about 6 minutes (for a general set period of 4 seconds of oscillations).

For the depth and load dependency of the time constants, uncertainty on the depth and load measurements have been considered. In the Indentation Calibrations (Chapter 2.6.4) the depth uncertainty has been investigated deeply. For about $50^{\circ}C$, the depth uncertainty can be calculated with help of Table 2.3 as about 200 nm, and load uncertainty can be used as 2.5 mN. Moreover, for comparison of experiments that was made on different positions, the roughness of the sample should be added for depth dependency of time constants. On the other hand, for the load dependency, we may expect to know contact area dependent load value after touch point in any case, so there should not be a direct effect of roughness on the load dependency of the calculated time constants. The sole evaluation of the depth dependency can be done most accurately through single location sequential experiments that have single touch point uncertainty and sequential increase in the depth. In addition, for the probability of coinciding to an unintentional hollow at the sample deeper than an expected roughness value should be discriminated by distinct load measurement at that indentation depth.

3.1.3 Analysis of extracted time constants

After reaching the TTC of contacts and separations at various load and depth, we may proceed to estimate TCR from the found RCs. Hence, with an agreement on constant capacitance value of the tip, a resistance value can be extracted with equation of τ (1.30).

In the Introduction, several approaches are mentioned for the depth and load dependency of the TCR, and these models will be tried on the extracted RCs. Obtained results' fitness to model functions for constriction model $1/d$, for the proposed fin efficiency functions, and for large scale $\left(\frac{F}{d^2}\right)^m$ type functions will be examined.

Usage of Lumped Analysis has a limiting factor of Biot number, and a rough average estimate has been tried to extract for ensuring of the criteria.

Errors of the extracted RC constants can be correlated to difference between contact and separation temperatures, depth and load. We will investigate how these parameters

affect the error on the time constants found with our method. The absolute σ (uncertainty) values have been found by least square fits' variance parameters (var) such as:

$$\sigma(\%) = 100 var(\tau)/\tau \tag{3.6}$$

Consequently, taking into account of 328 average contact sequence of experiments, we have reached correlation values by Spearman's correlation calculation with help of SciPy library [79] in Python. For the correlation of σ to amplitude and load, weak correlation coefficients are found as (-)0.466 and (-)0.349 respectively. However, for the temperature difference between contact and separation, very high correlation value of (-)0.941 is found with a strong p_0 value of uniqueness as in the order of E-152 has been found. The graphical demonstration of the correlations can be seen in below Figures 3.2,3.3,3.4.

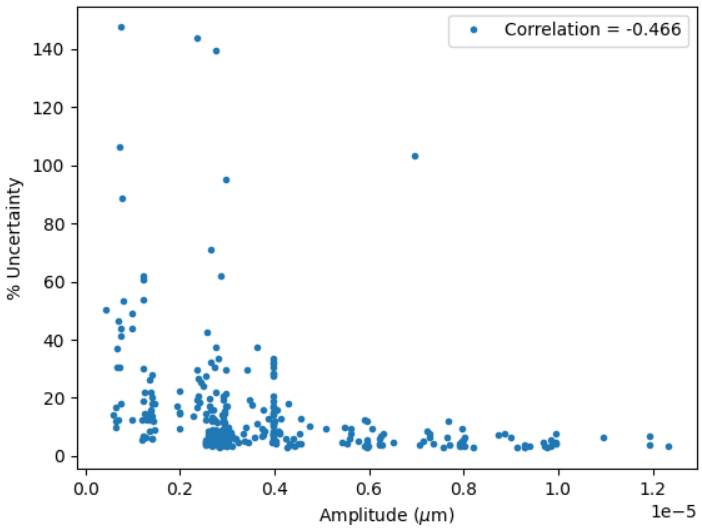

Figure 3.2 : Amplitude versus % Uncertainty.

The correlation results indicate increasing the temperature difference lowers the variance of the exponential rise time constant as can be expected. The difference in the temperature has been provided by amplitude and load difference due to tip temperature has not been controlled, but correlations have not shown the direct-strong relation between σ to amplitude and load. Because, while the amplitude provides the difference, the absolute depth value causes heating up, so cooling down needs more time. Hence, ratio of amplitude to depth may be more convenient in terms of

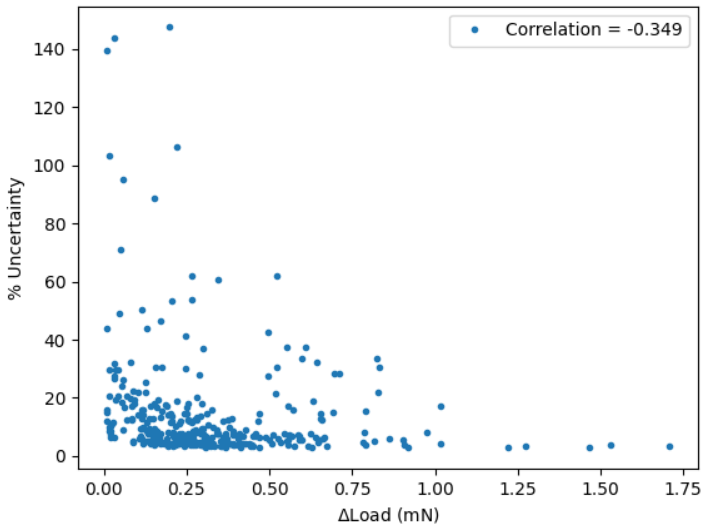

Figure 3.3 : Load Difference versus % Uncertainty.

uncertainty correlation. Lower load correlation can be also deduced to the mentioned ratio dependency, because high load difference indicates deeper indentation when a constant amplitude is given.

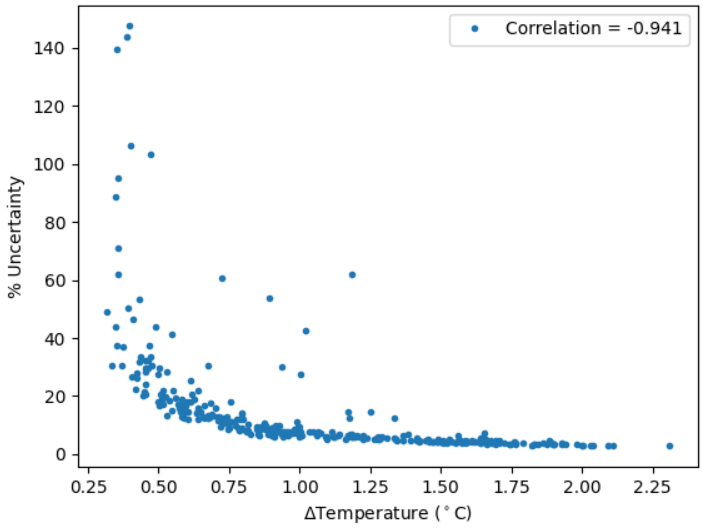

Figure 3.4 : Temperature Difference versus % Uncertainty.

Moreover, some systematic errors will be tried to interpret with the error analyses because, the setup and procedures have been tried first time for TCC extraction with Lumped Analysis. Hence, failure modes and needs for improvements to setup,

procedures and data analysis can be understood with help of the error analyses for our novel approach to TCC subject.

3.2 Metal Samples

Indentations have been made with diamond tips on the metallic samples such as Aluminium (Al), Gold (Au) and Copper (Cu).

The Al sample have been used for first trials of the indenter system as well as for controlled experiments. The Al sample is an SEM holder with measured RMS surface roughness of 108.43 nm (see AFM image in the Figure 3.5). The conductivity of the Al has been taken as 237 W/mK for freshly indented surfaces while pristine surface vulnerable to oxidization. The Al oxide layer for ambient conditions is generally 4-5 μm, but it is found the thickness may be about 500 nm to 1 μm for some situations. The oxide layer can dramatically lower the conductivity to 30-40 W/mK.

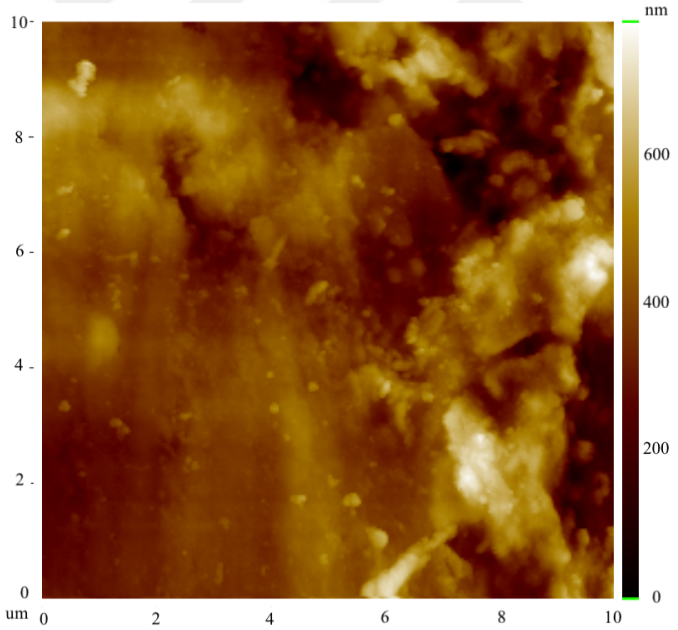

Figure 3.5 : AFM image of Al sample.

The Au samples are foils with 200 and 400 μm thicknesses. Roughness values are measured as 13.96 nm and 38 nm for 200 μm and 400 μm thin foils respectively (see AFM image of the thick sample in the Figure 3.6). The conductivity of the Au samples is used as 315 W/mK that can be found from the literature. There is not any concerns for oxide formation in the ambient conditions, so we will expect to obtain similar

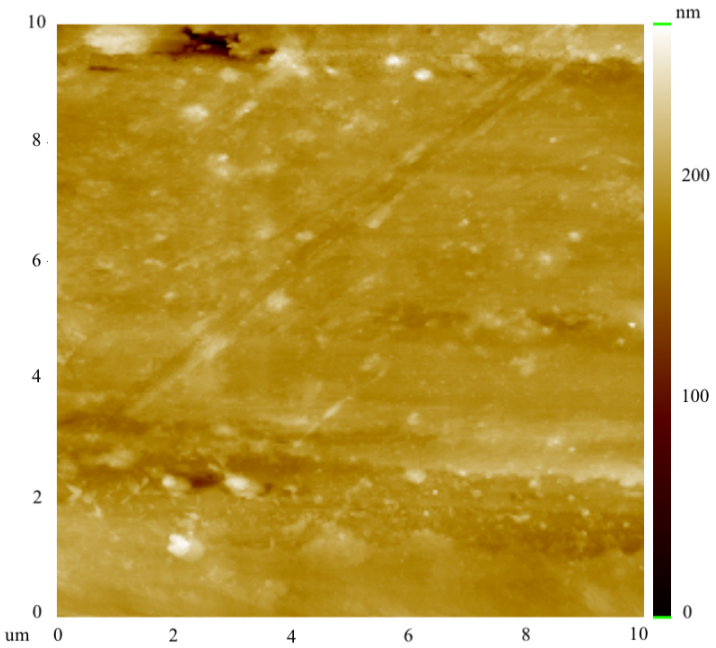

Figure 3.6 : AFM image of Au sample.

diamond-Au contacts during the oscillations and indents in the manner of conductivity of the gold.

The Cu samples are bulk and thin foil (50 μm thickness). Roughness of surfaces are measured as 67.86 nm and 15.5 nm for bulk and foil samples respectively (see AFM images in the Figure 3.7). The highest conductivity value is expected for the Cu with the literature value of 385 W/mK. However, we may encounter with oxide layers or formation of oxides during the indentations and oscillations in the Cu contacts. For the conductivity of the oxide layers of Cu, one can found values between 18 to 76.5 W/mK with typical value of 33 W/mK. Nevertheless, the Cu oxide formation is a slow process when compared to Al, and the thickness of the oxide is given between 10-50 nm which we can overcome with indentations between oscillations or even during the oscillations due to small creep in the contact.

3.3 Results of Truncated Cone Diamond on Metallic Samples

A truncated cone shape of diamond has been used for the most of the experiments. Half cone angle is measured as 60°. Truncated part may be expected to show a similar mechanical behaviour of a flat punch for initial part of the indentations with a radius of

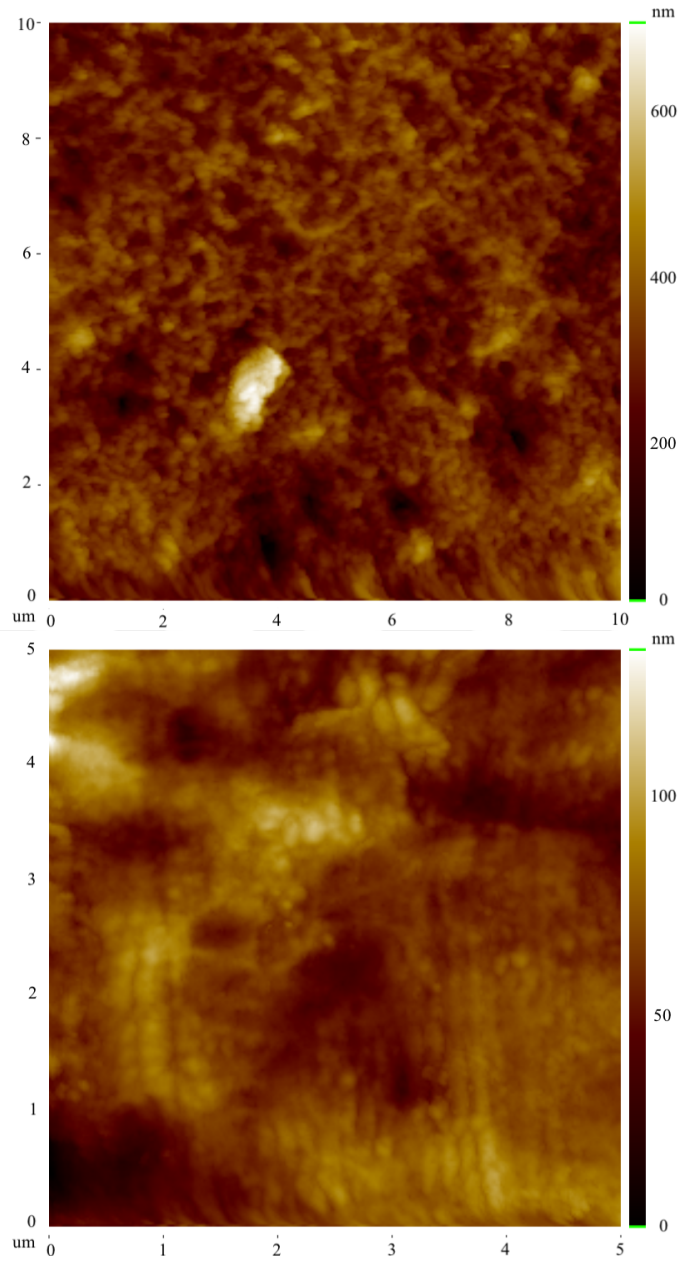

Figure 3.7 : AFM images of Cu samples: left one is bulk sample, right one is foil sample.

5 μm. However, there is an obliqueness that causes to initial spherical-conic tip touch as can be seen from the Figure 3.8.

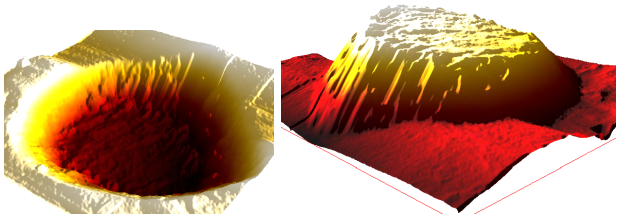

Figure 3.8 : AFM images of the indentations on Copper foil (left) 3D topography image, (right) reversed topography image to reveal the truncated cone tip shape. Maximum height was measured as 278 nm for the 20 by 20 μm^2 area

Nevertheless, the angular misalignment is calculated as about 3°, and the height of the oblique flat part is about 75 nm which is even lower than our smallest general prior indentation depth of 2 μm. Therefore, we will mention about the tip with the name truncated cone, and area functions will be simplified as below unless otherwise stated.

$$A_{pro} = \pi[R_0 + tan\theta d]^2 = \pi[R_0^2 + 2R_0 tan\theta d + tan^2\theta d^2] = \pi[25 + 17.32d + 3d^2] \quad (3.7)$$

$$A_{cont} = \pi\left[\frac{(d+d_0)^2 tan\theta - R_0 d_0}{cos\theta} + R_0^2\right] = \pi[2((d+2.9)^2 1.732 - 14.45) + 25] \quad (3.8)$$

The area functions are given in the μm^2 units, R_0 is the radius of the flat tip of the truncated cone, and d_0 is the height of truncated part of the cone where A_{pro} and A_{con} indicates the projected and contact area.

The capacitance of truncated cone is estimated by the volume and literature values of density and specific mass of the diamond. The estimation is made for rough calculations of Biot number and validation of extracted fit parameters by correlating them to conductance and conductivity values. The base of the cone has 250 μm radius, therefore one can estimate the mass of the diamond as about 34 μg, so capacitance can be found as 0.184 E-4 J/K by using the specific heat capacity value of 0.54 $Jg^{-1}K^{-1}$. Hence, capacitance (C) values can be estimated roughly as in the order of 10^{-5}.

3.3.1 Overall results

Results with truncated cone tip have been assessed in many aspects, and ensured 46 different experiments with three different mentioned metallic samples selected to be evaluated (Figures 3.9 3.10).

Overall results of time constant measurements for contact sequences demonstrate a rapid initial drop followed by a slower reduction with increasing indentation depth. Moreover, load dependency of time constants for different experiments seem to be more compatible with each other when compared to depth behavior. It may be interpreted with the uncertainties of depth measurement that is vulnerable to inconsistencies in touch point and machine compliance between different experiments. On the other hand, load measurement shows a general consistency between different experiments, especially for the Au sample.

Separation sequences (retraction of the tip from the sample) does not show a depth correlation as can be expected, but if the amount of elastic recovery were equal or more than the peak-to-peak of oscillation we can observe a distinct low time constant for cooling down sequences. Besides, for some sequential amplitude increase experiments, we have encountered monotonic decrease in time constant with increased amplitude due to increase in the amount of separation (gap) between the tip and the hot sample.

The mean, minimum and maximum values for different samples are given in Table 3.1.

Table 3.1 : Summary of Time Constant Measurements with Truncated Cone Tip.

Truncated Cone **Contact Sequences**	**Mean (ms)**	**Minimum (ms)**	**Maximum (ms)**
Aluminium	638.4	318.31	2493.4
Gold	502.6	30.25	1076.7
Copper	618.2	218.1	1827.64
Separation Sequences			
Aluminium	693.5	321.1	3333.2
Gold	591.5	100.1	891.3
Copper	625.1	342.7	1601

To make a rough estimation for compliance with the Lumped Criteria due to Biot number as indicated in the Introduction [1.1], the minimum time constant measurement can be investigated for the worst case scenario. The overall area is estimated as 0.24 E-6 m^2, and maximum contact area can be approximated to 3.5 E-9 m^2, so contact area to overall area ratio is roughly 1%. Using the equation 1.2 and area for truncated cone,

the criteria can be simplified as:

$$Bi = \frac{h_c A_c}{kA/L} = \frac{h_c A_c}{3.3} = \frac{C}{3.3\tau} (<< 0.1) \tag{3.9}$$

Therefore, we can estimate the Biot number for the minimum time constant measurement of 30 ms as in the order of E-4 which is well-below the limit of the E-1. In addition, using the table and the contact area estimation, we may estimate the conductance values that are extracted through the experiments in the range of E+4 to E+6, and the limit value for the criteria compatibility as E+8 of conductance can be thought. However, rather than relying on the individual measurements, we will try to use the proposed contact resistance models for parameter estimation that may be more accurate to comment on.

3.3.2 Pressure and depth dependencies

After the time constants were obtained, the variation of them with respect to depth and pressure have been tried to be analysed and fitted to a reasonable model.

The first known dependency of the time constant gathered from the Lumped Analysis is direct area dependency for a constant surface conductance and capacitance (see fits in the Figure 3.11).

Indeed we do not assume a constant surface conductance that is independent from the area, but for a rough estimation of Biot number, and to show how much problematic to approach micro-scale junction with this model it has been tried to fit the time constants to the area. Moreover, the disc constriction resistance model of inverse depth (or square root area) (see Figures 3.12 and 3.13) and proposed area efficiency functions that are similar to conical (see Figures 3.16 and 3.17) and cylindrical (see Figures 3.14 and 3.15) fins will be shown. The shape of the tip allows us to try both cylindrical and conical fin approaches due to the fact that it is a truncated cone.

The extracted parameters are shown in graphs with thermal diffusivity per volume, because, the fit parameter for disc resistance model consists of capacitance to (harmonic) conductivity with some dimensionless coefficients. Therefore, we have given the inverse of fit parameters with dimensional similarity to thermal diffusivity which is easier to investigate.

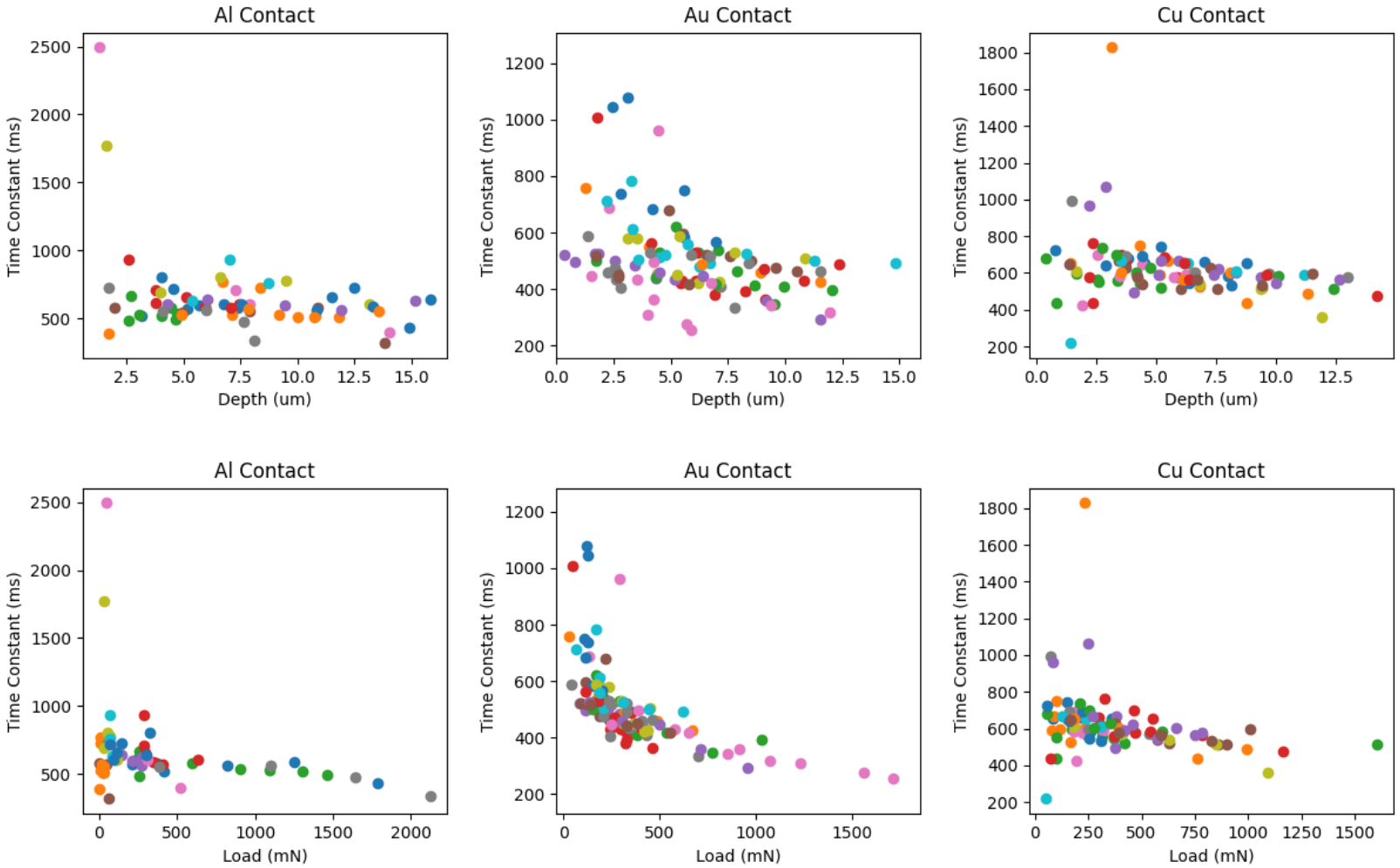

Figure 3.9 : Contact sequences time constants for truncated cone tip with Al (right), Au (middle), Cu (left) samples (Each color represents a different experiment.). Top graphs show depth versus time constant, and bottom graphs show load versus time constant.

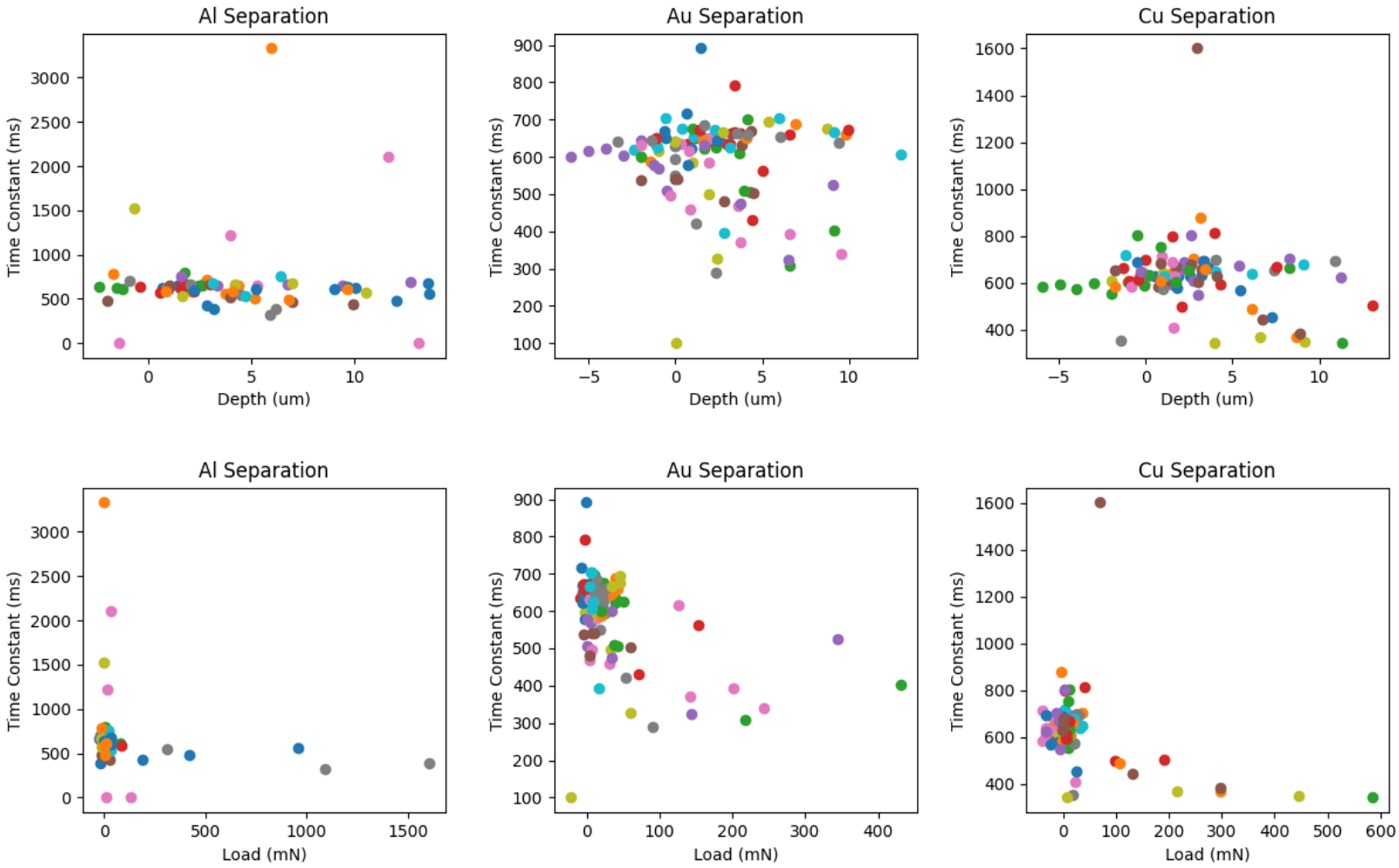

Figure 3.10 : Separation sequences time constants for truncated cone tip with Al (right), Au (middle), Cu (left) samples (Each color represents a different experiment.). Top graphs show depth versus time constant, and bottom graphs show load versus time constant.

The fit functions and the corresponding parameters is given below:

For the modified disc constriction function (see details in Introduction 1):

$$\tau = RC = \frac{C}{hA} = \frac{C}{2k'c_0 tan(\theta)d} = \frac{3.464}{c_0}\frac{C}{k'}\left(\frac{1}{d}\right) = p_0\left(\frac{1}{d}\right) \tag{3.10}$$

Thus, the inverse of the parameter p_0 can be defined as thermal diffusivity per volume. Indeed, it is not a physically meaningful parameter, but after multiplication by the volume of the tip it will provide us an effective thermal diffusivity for the contact.

The ratio of the efficiency fit parameters can also be given as thermal diffusivity per volume as explained in the Introduction (Chapter 1.2.1). In addition, the coefficient of the tangent hyperbolic and Bessel functions have been investigated separately, and conductance parameters that are extracted through this fit parameter will be evaluated too.

For the cylindrical efficiency function included constriction model (see details in Introduction 1.2.1):

$$\tau = RC = \frac{C}{hA\eta} = \left(c_1\frac{(1+r/2d)}{tanh(c_2(d+r/2))}\right) \tag{3.11}$$

where the constants represents:

$$c_1 = \frac{C}{3.464k'c_0}\sqrt{\frac{2h}{kr}} \tag{3.12}$$

$$c_2 = \sqrt{\frac{2h}{kr}} \approx 14.142\sqrt{h} \tag{3.13}$$

For the conical efficiency function included constriction model (see details in Introduction 1.2.1):

$$\tau = RC = \frac{C}{hA\eta} = \left(\frac{c_1}{\sqrt{d}}\frac{I_1(c_2\sqrt{d})}{I_2(c_2\sqrt{d})}\right) \tag{3.14}$$

where the constants represents:

$$c_1 = \frac{C}{k'c_0}\sqrt{\frac{2h}{ktan(\theta)}} \tag{3.15}$$

$$c_2 = \sqrt{\frac{8h}{ktan(\theta)}} \approx 0.0481\sqrt{h} \tag{3.16}$$

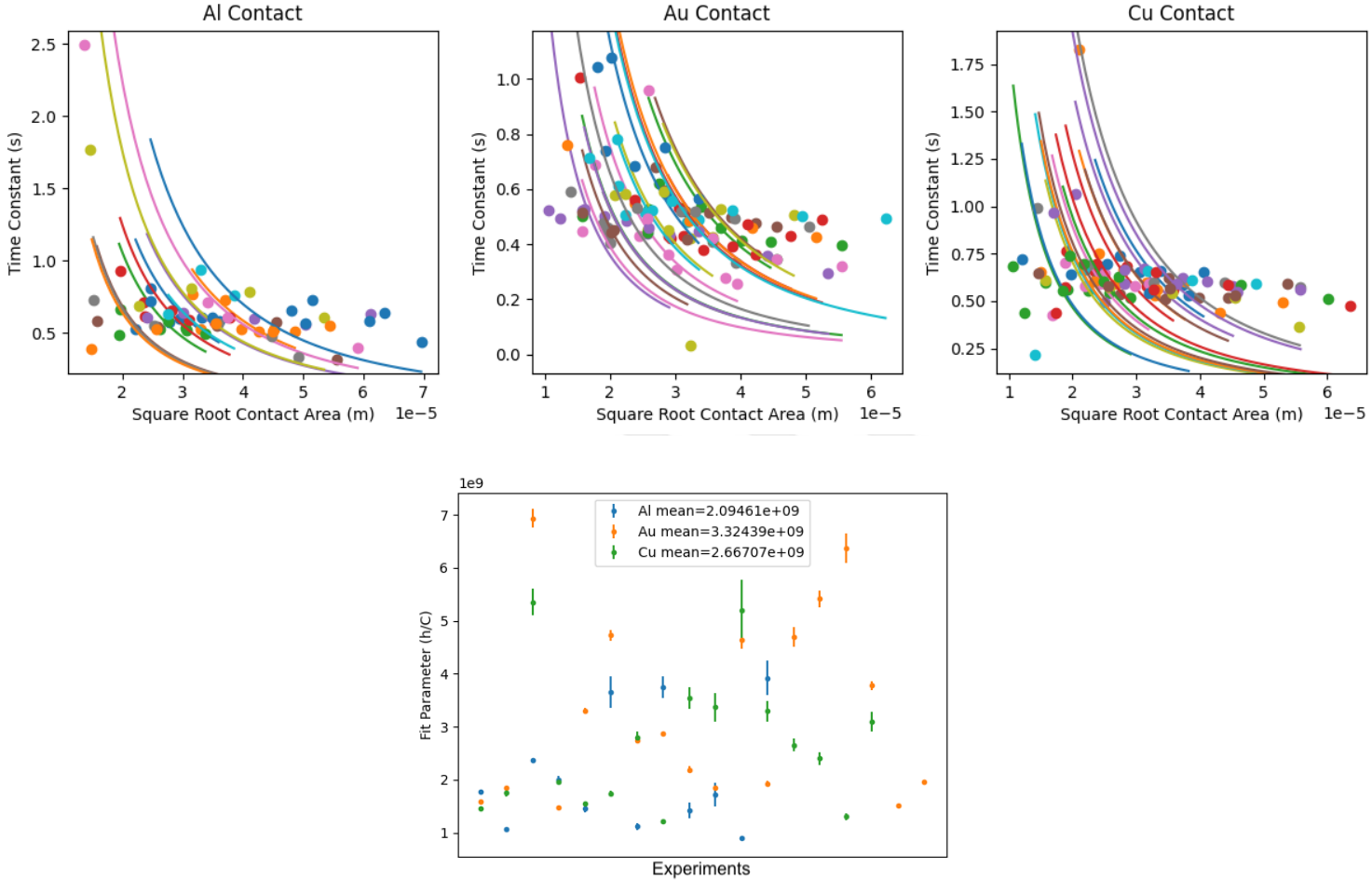

Figure 3.11 : Top graphs (diamond tip contact with Al (right), Au (middle), Cu (left)) show area fits graphically on the each experiment while bottom graph shows fit parameter calculated for each.

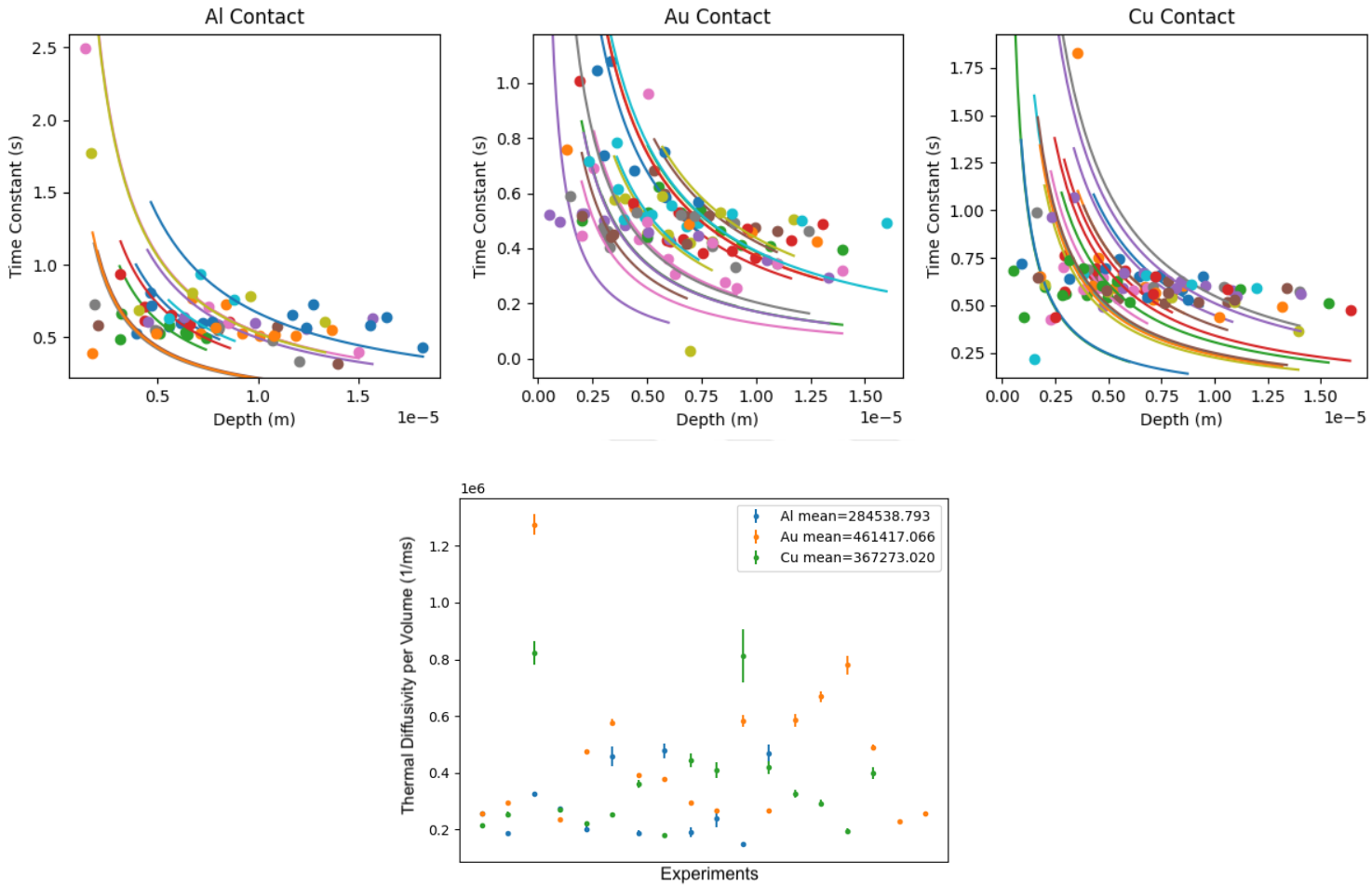

Figure 3.12 : Top graphs (diamond tip contact with Al (right), Au (middle), Cu (left)) show inverse depth fits graphically on the each experiment while bottom graph shows thermal diffusivity per volume calculated for each.

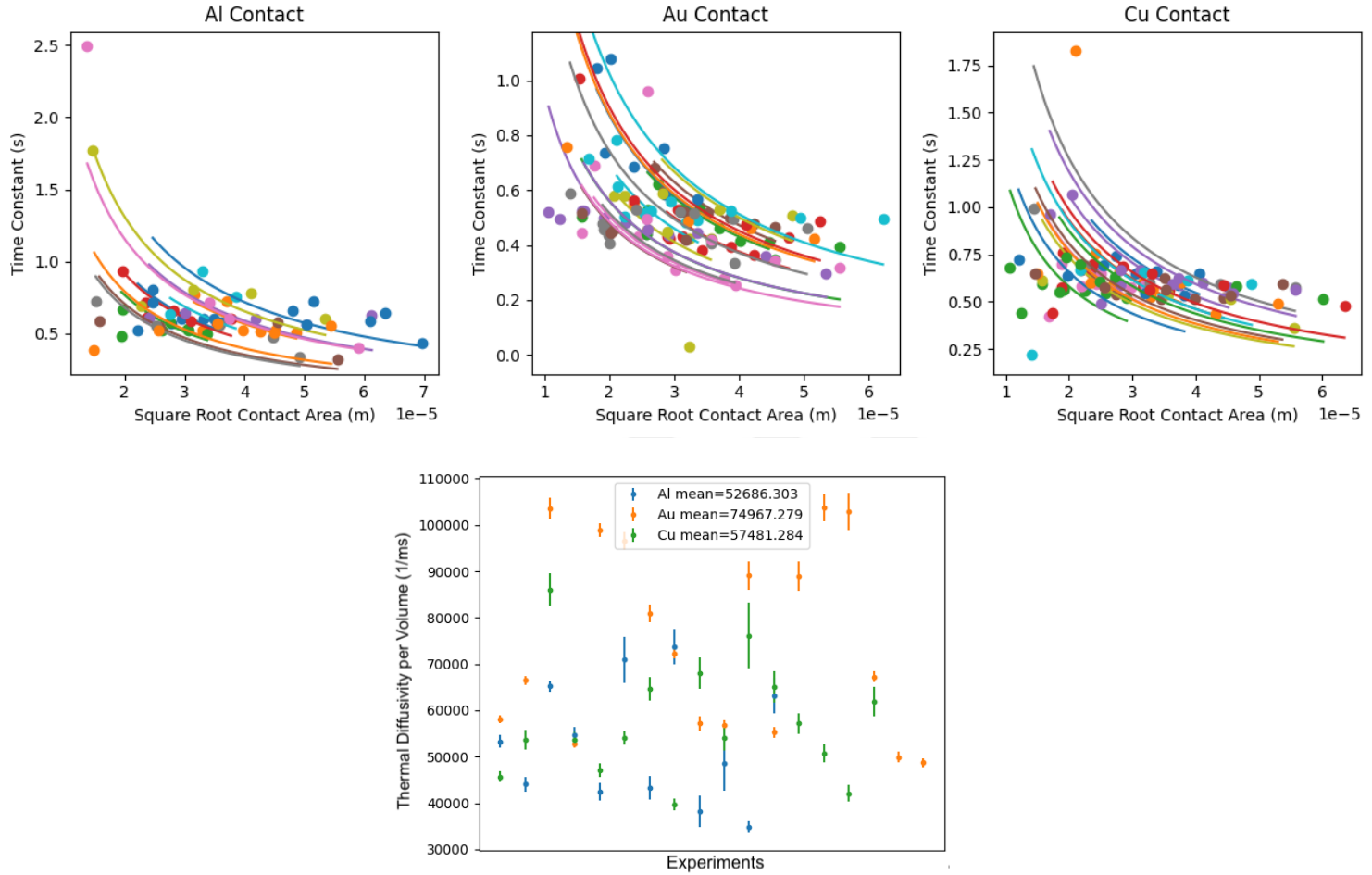

Figure 3.13 : Top graphs (diamond tip contact with Al (right), Au (middle), Cu (left)) show inverse square root area fits graphically on the each experiment while bottom graph shows thermal diffusivity per volume calculated for each.

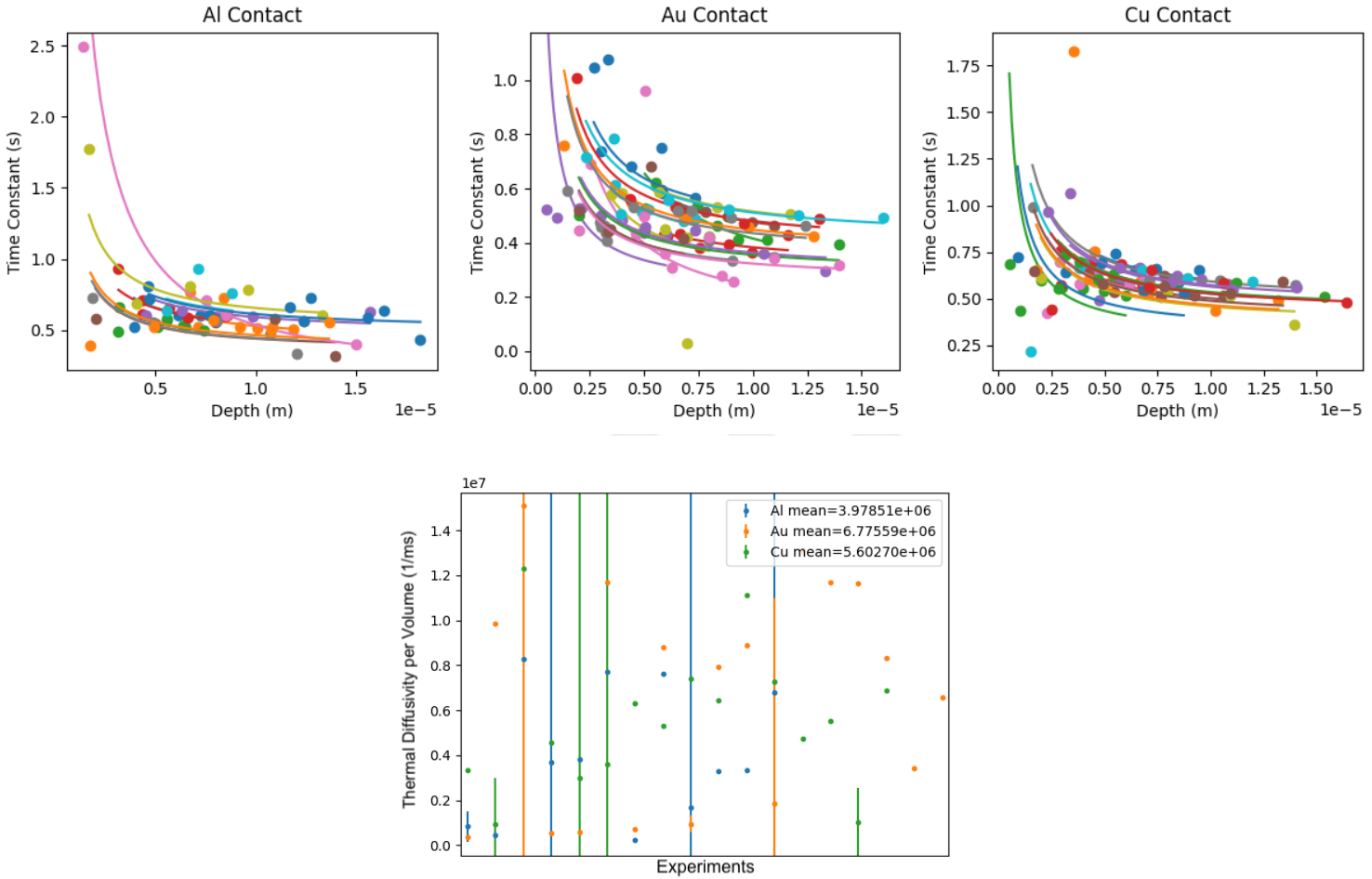

Figure 3.14 : Top graphs (diamond tip contact with Al (right), Au (middle), Cu (left)) show cylindrical efficiency depth dependent fits graphically on the each experiment while bottom graph shows thermal diffusivity per volume calculated for each.

Table 3.2 : Surface Conductance ($Wm^{-2}K^{-1}$) Estimations from Different Fit Functions (Note that for parameter obtained from the direct area fit (quadratic) conductance is a total while for the other fits it is assumed that the parameter is for pure interface of diamond-metal contact.)

Sample	$h_{quadratic}$	$h_{Cylinder}$	$h_{Cylinder\sqrt{A}}$	h_{Cone}	$h_{Cone\sqrt{A}}$
Al	3.86 E+4	1.28 E+10	1.38 E+8	1.58 E+13	4.59 E+12
Au	6.11 E+4	2.06 E+10	3.58 E+7	1.71 E+13	3.23 E+12
Cu	4.91 E+4	2.33 E+10	2.72 E+8	2.07 E+13	4.9 E+12

Therefore, we may find the thermal diffusivity values by multiplying the thermal diffusivity per volume parameters with volume of the tip and the constants to obtain a physically meaningful value. Moreover, the square of efficiency function fits' c_2 parameter would give a surface conductance parameter for the diamond-metal interface that is not exposed to a constriction (of microscale) resistance.

In Table 3.2, one can evaluate the surface conductance (per area) results for diamond-metal contacts that are found from the area fit and mentioned c_2 parameter from the conic and cylindrical fits. The results from the area fit give values about the real contact conductance that are calculated with constant contact conductance and diamond tip's capacitance estimation. On the other hand, we deduced the conductance values from the efficiency functions are for the metal-diamond interface (i.e. nanoscale contact conductance) that are calculated with shape and conductivity of diamond. Therefore, there are 6 to 9 order of magnitude difference has been found between total conductance and interface conductance. The compliance of indirect result of efficiency fit with the order of magnitude of conductance for metal-diamond junction demonstrates the accuracy of the approach.

Furthermore, depth dependent conic fin efficiency fit shows the highest conductance derivation with E+13 , and cylindrical square root area dependent cylindrical fits calculate the lowest conductance values in the order of E+8. For depth dependent fits of conic and cylinder efficiency functions, the results are found in the order of conductivities of the metals from the lowest Al to the highest Cu. These results also show that, the efficiency fits of TTC can reveal the interface, even though the actual single values of contact conductance show different order as we see the order of overall surface conductance values Al, Cu and Au from the lowest to the highest.

Table 3.3 : Thermal diffusivity (α) (cm^2/s) estimation from the average of fit parameters for the contacts of diamond tip with the Al, Au and Cu samples. $\sqrt{A}$ denotes that fit was made by using the square root area instead of the depth directly.

Sample	$\alpha_{1/d}$	$\alpha_{1/\sqrt{A}}$	$\alpha_{Cylinder}$	$\alpha_{Cylinder\sqrt{A}}$	α_{Cone}	$\alpha_{Cone\sqrt{A}}$
Al	0.79 E-2	0.26 E-2	0.11	0.015	0.895	0.039
Au	1.29 E-2	0.36 E-2	0.19	0.01	1.26	0.42
Cu	1.03 E-2	0.28 E-2	0.16	0.022	1.08	0.396

The literature values of thermal diffusivity of the diamond, Al, Au and Cu are 3, 0.97, 1.27, 1.11 cm^2s^{-1} respectively. For the temperature measurements through the diamond tip depending on the contact with the metal sample, we may expect to see values between the bulk separate diffusivity values contacting pairs.

Thermal diffusivity calculations from different fit functions can be found at the Table 3.3. The diffusivity calculation is mainly includes the diamond, because thermal capacitance and volume are taken into account for the diamond tip. Therefore, we may encounter diffusivity values between the diamond and the contacting metal due to effective conductivity of the contact. This expectation is mostly satisfied by parameters obtained from conic fin efficiency function fitted with depth. Hence, the diffusivity results, geometry of the tip and accurate fitting of conic efficiency function show us depth dependent conic fin efficiency function is the best approach. However, the uncertainties in the volume and truncated conic shape of the tip prohibits us to make conclusive comments.

Table 3.4 : Conductivity ($Wm^{-1}K^{-1}$) estimation from the average of fit parameters for Al, Au and Cu, and comparison with literature by using harmonic conductivity of diamond-metal couple. $\sqrt{A}$ denotes that fit was made by using the square root area instead of the depth directly.

Sample	k_{sample}	$k_{harmonic}$	$k_{1/d}$	$k_{1/\sqrt{A}}$	$k_{Cylinder}$	$k_{Cylinder\sqrt{A}}$
Al	237	423.8	1.51	0.48	21.1	2.85
Au	315	544.3	2.45	0.69	35.9	1.97
Cu	385	645.7	1.95	0.53	29.7	4.1

Sample	k_{Cone}	$k_{Cone\sqrt{A}}$
Al	166.4	71.3
Au	234.0	79.8
Cu	201.5	75.2

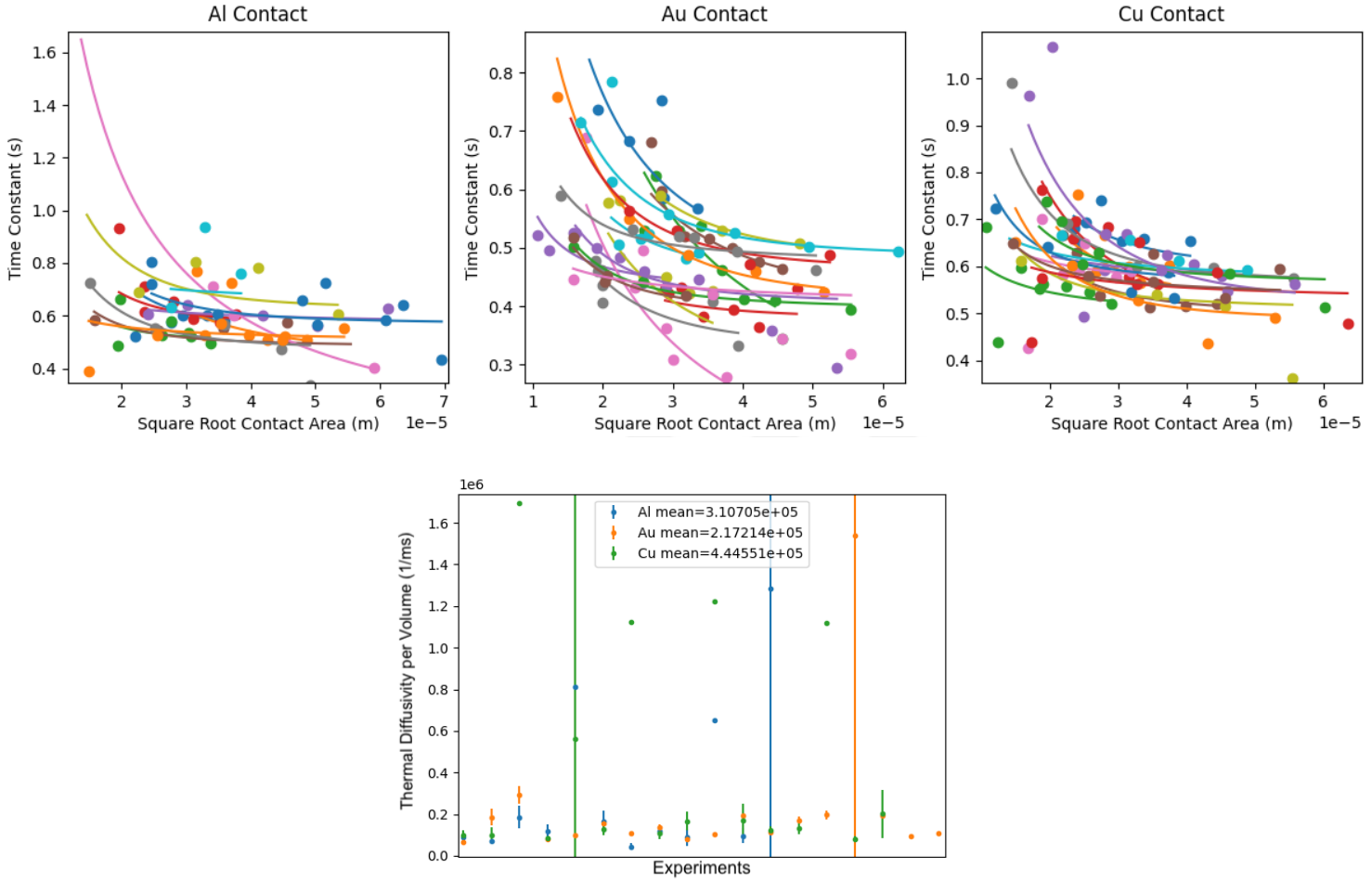

Figure 3.15 : Top graphs (diamond tip contact with Al (right), Au (middle), Cu (left)) show cylindrical efficiency area dependent fits graphically on the each experiment while bottom graph shows thermal diffusivity per volume calculated for each.

Firstly, the results show a ranking independent from the fit function for harmonic conductivity from the lowest to the highest as Al, Cu and Au respectively. This is compatible with the average of the direct TTC measurements too. However, the expectation for the ranking is Al, Au and Cu. It may be partially due to mentioned oxidization and wear effects of impact type testing on copper sample. Yet, the differences are not high as in the literature for conductivity of oxide layers. Therefore, we may also attribute this discrepancy to plasticity effect where the gold has about half of hardness value of copper, and Al can have similar hardness value to gold. Consequently, we may deduce that when the conductivities are similar the hardness becomes effective for the conformity and quality of the contact. Actually the load dependent behavior also shows that gold-diamond contact conductance has high correlation with load. However, if we were to capable to measure true indentation depth inside the sample, we may not conclude this behavior through depth dependent fits. Yet, there is a probability of effect of hardness on development of the interface conductance which we can not make conclusive interpretations with the state of our experimental investigation.

Secondarily, we may interpret the absolute values of the found conductivity values. Due to the fact that the values presented here were found by volume and capacitance estimations, we may encounter discrepancies in the exact numbers. Nevertheless, conic fits give order of magnitude consistency with the expected harmonic conductivities. Yet, they are well-below than theoretical estimation. Therefore, even the behavior of the TTC measurements can be fitted to constriction and area efficiency production, we are far from finding exact numbers. In addition, we have not conducted efficiency function for the exact shape of the indenter, but we have used similar efficiency functions of shapes of cylinder and cone. Hence, we would like to see roughly if this approach works. Moreover, the constriction function of disc that we have used is not exact solution for the case of penetrated tip, and usage of square root area instead of depth trials were made to see an effective disc that is spread through the indentation contact area.

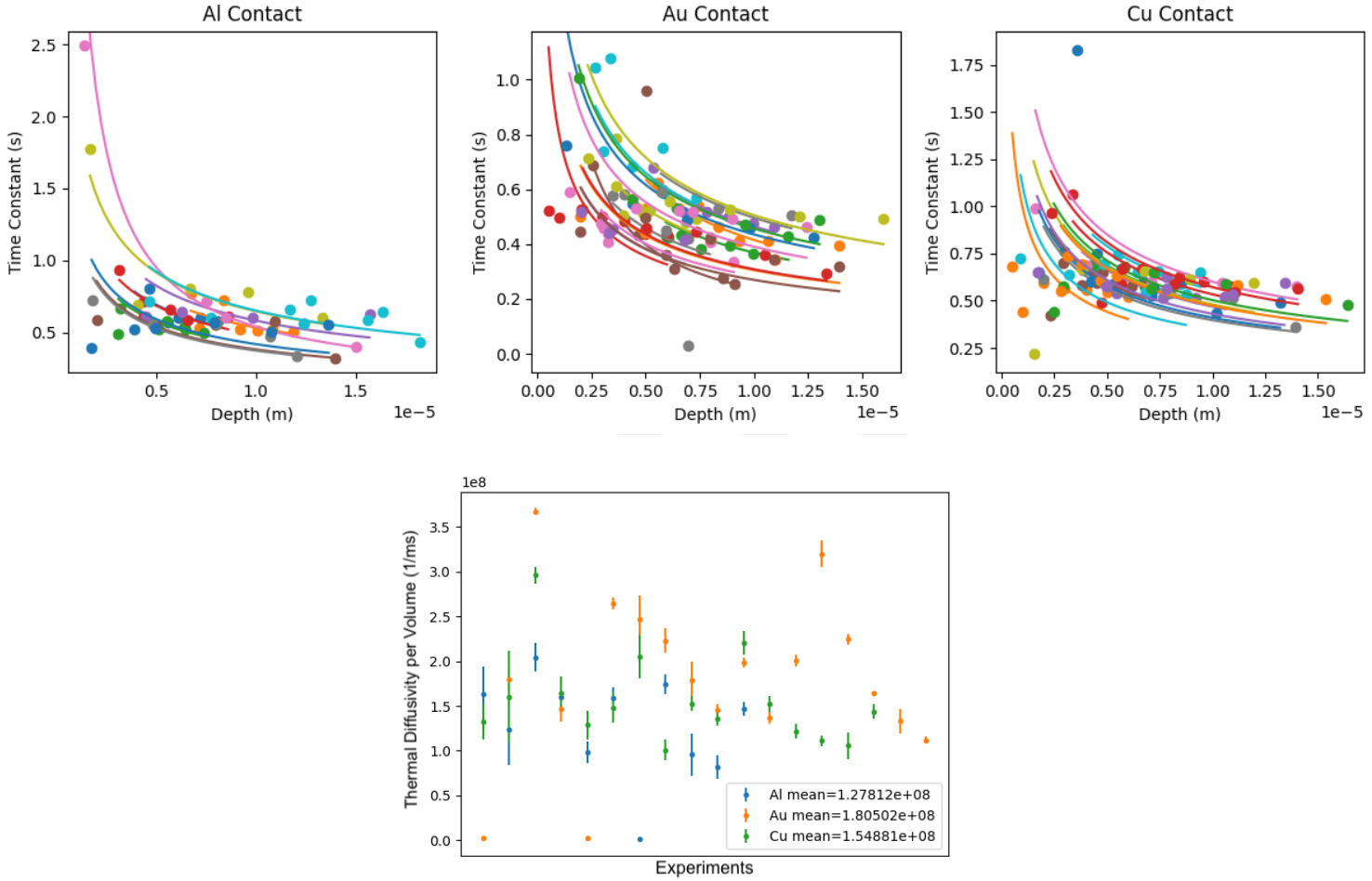

Figure 3.16 : Conic fin area efficiency with depth dependent constriction function fitted to time constant measurements. Top graphs (diamond tip contact with Al (right), Au (middle), Cu (left)) show conic efficiency depth dependent fits graphically on the each experiment while bottom graph shows thermal diffusivity per volume calculated for each.

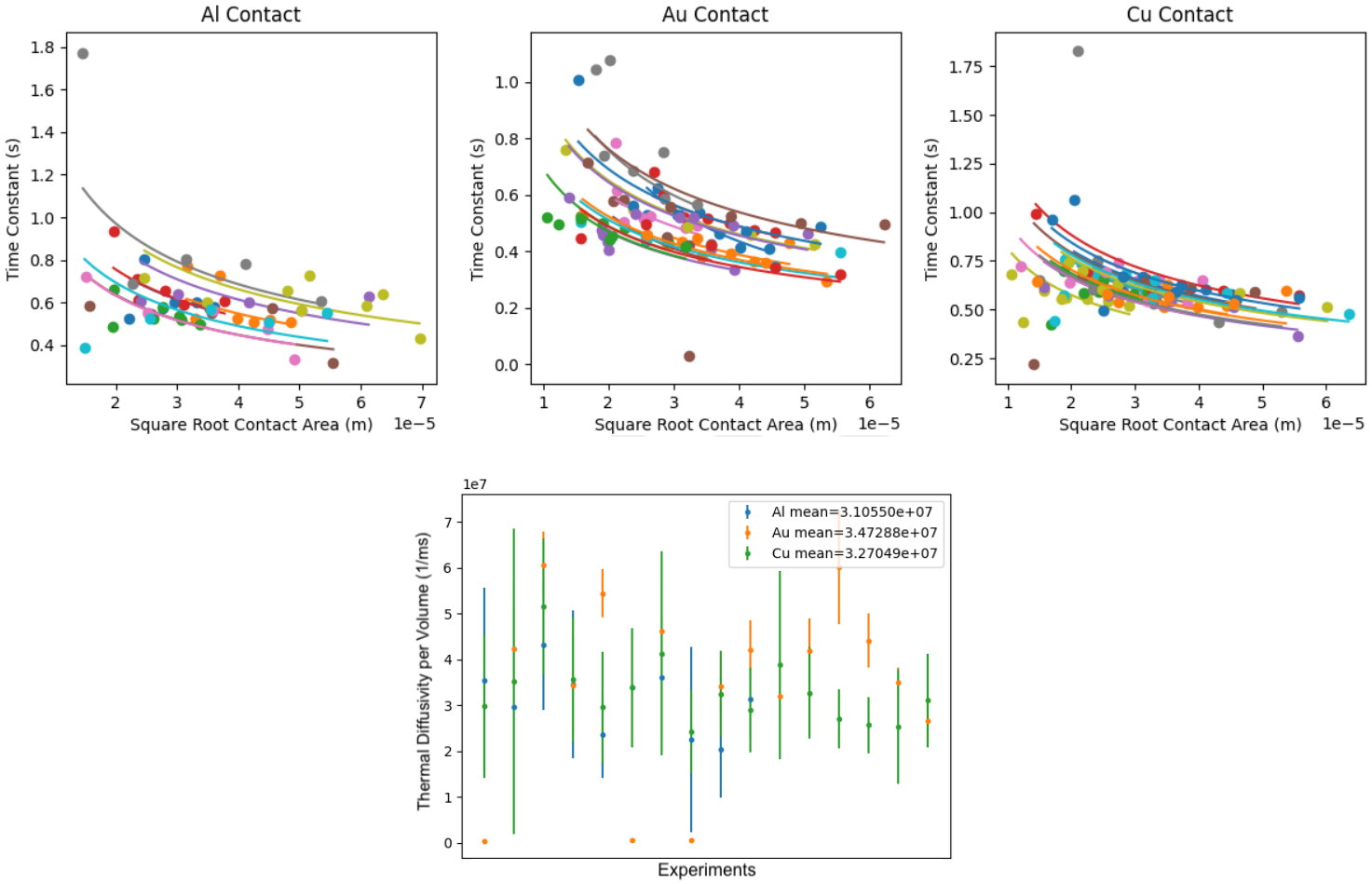

Figure 3.17 : Conic fin area efficiency with square root area dependent constriction function fitted to time constant measurements. Top graphs (diamond tip contact with Al (right), Au (middle), Cu (left)) show conic efficiency area dependent fits graphically on the each experiment while bottom graph shows thermal diffusivity per volume calculated for each.

Even though the absolute numbers seem to be more close to real for the depth used fits, the square root area fits show a good agreement with the TTC measurement, so finding proper proportionality and cross-check with different type of measurements may suggest accuracy of square root area approach.

Pressure dependency relations could not be estimated with the macroscopic picture of contacts as indicated in the Introduction such as:

$$\frac{C}{\tau A_{con}} = h = c_1 \left(\frac{F}{A_{pro}} \right)^{c_2} \tag{3.17}$$

The graphs in the Figure 3.18 show the pressure fit trials with exponent is bounded in the interval of 0-3, and initial guess is given as 0.85 as used in the many studies of literature. Capacitance is estimated as mentioned above in the conductivity calculations.

This results may suggest that we have not reached a contact which can be interpreted as a summation of many microscopic asperities yet. Hence, it seems consistent with our experimental design to elucidate single micro asperity.

3.4 Results of Three-Sided Diamond on Metallic Samples

3.4.1 Overall results

A three-sided (Berkovich-like) diamond micro particle had been prepared for TTC measurements too. However, reliable results with this tip are just 12 experiments with different samples due to the fact that experiments with this tip have been made while development stage of the setup, and thermocouple-tip contact has stability problems (see overall results in Figures 3.19 and 3.20). Average, minimum and maximum values for this berkovich-like tilted tip can be seen on Table 3.5.

Nevertheless, we may show some of the results that are showing depth dependency, and rough calculations for contact conductance. The contact surface calculations for this tip are also problematic due to the extreme obliqueness, so we will avoid to comment on both Biot number considerations and doing square root area type calculations.

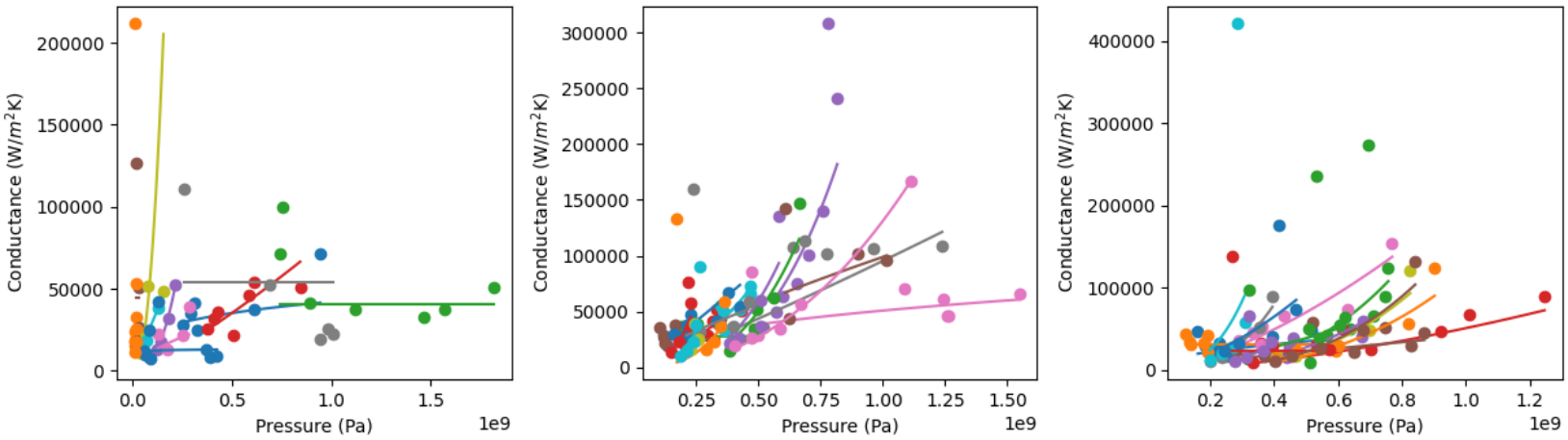

Figure 3.18 : Pressure vs. conductance graph.

The volume of the tip can be rounded to E-9 m^3, so the capaticance for this tip is estimated as 1.89 E-3 J/K. Therefore, according to fit results of time constants that were obtained with the tip, harmonic conductivity values and interface conductance values were estimated. Due to the geometry, we just conducted least square fitting to conic fin and modified constriction functions.

Table 3.5 : Summary of Time Constant Measurements with Berkovich-like Tip

Berkovich-like tip	**Mean (ms)**	**Minimum (ms)**	**Maximum (ms)**
Contact Sequences			
Aluminium	399.4	36	564.4
Gold	423.1	326.1	704.3
Copper	986.9	854.5	1182
Separation Sequences			
Aluminium	693.5	292.1	5444.4
Gold	591.5	419.3	730.5
Copper	625.1	762.4	1856

In Table 3.6, surface conductance estimations with mentioned c_2 parameter for the truncated cone tip can be seen for the tilted berkovich-like tip also. The values seem to be less than literature values with 1-2 order of magnitude less than the expected values.

Table 3.6 : Surface Conductance ($Wm^{-2}K^{-1}$) Estimations from Conic Efficieny Fit Function's c_2 Parameter for contacts of tilted berkovich-like tip (it is assumed that the parameter is for pure interface of diamond-metal contact.)

Sample	h_{Cone}
Al	5.5 E+6
Au	6.7 E+6
Cu	9.9 E+7

In Table 3.7, harmonic conductivity calculations with the conic efficiency fit and constriction fit are shown. The results show a tendency of being more than expected harmonic conductivity values with 1-3 order of magnitudes.

To conclude the results of three-sided diamond tip, due to the lack of knowledge of the exact geometry and contact area, we could not elucidate the contact parameters through the constriction models.

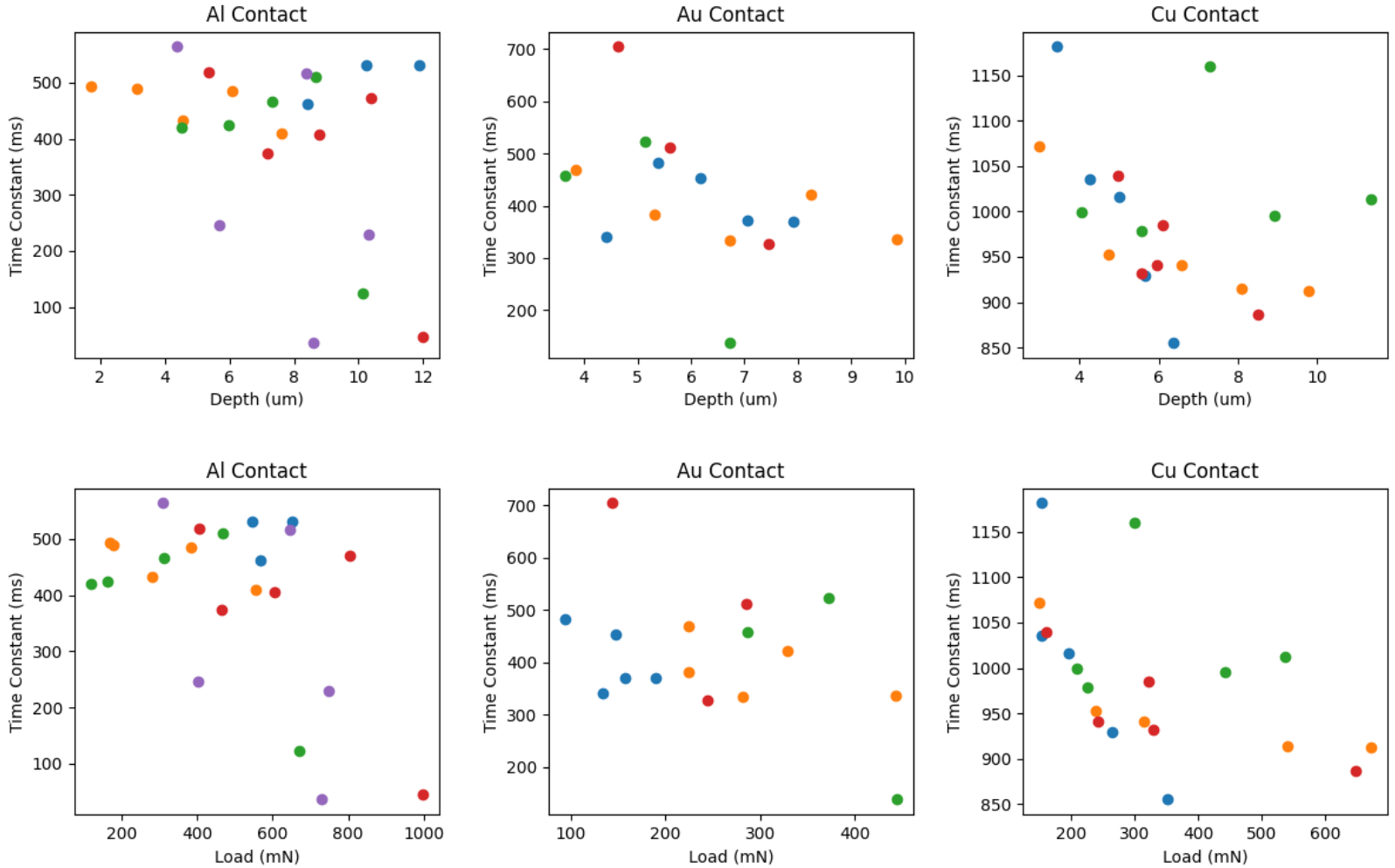

Figure 3.19 : Contact sequences time constants for Berkovich-like Tip with Al (right), Au (middle), Cu (left) samples (Each color represents a different experiment.) Top graphs show depth versus time constant, and bottom graphs show load versus time constant.

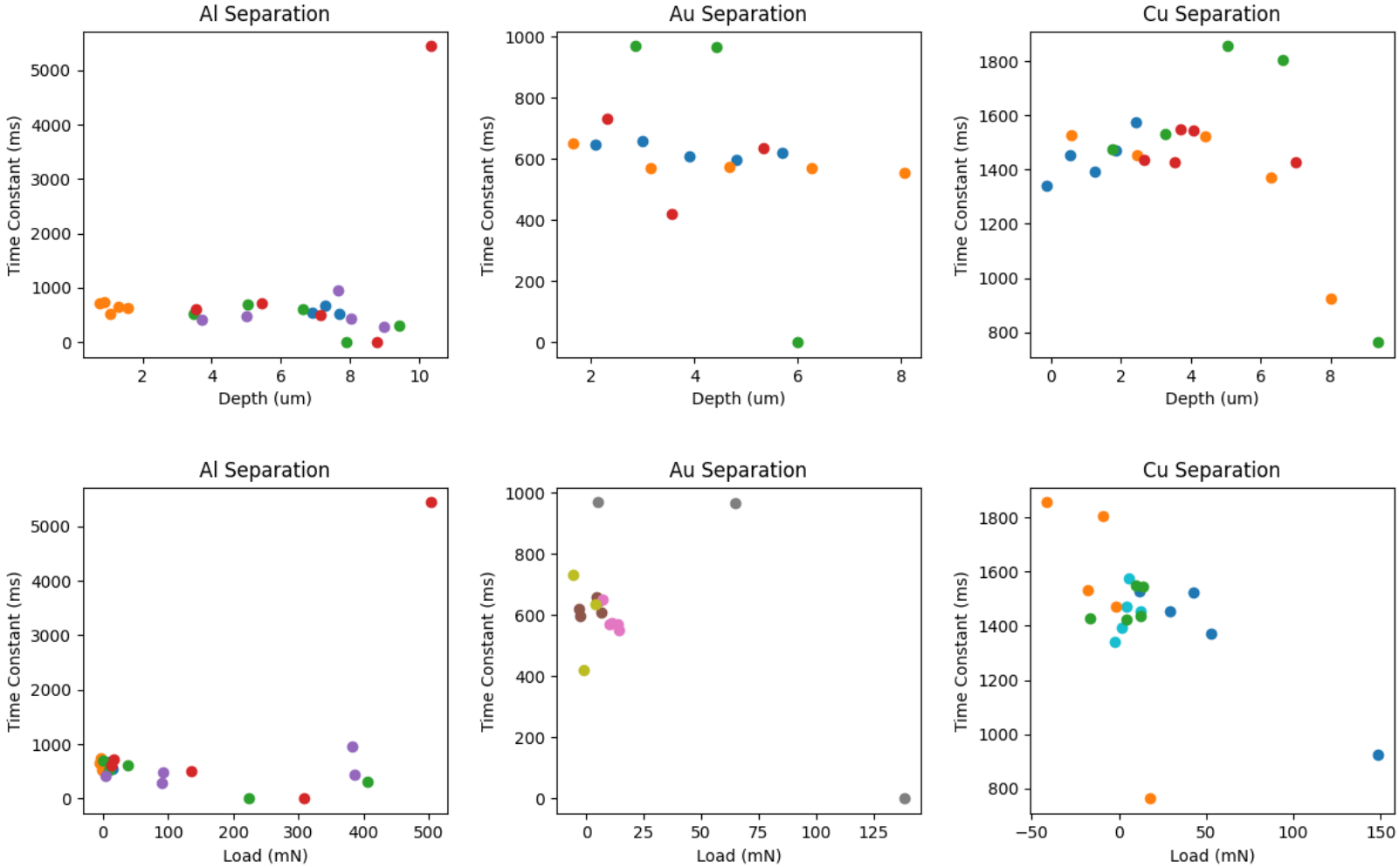

Figure 3.20 : Separation sequences time constants for Berkovich-like Tip with Al (right), Au (middle), Cu (left) samples (Each color represents a different experiment.) Top graphs show depth versus time constant, and bottom graphs show load versus time constant.

Table 3.7 : Conductivity ($Wm^{-1}K^{-1}$) estimation from the average of fit parameters for Al, Au and Cu with tilted berkovich-like tip, and comparison with literature by using harmonic conductivity of diamond-metal couple.

Sample	k_{sample}	$k_{harmonic}$	$k_{1/d}$	k_{Cone}
Al	237	423.8	7750	2.19 E+5
Au	315	544.3	7447	3.02 E+5
Cu	385	645.7	3289	1.8 E+5

Still, we could obtain clear depth dependency in time constants, and with further investigations and advances in the measurment and data analysis, we may measure contact parameters of oblique shapes such as this tilted berkovich-like tip.

4. CALCULATION AND SIMULATION RESULTS

To gain more comprehensive insights on the elastoplastic contacts, some analytical solutions and finite element analyses are conducted. In this section, some important results of calculations and simulations will be mentioned. Firstly, with help of derivations for elastic contacts in the Introduction 1.3, different indenter shapes have been investigated in the manner of area maximization and force minimization in the elastic regime. After that, utilizing the mentioned Fin Approach in the Introduction 1.2.1, efficiency of different geometries have been investigated. In addition to optimization sections, using a commercial FEA program (ABAQUS), several dynamic, static, mechanical, thermal and coupled mechanical-thermal analyses of indentations have been pursued and, some of the results will be provided in the two subsequent sections.

4.1 Elastic Regime Shape Optimization of Indentation Contact Area

As mentioned in the Introduction (Ch.1), it is well known that elastic regime is a very small portion of the indentation. However, except of the pile-up and sink-in effects, shape of the indent is mostly determined by the elastic-geometry dependent relations. Hence, we found precious to investigate with sole elastic calculations to gain insight onto pressure optimization. For instance, the pressure optimization is crucial for especially delicate TIM designs for electronic packaging.

Using the conical area function (eq. 1.9) (with $\beta = tan^2(Radius/Depth)$) and the force-displacement equation (eq. 1.44) an area optimization with respect to cone angle is shown in graph [Figure 4.1].

Cone geometry and depth to force relation provides self-similar depth independent area per force function as shown in the Figure 4.1. Results may seem obvious due to the fact that while cone angle is being extended to 90° it will converge to a flat punch which has the maximum same area over all the forces. This deduction and some other

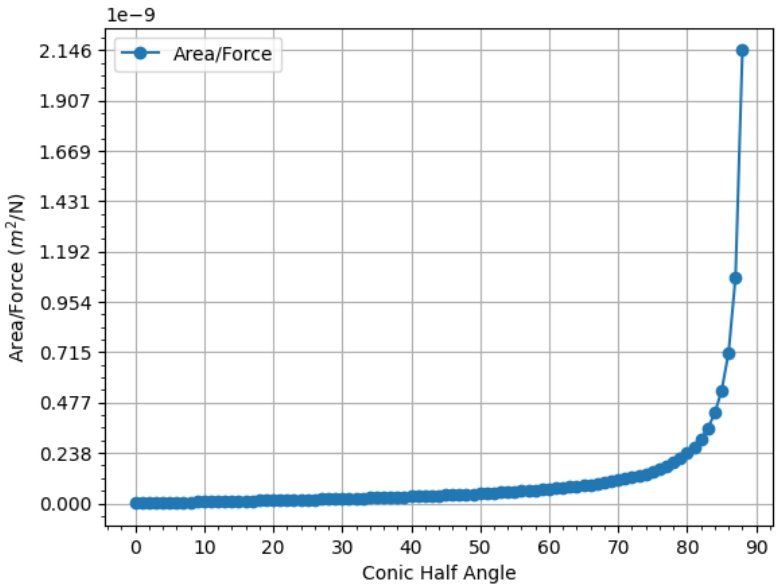

Figure 4.1 : Area to force ratio of different cone angles for elastic regime, material properties are taken into account for diamond indenter and copper sample.

widely-used pointed and spherical geometries calculated with the corresponding area and force relation in the elastic regime (shown in Figure 4.2).

The results of the calculations show pointed indenters become eventually more efficient for the pressure optimization. Knoop shape with the highest cone angle (77°) have the highest area per force while the cube corner with the cone angle of 42° shows the lowest among the pointed indenters. Self similar geometries in the elastic regime show a constant inverse pressure as can be expected from the equations at the Introduction 1.3.

One can also deduce that flat punch becomes less efficient than Knoop, Vickers and Berkovich after indentation depth exceeds the 10% of the radius, while 25% of the radius for the Cube Corner. In addition, for the spherical indenter, when the indentation depth exceeds about 5% of the radius, Knoop shape becomes more efficient, and this ratio is 10% for the Berkovich and the Vickers shapes. We avoid to make comparison for the cube corner to spherical indenter cases for two reasons. First, elastic equations for spherical indentation need to have high radius to depth ratio to be valid. Second, it is obvious that even 1 μm is a big extension for the elastic regime, so intersection at about 3-4 μm of spherical and cube corner may not be that correct. However, we

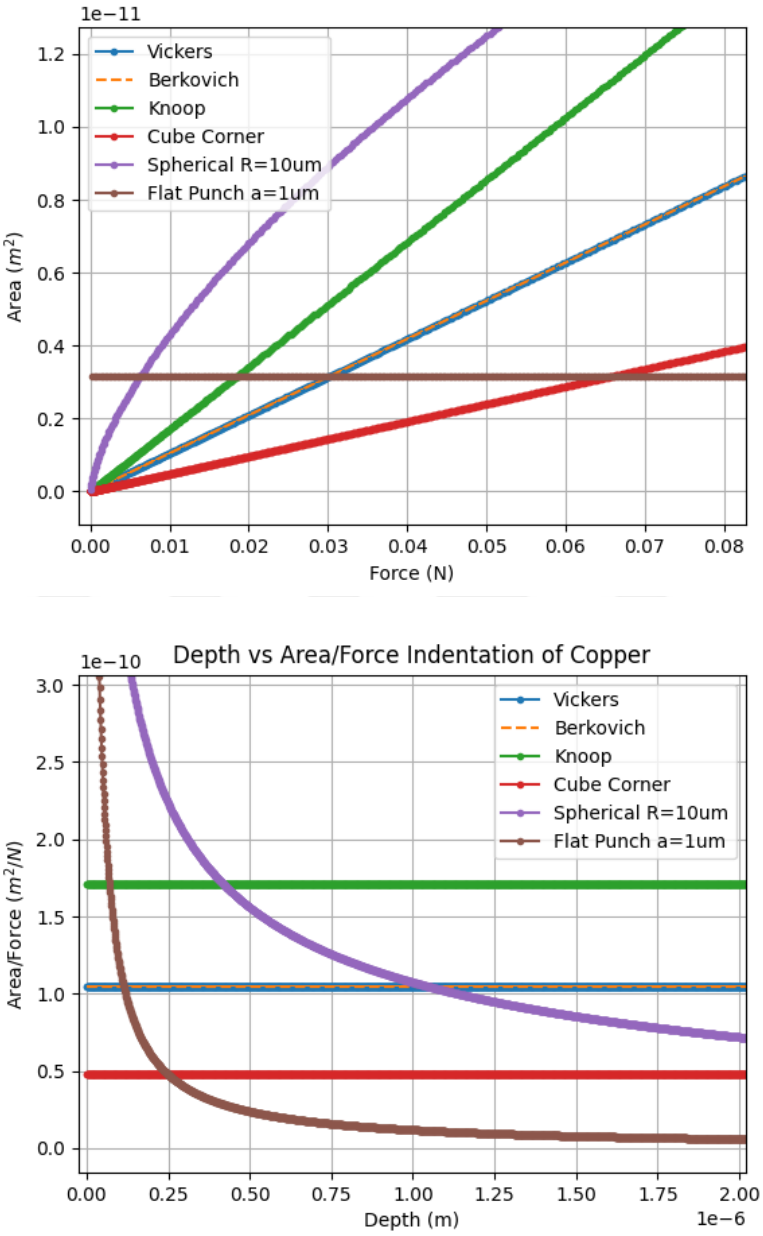

Figure 4.2 : Area vs Force graph (top), and depth dependency of area per force (bottom) for different indenter geometries and for pure elastic behavior.

mentioned a sharp conic tip with 30° half cone angle at the simulations with plastic deformations included.

4.2 Elastic Regime Shape Optimization of Fin Efficiency for Indentations

After several shape optimization in the manner of area versus force calculations, the direct thermal contribution of the increased area by indentation is calculated by the presumed gradient (in Section 1.2.1) which decreases the effectiveness of the heat transfer channel.

These calculations had been made similar with the fit functions in the Results section. Therefore, we put an inverse spreading resistance (conductance) from diamond tip to copper sample multiplied by efficiency along the indenter determined by diamond-copper interface and diamond conductivity (and also conic half angle).

The results presented at the Figure 4.3 calculated for a base radius of 10 μm and a constant interface conductance of 1E+10. Results show a rapid saturation for cylindrical (flat punch) case up to 10 μm while conical fin also shows fast decreasing in the efficiency, but it is not saturated.

The results presented at the Figure 4.4 calculated for a base radius of 2 μm and a constant interface conductance of 1E+10. Results show a rapid saturation for cylindrical (flat punch) case up to 2 μm while conical fin also shows fast decreasing in the efficiency, but it is not saturated completely up to 10 μm.

The two different base radius results show that increasing the cylinder radius provides an increasing saturation depth as can be expected.

A total efficiency calculation trial had been made also along conic half angles that is made by multiplication of inverse pressure efficiency and fin efficiency for cone.

In Figure 4.5 results are shown for sharp to wide cones, and as can be expected, wider cone angles show more efficiency both for the inverse pressure and the heat rate.

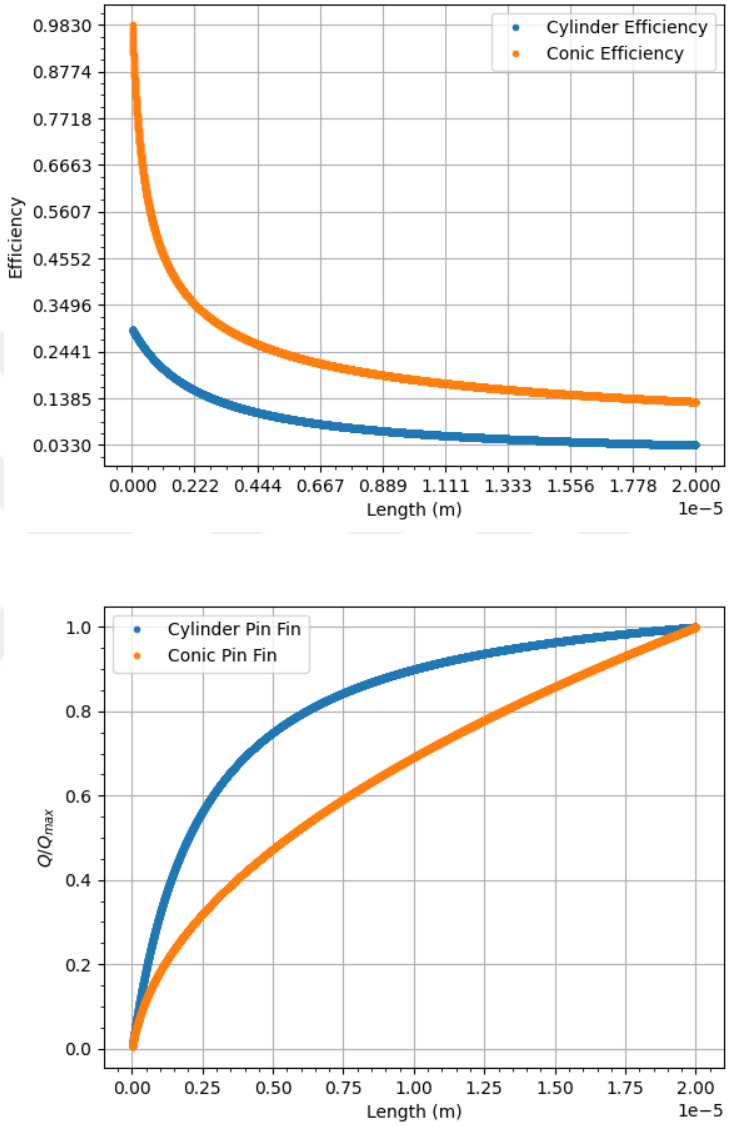

Figure 4.3 : Change of the efficiency (top) and heat rate (bottom) of the heat transfer channel for constant conductance 1E+10 $W/(m^2K)$ with respect to depth while the diameter of the beginning of the extension is kept constant 10 μm for cylinder (blue), and cone's (orange) half angle is 60°.

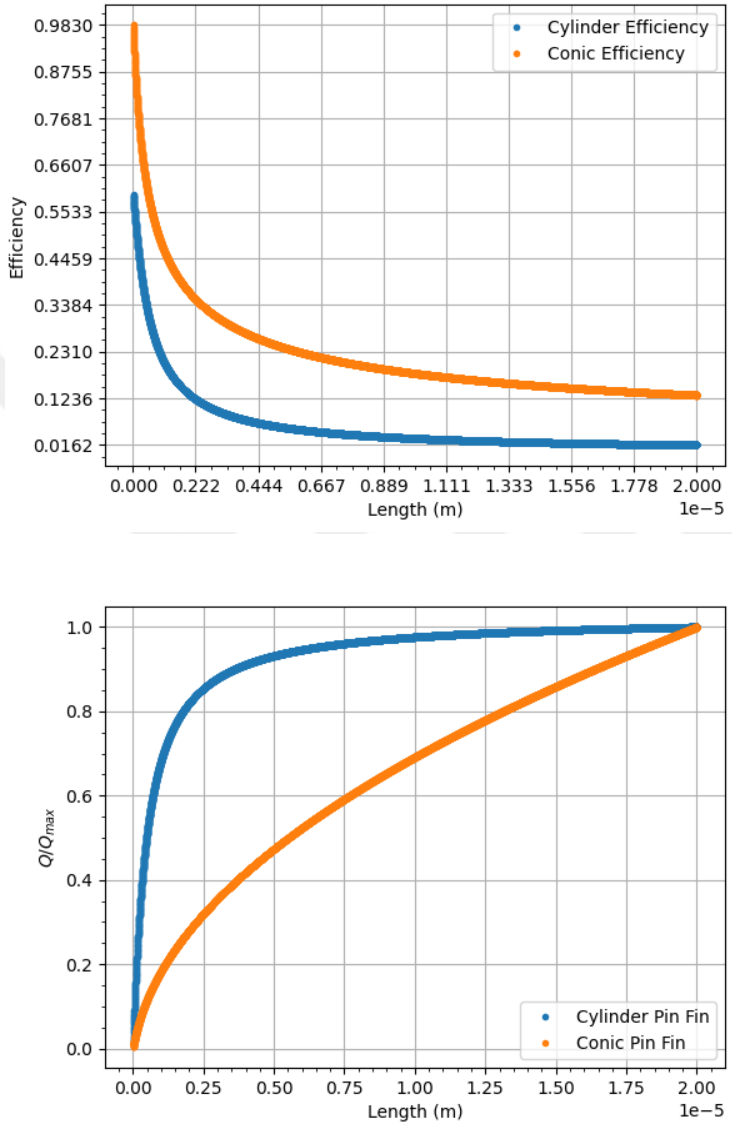

Figure 4.4 : Change of the efficiency (top) and heat rate (bottom) of the heat transfer channel for constant conductance 1E+10 $W/(m^2K)$ with respect to depth while the diameter of the beginning of the extension is kept constant 2 μm for cylinder (blue), and cone's (orange) half angle is 60°.

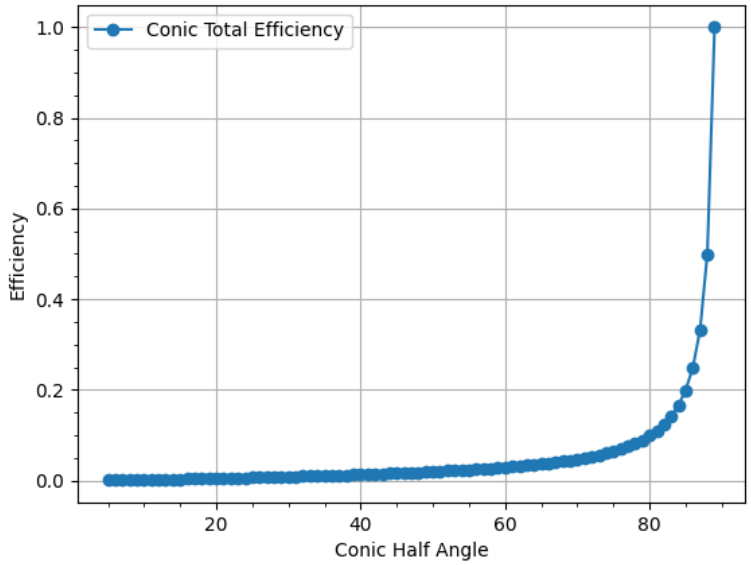

Figure 4.5 : Total efficiency (inverse pressure to heat efficiency multiplication) calculation for conic angles.

4.3 Elastoplastic Simulations of Indentation

Beyond the elastic regime, we conducted FEA simulations to investigate plasticity effects on area optimization. Indentations of different tip geometries are simulated on copper with 2D Axis-symetric Dynamic-Explicit solver. Indenters are modeled as rigid bodies with different geometries due to the fact that diamond behaves as a rigid brittle body on metallic indentations with owing about 1 order of magnitude higher elastic modulus than copper (130 GPa and 1220 GPa, copper and diamond respectively).

From the simulations, wider angle cone (near Berkovich equivalent half cone angle 70° to a sharp half cone angle 30°) seems more efficient in the area optimization manner with indentation depth. Even though spherical punch seems to be more efficient at the beginning as shown in the calculations also, Berkovich equivalent cone tends to catch spherical area up to 2-3 μm. In addition, at the 1 μm Berkovich becomes more efficient for the inverse pressure.

Interestingly, sharp conic shows more efficiency for the inverse pressure calculation from the elastoplastic simulation results. A number of 8 μm^2 per mN at the 1 μm for Berkovich and Spherical Punch can be estimated, while for the sharp cone (30° half

cone angle) at the 4 μm of indentation, it is about 10 μm^2 per mN. Even though the indentation depths are different for the two conic half angles, we expect self similarity for the conic shapes, so they should behave same along all the depths. Furthermore, from the graphical results, we deduced that the pile-up effect makes more efficient the sharper one. Therefore, these results show especially for the highly plastic materials at micro scale, it is important to include plasticity effects for the optimization of pressure. The efficiency increase due to pile-up is also important for the thermal efficiency. Because, pile-up means area yield above the base of indenter that is different from the fin approach that just includes the area efficiency after the base. Nevertheless, we have not made further investigations on this issue due to being more focused on the consistency of the experiments with general area efficiency functions, and we left more comprehensive investigations for next studies.

4.4 Thermal Simulations of Contact Resistance and Channelling

In addition to dynamic-explicit simulations, coupled-static/quasi-static analyses are conducted by using ABAQUS to clarify simultaneous heat transfer and indentation effects. Moreover, to understand channelling/fin behavior, several only heat transfer simulations have been run on indents at different depths and conductivity to conductance ratio.

Firstly, to check whether ABAQUS simulation provides the spreading resistance within the studied dimensions and materials, we had conducted heat transfer analysis by putting several uniform temperature boundaries with different radii.

In Figure 4.8 the resistance calculation results from the simulation of temperature boundary is demonstrated. Moreover, to see clearly the constriction resistance holds in that regime of 5 μm radius, inverse resistance (conductance) is calculated, and is shown at the bottom graph of Figure 4.8. The slope of the conductance graph should show (Eq. 1.14):

$$m = 4k \tag{4.1}$$

The calculation of the slope has given about 1539, and the conductivity can be found as 384.75 $Wm^{-1}K^{-1}$ which is very close to given value of 385.

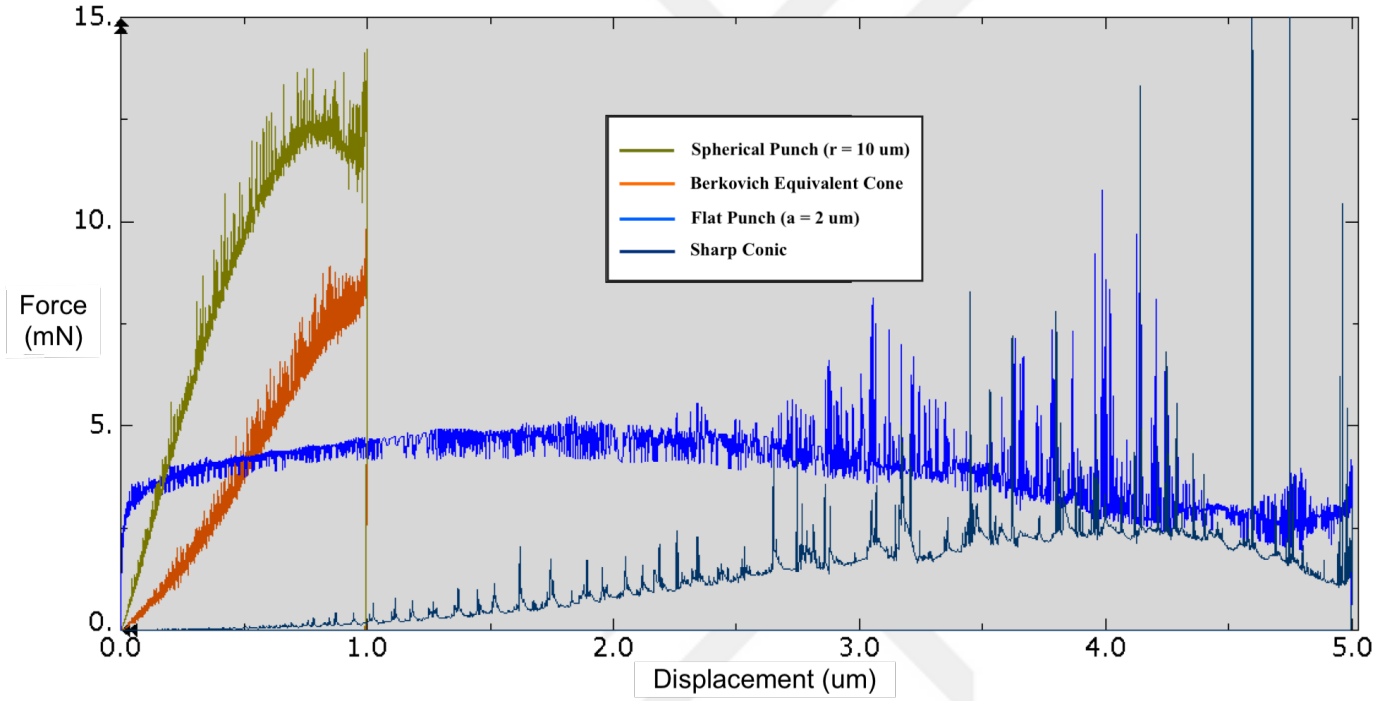

Figure 4.6 : Force vs Displacement Curves Simulated for Different Geometries of spherical punch (10 μm radius) (red), Berkovich (70° half cone angle) (purple), 30 ° half cone angle of sharp cone (brown) and a 2 μm radius of flat punch (Prussian blue).

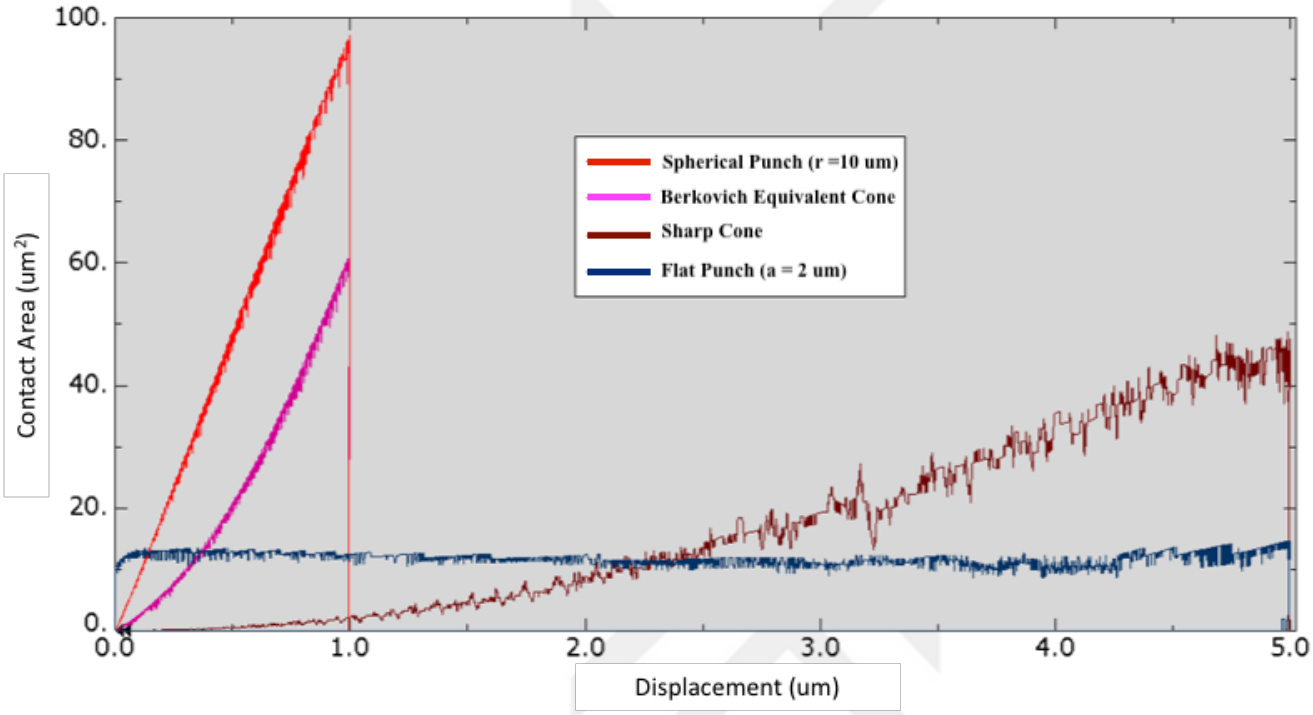

Figure 4.7 : Contact Area vs Displacement Curves Simulated for Different Geometries.

Therefore, results show, we can investigate the constriction issue with our axis-symmetric 200 μm radius copper model.

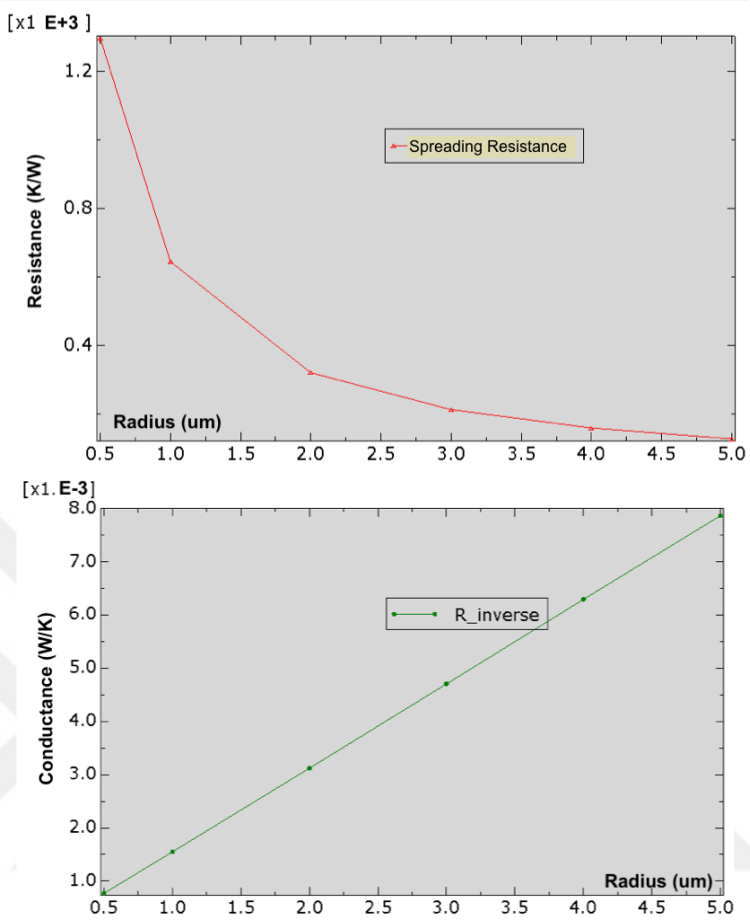

Figure 4.8 : (top) Spreading resistance change with radius and (bottom) inverse resistance (conductance) with respect to radius of temperature boundary on the copper sample.

Coupled indentation and heat transfer simulation results on bulk copper with diamond indenter had been pursued too (Figure 4.9). However, coupled analysis consumes much more time and storage with little help on the our area efficiency investigations especially for the cylindrical cases, so we had tried to simulate several instances of the contact without deformation analysis.

Hence, ABAQUS simulations had been made for channelling by creating many contact instances of cylindrical penetrations. Using those simulations, we reached to similar results of cylindrical fin efficiency by calculating the total (from top of the tip to bottom of the sample) and spreading (from the contact to bottom of the sample) resistances (Figure 4.10).

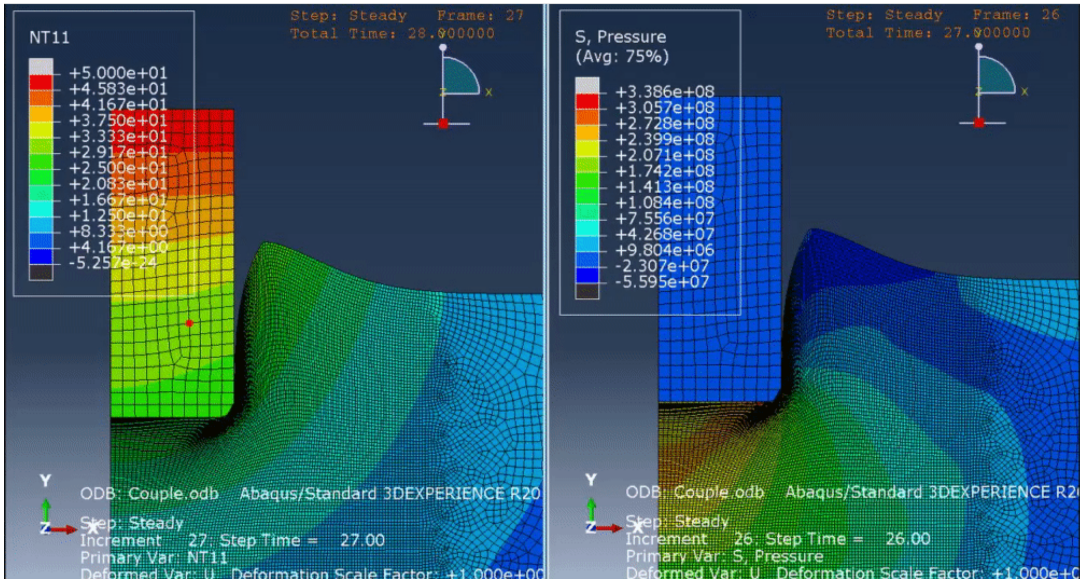

Figure 4.9 : Coupled Indent and Heat Transfer Analysis Result, hold after indent instance is shown.

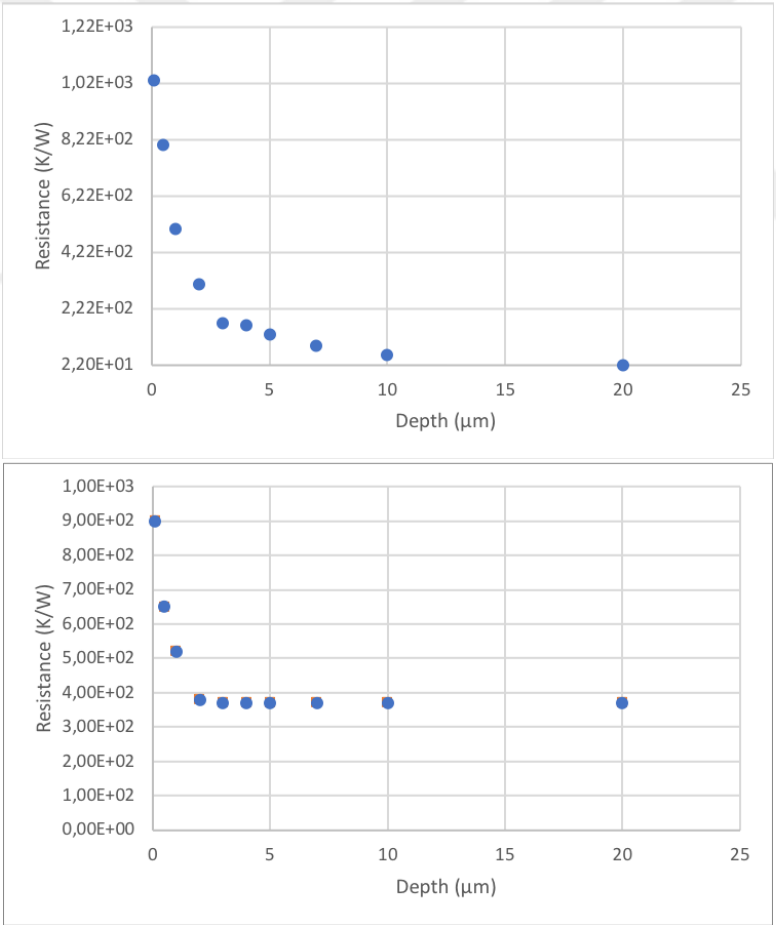

Figure 4.10 : ABAQUS Simulation Results for Change of Resistance by Cylindrical Perfect (all indentation depth contributes to contact depth) Indentation into Sample, resistance is calculated along the indentation axis $\Delta T/Q$ using surface conductance as E+10, (top) Spreading Resistance, (bottom) Total Resistance.

Results show a saturation behavior after 3 μm which can be seen also from the calculation of cylinder fin efficiency with the same 2 μm diameter in the Figure 4.4. Moreover, even the spreading resistance that is calculated from the contact of the tip of the flat punch to copper shows an ongoing decrease, total resistance seems to be saturated with the gradient along the tip. This result shows that how important the gradient can be while trying to increase the area and decrease the constriction by pushing the tip into sample.

Furthermore, we investigated the conductivity ratio effect on the spreading and total resistances along a 20 μm cylinder tip inside a copper specimen by changing the tip's conductivity.

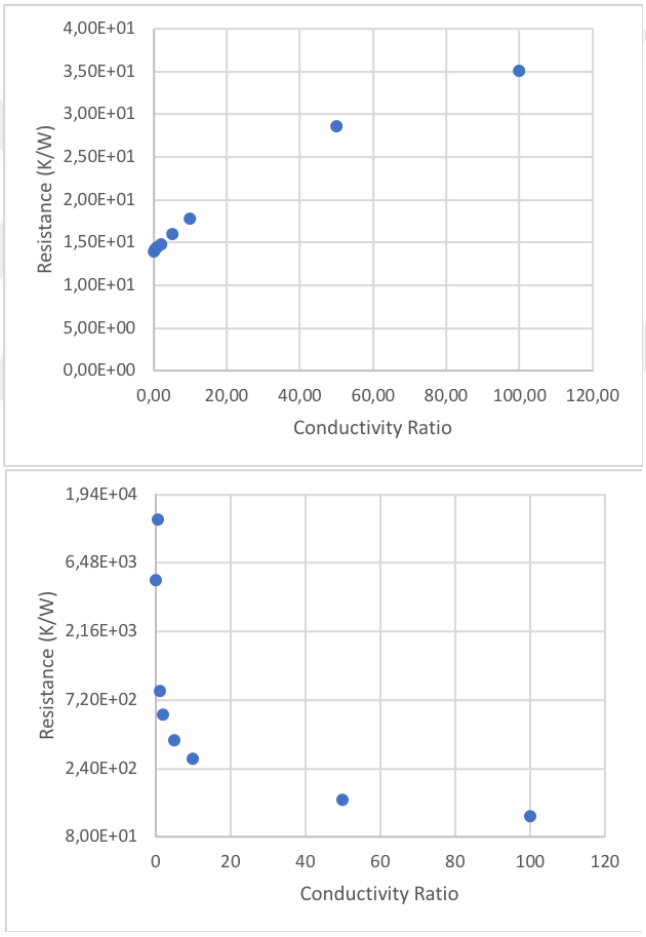

Figure 4.11 : Spreading (top) and total (bottom) resistance change with respect to conductivity ratio k_{tip}/k_{sample} using surface conductance as E+10.

The conductivity ratio of tip to sample is made by holding the sample conductivity of copper and the tip-sample interface conductance same, while changing the tip conductivity from 1% to 100 times of the sample's conductivity. For the

metal-diamond interface about the value of E+10 can be found in different studies. Therefore, we show here change of effectiveness of the gradient while changing the conductivity of diamond contacting through 20 μm indent. Interestingly, here increase of the conductivity increases the spreading part of the resistance while the total resistance decreases. Total resistance tends to be saturated at about 50 times higher conductivity is given for the tip part. Up to the saturation region, we see rapid decrease in the gradient along the tip, after the conductivity becomes 10 times of copper, spreading resistance resistance becomes comparable in total resistance. Therefore, we can see for a constant high surface conductance of interface, spreading effect begins to suppress the total conductance after gradient is overcome for the indented contacts.

5. CONCLUSIONS

Thermal Contact Conductance (TCC) of single microscale junctions under high plastic deformation have been investigated in this thesis. Experimental analysis of the thermal contacts has been conducted with home-made indenter-thermal junction setup while analytical and FEA calculations have been made for different perspectives of the contacts of indentation.

Contacts that are created by penetration of a tip into a sample rather than the mostly studied case of flattening asperities of metallic contacts have been expected to demonstrate a temperature gradient along the tip which is analogous of the well-known fin efficiency. Therefore, we unified the disc constriction resistance picture of the contacts with cylindrical and conical pinned fin efficiency functions as explained in detail in the Introduction 1.2.1.

Experimental results have demonstrated a good agreement in the behavior of the time constant measurements with efficiency functions. Moreover, constant conductance (inverse area fit), modified disc constriction (inverse depth fit), and fits of efficiency functions for the square root area rather than the depth solely have been tried.

The TTC results as well as fits of TTC to aforementioned functions in average show contact conductance ranking from the lowest to highest as Al, Cu and Au. However, just taking into account the harmonic conductivity picture of constriction is not enough with the highly plastic indented contacts. Especially, about two times higher hardness of copper from gold may be resulted in more conforming gold-diamond contact, so lower TTC values are obtained for the experiments with gold.

Moreover, the direct surface conductance estimations with area fit revealed average values in the order of E+4 with a general contact area to overall area ratio of 1% for the diamond tip. These results seem to comply with the values of the literature. Moreover, with help of the efficiency fit functions, we could estimate indirect interface conductance for the diamond-metal interfaces. The results show very high values of

conductance varying with the used fit function from E+8 to E+13 for cylindrical to conic efficiency functions respectively. These results also comply with the results in the order of magnitudes both calculation and experimental studies of the literature.

In addition, calculation and simulation results have shown that gradient occurs and becomes effective for the indented microscale junctions with high interface conductance. Therefore, we emphasized that inclusion of efficiency function in the thermal contacts of indentation is an accurate approach, and fitting experimental results of TTC has simulation and analytical calculation supports.

Beyond providing support for the establishment of the mentioned efficiency picture for contacts, the simulation and calculation results had been tried to find the most effective indentation contact depth and shape. Elastic regime calculations show that wider cone angle is generally more effective for both the pressure minimization and the thermal gradient decrease. However, when plasticity was included in the simulations, the sharper cone was found more effective for the pressure case due to pile-up occurrence. It seems also can be helpful for the thermal issue due to obtaining more contact area above the base of contact surface, so the micro scale engineering of the thermal contacts should be evaluated with these high plasticity effects.

In addition, we found that before the spreading resistance starts to suppress the conductance of the contact pairs, the gradient occurrence should be overcome with the varying conductivity simulations of the perfectly conforming cylindrical indentation. Thus, for the creation of the surface extensions for increasing the thermal contact conductance, the effect of gradient occurrence on the tip should not be underestimated especially for high quality interfaces as being in the diamond and metal.

To conclude, we have seen the fin similarity can be, and should be used in the interpretation of the thermal contacts of indentation. The single asperity in the micro scale has been investigated with this unique approach, and novel oscillatory experimental design. Even though this study consists of diamond-metal contacts, proposed experimental procedure can be applied for any contact pairs, and can be compared with the literature. The pursued data analysis is focused on providing reliable single thermal time constant for contact or separation sequence of the contact.

However, with help of improvements of the temperature measurement resolution, we may extract each cycle of contact rather than average of many quasi-steady state contact cycles at different indentation depth. Furthermore, with the mentioned improvements the (slow) indentation parts and (square wave) impact effects of the experiments would be also deduced for the thermal contact conductance estimations.

Consequently, there are several issues that are left to ongoing research works. Firstly, the indenter should be more accurate and machine compliance should be decreased to simultaneously measure the mechanical properties accurately. More importantly, the indentation depth should be known more accurately which is mostly dependent on the problems of the machine compliance. Secondly, the thermal measurement part of the setup would be developed with more precise devices or as mentioned in the Experimental Setup (Chapter 2) with direct measurement through diamond. The setup has no control on the tip temperature yet, and its temperature is just determined by thermal balance between the medium and contact to the sample, after a certain level of indentation, obtaining resolvable data becomes impossible as can be seen in the Experimental Results section (Chapter 3). This problem can be solved partially by putting a cooler on the tip as near as possible, but there will be eventually a limit to measure through this procedure and setup. However, just for a thought experiment, putting all the tip with a cooler on it and embedding in the sample, then, measuring temperature directly through the tip (i.e. via NV centers of Diamond tip) may give some results for the sake of contact resistance measurements. Indeed similar situations have been shown via ABAQUS simulations (Chapter 4).

REFERENCES

[1] **Song, H.**, **Liu, J.**, **Liu, B.**, **Wu, J.**, **Cheng, H.M. and Kang, F.** (2018). Two-Dimensional Materials for Thermal Management Applications, *Joule*, *2*, 442–463.

[2] **Bergman, T.L.**, **Lavine, A.S.**, **DeWitt, D.P. and Incropera, F.P.** (2011). *Introduction to Heat Transfer*, John Wiley & Sons, sixth edition edition.

[3] (2015). Metallic materials-Instrumented indentation test of hardness and materials parameters.

[4] **Mosso, N.**, **Drechsler, U.**, **Menges, F.**, **Nirmalraj, P.**, **Karg, S.**, **Riel, H. and Gotsmann, B.** (2017). Heat transport through atomic contacts, *Nature Nanotechnology*, *12*, 430–433.

[5] **Cui, L.**, **Jeong, W.**, **Hur, S.**, **Matt, M.**, **Klöckner, J.C.**, **Pauly, F.**, **Nielaba, P.**, **Cuevas, J.C.**, **Meyhofer, E. and Reddy, P.** (2017). Quantized thermal transport in single-atom junctions, *Science*, *355*, 17, `http://science.sciencemag.org/`.

[6] **Gotsmann, B. and Lantz, M.A.** (2013). Quantized thermal transport across contacts of rough surfaces, *Nature Materials*, *12*, 59–65.

[7] **Cui, L.**, **Hur, S.**, **Akbar, Z.A.**, **Klöckner, J.C.**, **Jeong, W.**, **Pauly, F.**, **Jang, S.Y.**, **Reddy, P. and Meyhofer, E.** (2019). Thermal conductance of single-molecule junctions, *Nature*, *572*, 628–633.

[8] **Warzoha, R.J. and Fleischer, A.S.** (2014). Heat flow at nanoparticle interfaces, *Nano Energy*, *6*, 137–158.

[9] **Yovanovich, M.M. and Marotta, E.E.** (2003). *Thermal Spreading and Contact Resistances*, JOHN WILEY & SONS, INC.

[10] **Yovanovich, M.M.** (2005). Four decades of research on thermal contact, gap, and joint resistance in microelectronics, *IEEE Transactions on Components and Packaging Technologies*, *28*, 182–206.

[11] **Madhusudana, C.V.** (2014). *Thermal Contact Conductance*, Springer, second edition edition, `http://www.springer.com/series/1161`.

[12] **Cahill, D.G.**, **Braun, P.V.**, **Chen, G.**, **Clarke, D.R.**, **Fan, S.**, **Goodson, K.E.**, **Keblinski, P.**, **King, W.P.**, **Mahan, G.D.**, **Majumdar, A.**, **Maris, H.J.**, **Phillpot, S.R.**, **Pop, E. and Shi, L.** (2014). Nanoscale thermal transport. II. 2003-2012, *Applied Physics Reviews*, *1*.

[13] **Bahrami, M.** (2004). *Modeling of Thermal Joint Resistance for Sphere-Flat Contacts in a Vacuum*, University of Waterloo.

[14] (2021). *Global Thermal Management Market (2021 to 2026)*, https://tinyurl.com/thermal-market-forecast.

[15] **Razeeb, K.M.**, **Dalton, E.**, **Cross, G.L. and Robinson, A.J.** (2018). Present and future thermal interface materials for electronic devices, *International Materials Reviews*, *63*, 1–21, https://www.tandfonline.com/doi/full/10.1080/09506608.2017.1296605.

[16] **Prasher, R.** (2006). Thermal interface materials: Historical perspective, status, and future directions, *Proceedings of the IEEE*, *94*, 1571–1586.

[17] **Hamann, H.F.**, **Weger, A.**, **Lacey, J.A.**, **Hu, Z.**, **Bose, P.**, **Cohen, E. and Wakil, J.** (2007). Hotspot-Limited Microprocessors: Direct Temperature and Power Distribution Measurements, *IEEE Journal of Solid-State Circuits*, *42*(1), 56–65.

[18] **Dou, R.**, **Li, Q.**, **Zhu, C.**, **Zhang, R.**, **Wen, Z. and Liu, X.** (2019). Experimental study on the enhancement of contact heat transfer by micro fin, *International Journal of Heat and Mass Transfer*, *134*, 482–488.

[19] **Cui, J.**, **Wang, J.**, **Zhong, Y.**, **Pan, L. and Weibel, J.A.** (2018). Metallized compliant 3D microstructures for dry contact thermal conductance enhancement, *Journal of Micromechanics and Microengineering*, *28*.

[20] **Cui, J.**, **Wang, J.**, **Weibel, J.A. and Pan, L.** (2019). A compliant microstructured thermal interface material for dry and pluggable interfaces, *International Journal of Heat and Mass Transfer*, *131*, 1075–1082.

[21] **Cui, J.**, **Pan, L. and Weibel, J.A.** (2019). DEMONSTRATION OF A COMPLIANT MICRO-SPRING ARRAY AS A THERMAL INTERFACE MATERIAL FOR PLUGGABLE OPTOELECTRONIC TRANSCEIVER MODULES, http://asmedigitalcollection.asme.org/InterPACK/proceedings-pdf/InterPACK2019/59322/V001T02A004/6461948/v001t02a004-ipack2019-6389.pdf.

[22] **Xu, W. and Zhang, L.** (2019). Heat effect on the material removal in the machining of fibre-reinforced polymer composites, *International Journal of Machine Tools and Manufacture*, *140*, 1–11.

[23] **Burghold, E.M.**, **Frekers, Y. and Kneer, R.** (2015). Determination of time-dependent thermal contact conductance through IR-thermography, *International Journal of Thermal Sciences*, *98*, 148–155.

[24] **Williamson, M. and Majumdar, A.** (1992). Effect of Surface Deformations on Contact Conductance, *Journal of Heat Transfer*, *114*, 802–810.

[25] **Abdollahi, H.**, **Shahraki, S. and Motahari-Nezhad, M.** (2017). A review on the effects of different parameters on contact heat transfer, *Thermophysics and Aeromechanics*, *24*, 499–512.

[26] **Razavi, M.**, **Muzychka, Y.S. and Kocabiyik, S.** (2016). Review of advances in thermal spreading resistance problems, *Journal of Thermophysics and Heat Transfer*, *30*, 863–879.

[27] **Peng, J.**, **Hong, J. and Zhuang, Y.** (2012). A new model for constriction resistance of rough contacts between nominally flat surfaces, volume110-116, pp.977–984.

[28] **Mikic, B.B.** (1974). THERMAL CONTACT CONDUCTANCE; THEORETICAL CONSIDERATIONS, *Int. J. Heat Mass Tranfer*, *17*, 205–214.

[29] **Laming, L.C.** (1963). Thermal conductance of machined metal contacts, American Society of Mechanical Engineers, p.65–76.

[30] **Malkov, V.A.** (1970). Thermal contact resistance of machined metal surfaces in a vacuum environment(Heat resistance of machined stainless steel and molybdenum contact pairs in vacuum, discussing compressive loads and surface defects effects), *Heat Transfer-Soviet Research*, *2*, 24–33.

[31] **Tien, C.L.** (1968). A correlation for thermal contact conductance of nominally flat surfaces in vacuum, *Thermal Conductivity, Proceedings of the Seventh Conference, National Bureau of Standards Special Publication*, volume302, pp.755–759.

[32] **Madhusudana, C.V. and Fletcher, L.S.** (1983). SOLID SPOT THERMAL CONDUCTANCE OF ZIRCALOY-2/URANIUM DIOXIDE INTERFACES., *Nuclear Science and Engineering*, *83*, 327–332.

[33] **Madhusudana, C.V. and Fletcher, L.S.** (1981). Gas conductance contribution to contact heat transfer, American Institute of Aeronautics and Astronautics (AIAA).

[34] **Xian, Y.**, **Zhang, P.**, **Zhai, S.**, **Yang, P. and Zheng, Z.** (2019). Re-estimation of thermal contact resistance considering near-field thermal radiation effect, *Applied Thermal Engineering*, *157*.

[35] **Cheng, Y.T. and Cheng, C.M.** (2000). What is indentation hardness?, *Surface and Coatings Technology*, *133134*, 417424.

[36] **Chudoba, T. and Jennett, N.M.** (2008). Higher accuracy analysis of instrumented indentation data obtained with pointed indenters, *Journal of Physics D: Applied Physics*, *41*.

[37] **Oliver, W.C. and Pharr, G.M.** (1992). An improved technique for determining hardness and elastic modulus using load and displacement sensing indentation experiments, *J. Mater. Res.*, *7*, 1564–1583.

[38] **Cook, R.F.** (2011). *Indentation and Adhesion at Small Length Scales*, Pan Stanford.

[39] **Fischer-Cripps, A.C.** (2009). *The IBIS Handbook of Nanoindentation*, Fischer-Cripps Laboratories.

[40] **Doerner, M.F. and Nix, W.D.** (1986). A method for interpreting the data from depth-sensing indentation instruments, *J. Mater. Res.*, *1*, 601–609.

[41] **Pethica, J.B.**, **Hutchings, R. and Oliver, W.C.** (1983). Hardness measurement at penetration depths as small as 20 nm, *Philosophical Magazine A: Physics of Condensed Matter, Structure, Defects and Mechanical Properties*, *48*, 593–606.

[42] **Wheeler, J.M.**, **Brodard, P. and Michler, J.** (2012). Elevated temperature, in situ indentation with calibrated contact temperatures, *Philosophical Magazine*, *92*, 3128–3141.

[43] **Le, K.C.** (2020). Two universal laws for plastic flows and the consistent thermodynamic dislocation theory, *Mechanics Research Communications*, *109*, `https://www.researchgate.net/publication/339164170`.

[44] **Cross, G.L.**, **O'Connell, B.S.**, **Pethica, J.B.**, **Rowland, H. and King, W.P.** (2008). Variable temperature thin film indentation with a flat punch, *Review of Scientific Instruments*, *79*.

[45] **Butt, H.J. and Kappl, M.** (2010). *Surface and Interfacial Forces*, Wiley-VCH.

[46] **Howard, J.R. and Sutton, A.E.** (1970). An Analogue Study of Heat Transfer Through Periodically Contacting Surfaces, *Int. J. Heat Mass Transfer*, *13*, 177–183.

[47] **Howard, J. and Sutton, A.E.** (1973). The Effect of Thermal Contact Resistance on Heat Transfer Between Periodically Contacting Surfaces, *Journal of Heat Transfer*, 411–412.

[48] **Howard, J.R.** (1976). An Experimental Study of Heat Transfer Through Periodically Contacting Surfaces, *Int. J. Heat Mass Transfer*, *19*, 367–372.

[49] **Schneider, G.E.**, **Strong, A.B. and Yovanovich, M.M.** (1977). Transient Thermal Response of Two Bodies Communicating Through a Small Circular Contact Area, *Int. J. Heat Mass Transfer*, *20*, 301–308.

[50] **Vick, B. and Ozisik, M.N.** (1981). Quasi-Steady-State Temperature Distribution in Periodically Contacting Finite Regions, *Journal of Heat Transfer*, *103*, 739–744, `http://www.asme.org/about-`.

[51] **Moses, W.M. and Johnson, R.R.** (1988). Experimental Study of the Transient Heat Transfer Across Periodically Contacting Surfaces, *J. Thermophysics*, *2*, 37–42.

[52] **Moses, W.M. and Johnson, R.R.** (1989). Experimental Results for the Quasisteady Heat Transfer Through Periodically Contacting Surfaces, *J. Thermophysics*, *3*, 474–476.

[53] **Moses, W.M. and Dodd, N.C.** (1990). Heat Transfer Across Aluminum/Stainless-Steel Surfaces in Periodic Contact, *J. Thermophysics*, *4*, 396–398.

[54] **Dodd, N.C. and Moses, W.M.** (1988). Heat Transfer Across Aluminum/Stainless Steel Surfaces in Periodic Contact.

[55] **Wahid, S.M. and Madhusudana, C.V.** (2003). Thermal contact conductance: Effect of overloading and load cycling, *International Journal of Heat and Mass Transfer*, *46*, 4139–4143.

[56] **Wang, H. and Degiovanni, A.** (2002). Heat transfer through periodic macro-contact with constriction, *International Journal of Heat and Mass Transfer*, *45*, 2177–2190, `www.elsevier.com/locate/ijhmt`.

[57] **Beck, J.V.**, **Blackwell, B. and Jr., C.R.S.C.** (1985). *Inverse Heat Conduction, Ill-Posed Problems*, J. Wiley.

[58] **Beck, J.V.** (1969). DETERMINATION OF OPTIMUM EXPERIMENTS FOR THERMAL CONDUCTANCE, *Int. J. Heat Mass Transfer*, *12*, 621–633.

[59] **Beck, J.V.** (1967). TRANSIENT SENSITIVITY COEFFICIENTS FOR THE THERMAL CONTACT CONDUCTANCE, *Int. J. Heat Mass Transfer*, *10*, 1615–1617.

[60] **Fieberg, C. and Kneer, R.** (2008). Determination of thermal contact resistance from transient temperature measurements, *International Journal of Heat and Mass Transfer*, *51*, 1017–1023.

[61] **Burghold, E.M.**, **Frekers, Y. and Kneer, R.** (2017). Transient contact heat transfer measurements based on high-speed IR-thermography, *International Journal of Thermal Sciences*, *115*, 169–175.

[62] **Asif, M.**, **Tariq, A. and Singh, K.M.** (2019). Estimation of thermal contact conductance using transient approach with inverse heat conduction problem, *Heat and Mass Transfer/Waerme- und Stoffuebertragung*, *55*, 3243–3264.

[63] **Frekers, Y.**, **Helmig, T.**, **Burghold, E.M. and Kneer, R.** (2017). A numerical approach for investigating thermal contact conductance, *International Journal of Thermal Sciences*, *121*, 45–54.

[64] **Vu, A.T.**, **Helmig, T.**, **Vu, A.N.**, **Frekers, Y.**, **Grunwald, T.**, **Kneer, R. and Bergs, T.** (2020). Numerical and experimental determinations of contact heat transfer coefficients in nonisothermal glass molding, *Journal of the American Ceramic Society*, *103*, 1258–1269.

[65] **Goudarzi, K. and Shojaeefard, M.H.** (2009). Experimental Study of the Heat Transfer Across Periodically Contacting Surfaces, *Journal of Mechanics*, *25*, 307–311, https://academic.oup.com/jom/article/25/3/307/5942115.

[66] **Goudarzi, K.**, **Ramezani, S.R. and Hajati, S.** (2014). Reducing thermal contact resistance using nanocoating, *Applied Thermal Engineering*, *70*, 641–646.

[67] **Shojaeefard, M.H.**, **Goudarzi, K. and Mazidi, M.S.** (2009). Inverse heat transfer problem of thermal contact conductance estimation in periodically contacting surfaces, *Journal of Thermal Science*, *18*, 150–159.

[68] **Shojaefard, M.H.**, **Ghaffarpour, M. and Noorpoor, A.R.** (2008). Thermal contact analysis using identification method, *Heat Transfer Engineering*, *29*, 85–96.

[69] **Pietrak, K. and Wis̀niewski, T.S.** (2014). Methods for experimental determination of solid-solid interfacial thermal resistance with application to composite materials, *Journal of Power Technologies*, *94*, 270–285.

[70] **Xian, Y.**, **Zhang, P.**, **Zhai, S.**, **Yuan, P. and Yang, D.** (2018). Experimental characterization methods for thermal contact resistance: A review, *Applied Thermal Engineering*, *130*, 1530–1548.

[71] **Loulou, T. and Bardon, J.P.** (2001). Estimation of thermal contact conductance during resistance spot welding, *Experimental Heat Transfer*, *14*, 251–264.

[72] **Henning, C.D. and Parker, R.** (1967). Transient Response of an Intrinsic Thermocouple, *Journal of Heat Transfer*, 146–152, http://asmedigitalcollection.asme.org/heattransfer/article-pdf/89/2/146/5718817/146_1.pdf.

[73] (2018). Crystalbond Product Specifications, https://www.aremco.com/wp-content/uploads/2018/05/A09_18.pdf.

[74] **Fujiwara, M.**, **Sun, S.**, **Dohms, A.**, **Nishimura, Y.**, **Suto, K.**, **Takezawa, Y.**, **Oshimi, K.**, **Zhao, L.**, **Sadzak, N.**, **Umehara, Y.**, **Teki, Y.**, **Komatsu, N.**, **Benson, O.**, **Shikano, Y. and Kage-Nakadai, E.** (2020). Real-time nanodiamond thermometry probing in vivo thermogenic responses, *Sci. Adv*, *6*, 9636–9647, http://advances.sciencemag.org/.

[75] **Neumann, P.**, **Jakobi, I.**, **Dolde, F.**, **Burk, C.**, **Reuter, R.**, **Waldherr, G.**, **Honert, J.**, **Wolf, T.**, **Brunner, A.**, **Shim, J.H.**, **Suter, D.**, **Sumiya, H.**, **Isoya, J. and Wrachtrup, J.** (2013). High-Precision Nanoscale Temperature Sensing Using Single Defects in Diamond, *Nano Letters*, *13*, 2738–2742.

[76] **Cahill, D.G.** (1990). Thermal conductivity measurement from 30 to 750 K: The 3ω method, *Review of Scientific Instruments*, *61*, 802–808.

[77] **Gomès, S.**, **Chapuis, O.**, **Nepveu, F.**, **Trannoy, N.**, **Volz, S.**, **Charlot, B.**, **Tessier, G.**, **Dilhaire, S.**, **Cretin, B. and Vairac, P.** (2007). Temperature Study of Sub-Micrometric ICs by Scanning Thermal Microscopy, *IEEE Transactions on Components and Packaging Technologies, Institute of Electrical and Electronics Engineers*, *30*, 424–431.

[78] **Felinger, A.**, **Kilár, A. and Boros, B.** (2015). The myth of data acquisition rate, *Analytica Chimica Acta*, *854*, 178–182.

[79] **Virtanen, P.**, **Gommers, R.**, **Oliphant, T.E.**, **Haberland, M.**, **Reddy, T.**, **Cournapeau, D.**, **Burovski, E.**, **Peterson, P.**, **Weckesser, W.**, **Bright, J.**, **van der Walt, S.J.**, **Brett, M.**, **Wilson, J.**, **Millman, K.J.**, **Mayorov, N.**, **Nelson, A.R.J.**, **Jones, E.**, **Kern, R.**, **Larson, E.**, **Carey, C.J.**, **Polat, İ.**, **Feng, Y.**, **Moore, E.W.**, **VanderPlas, J.**, **Laxalde, D.**, **Perktold, J.**, **Cimrman, R.**, **Henriksen, I.**, **Quintero, E.A.**, **Harris, C.R.**, **Archibald, A.M.**, **Ribeiro, A.H.**, **Pedregosa, F.**, **van Mulbregt, P. and SciPy 1.0 Contributors** (2020). SciPy 1.0: Fundamental Algorithms for Scientific Computing in Python, *Nature Methods*, *17*, 261–272.

[80] **Taylor, J.R.** (1997). *An Introduction to Error Analysis*, University Science Books, second edition edition.

CURRICULUM VITAE

PHOTO

Name Surname **:** Ahmed Uluca

EDUCATION **:**

- **B.Sc.** 2017, Istanbul Technical University, Faculty of Science and Letters, Department of Physics Engineering
- **M.Sc.** 2022, Istanbul Technical University, Graduate School, Department of Physics Engineering

PROFESSIONAL EXPERIENCE AND REWARDS:

-

PUBLICATIONS, PRESENTATIONS AND PATENTS ON THE THESIS:

- ,
-
-

OTHER PUBLICATIONS, PRESENTATIONS AND PATENTS: